ELECTROPOLYMERIZED DYE-MODIFIED GRAPHITE ELECTRODES FOR SELECTIVE AND SENSITIVE MULTI-ANALYTE ELECTROCHEMICAL DETECTION IN BIOMEDICAL AND ENVIRONMENTAL SYSTEMS

Monique Pacheco do Amaral

Thesis submitted to the Postgraduate Program in Instrumentation and Applied Optics of the Federal Center for Technological Education of Rio de Janeiro, CEFET/RJ, as partial fulfillment of the requirements for the degree of doctor.

Advisor: Ana Lucia Ferreira de Barros
Co-advisor: Ladário da Silva

Rio de Janeiro,

Maio 2026

Ficha catalográfica elaborada pela Biblioteca Central do CEFET/RJ

A485 Amaral, Monique Pacheco do
Electropolymerized dye-modified graphite electrodes for selective and sensitive multi-analyte electrochemical detection in biomedical and environmental systems / Monique Pacheco do Amaral. — 2026.
73f. : il. color. , enc.

Tese (Doutorado) Centro Federal de Educação Tecnológica Celso Suckow da Fonseca, 2026.
Bibliografia : f. 125-136
Orientadora: Ana Lucia Ferreira de Barros
Coorientador: Ladário da Silva

1. Eletroquímica. 2. Polimerização. 3. Eletrodos. 4. Detectores. 5. Voltametria. I. Barros, Ana Lucia Ferreira de. (Orient.). II. Silva, Ladário da. (Coorient.). III. Título.

CDD 541.37

Elaborada pela bibliotecária Tania Mello – CRB/7 nº 5507/04

ELECTROPOLYMERIZED DYE-MODIFIED GRAPHITE ELECTRODES FOR SELECTIVE AND SENSITIVE MULTI-ANALYTE ELECTROCHEMICAL DETECTION IN BIOMEDICAL AND ENVIRONMENTAL SYSTEMS

Thesis submitted to the Postgraduate Program in Instrumentation and Applied Optics of the Federal Center for Technological Education of Rio de Janeiro, CEFET/RJ, as partial fulfillment of the requirements for the degree of doctor.

Monique Pacheco do Amaral

Examining jury:

Ana Lucia Ferreira de Barros
Assinado de forma digital por Ana Lucia Ferreira de Barros
Dados: 2026.06.17 03:35:32 -03'00'

President, Profa. Dra. Ana Lucia Ferreira de Barros (CEFET/RJ) (Advisor)

gov.br Documento assinado digitalmente
LADARIO DA SILVA
Data: 16/06/2026 13:53:41-0300
Verifique em https://validar.iti.gov.br

Prof. Dr. Ladário da Silva (UFF/RJ) (Co-advisor)

gov.br Documento assinado digitalmente
ANA GRACI BRITO MADURRO
Data: 15/06/2026 17:03:51-0300
Verifique em https://validar.iti.gov.br

Profa. Dra. Ana Graci Brito Madurro (UFU/MG)

gov.br Documento assinado digitalmente
JOAO MARCOS MADURRO
Data: 15/06/2026 09:54:26-0300
Verifique em https://validar.iti.gov.br

Prof. Dr. João Marcos Madurro (UFU/MG)

gov.br Documento assinado digitalmente
LEANDRO MARQUES SAMYN
Data: 09/06/2026 11:06:01-0300
Verifique em https://validar.iti.gov.br

Prof. Dr. Leandro Marques Samyn (CEFET/RJ)

gov.br Documento assinado digitalmente
DIEGO BARRETO HADDAD
Data: 08/06/2026 15:43:18-0300
Verifique em https://validar.iti.gov.br

Prof. Dr. Diego Barreto Haddad (CEFET/RJ)

Rio de Janeiro,

Maio 2026

DEDICATION

This work is more than just words printed on pages; it's a journey I've undertaken with the tireless support of special people in my life. I dedicate it to:

To God, without His presence I would be nothing. To my husband Manasses, who stood by my side, lifting me up with clarity and affection after every stumble, even in moments of despair. To my children Lorena and Dimitri, who, despite their young age, understood the purpose of being without a mother figure during special moments for them. To my parents, Anália and Wantuil, who have always been the pillars of my upbringing, my deepest gratitude. You taught me that education is the key to achieving our most audacious dreams.

Finally, I dedicate this dissertation to those who could not be present to witness this moment, but whose love and influence continue to guide every step I take. You are eternally present in my memory and in my heart; I dedicate this to my paternal and maternal grandparents (in memorian) , especially Grandma Maria (I miss her very much).

May this work serve not only as an expression of my learning, but also as a sincere tribute to all those who have been part of this journey. May the knowledge contained herein contribute in some way to a more just, compassionate, and humane world..

ACKNOWLEDGMENTS

I give thanks: To God. To my friends, who were by my side in moments of joy and in the times when everything went wrong. Some words echo through the pages of this work, reminding me that the academic journey is more than just study; it is about the bonds we create and the memories we share. To one friend in particular, Suresh, who helped me and taught me with a patience I had never seen before. To the professors who guided and supported me, especially professors Leandro and Ladário, who shared their time and knowledge with all students indiscriminately, whether advisees or not. To my advisor, Professor Ana Lucia Barros, a kind, sincere, intelligent person, committed to teaching and research, an example to be followed, whose wisdom, dedication, and guidance were fundamental in shaping this work and broadening my intellectual, academic, professional, and even personal horizons—thank you very much.

This work was carried out with the support of the Coordenação de Aperfeiçoamento de Pessoal de Nível Superior – Brasil (CAPES) – Finance Code 001.

ABSTRACT

Electropolymerized Dye-Modified Graphite Electrodes for Selective and Sensitive Multi-Analyte Electrochemical Detection in Biomedical and Environmental Systems

Sensores baseados em eletrodos de grafite sensibilizados por corantes constituem uma plataforma versátil para detecção eletroquímica, combinando a alta condutividade de materiais de carbono com as propriedades funcionais de filmes eletropolimerizados. Neste trabalho, eletrodos de grafite foram modificados por eletropolimerização utilizando três corantes: azul de cresil brilhante, azul de timol e azul de bromofenol com o objetivo de desenvolver sensores eletroanalíticos seletivos e sensíveis.

Os eletrodos modificados apresentaram seletividade distinta para diferentes classes de analitos. O eletrodo baseado em azul de cresil brilhante permitiu a detecção de nucleobases e biomoléculas relacionadas, incluindo guanina, adenina, timina, ácido úrico e ácido ascórbico. O eletrodo modificado com azul de timol mostrou-se eficiente na detecção de aminoácidos e compostos orgânicos, como piridoxina, tirosina, vanilina, cisteína e triptofano. O eletrodo baseado em azul de bromofenol apresentou alta sensibilidade para compostos fenólicos e espécies nitrogenadas, incluindo catecol, resorcinol, hidroquinona, hidrazina e pirogalol.

A caracterização eletroquímica foi realizada por voltametria cíclica (VC), voltametria de pulso diferencial (VPD), voltametria de varredura linear (VVL) e cronoamperometria (CA), complementada por estudos de velocidade de varredura e análise de pH. As análises de superfície por microscopia eletrônica de varredura (MEV) e microscopia de força atômica (AFM) confirmaram a formação de filmes poliméricos homogêneos e eletroativos.

Os sensores apresentaram respostas eletroquímicas significativamente superiores em comparação ao eletrodo de grafite não modificado, com excelente linearidade ($R^2 \approx$ 0,99), baixos valores de desvio padrão relativo (RSD $< 10\%$) e tempos de resposta rápidos, da ordem de segundos. Além disso, os eletrodos modificados permitiram a detecção seletiva e simultânea de múltiplos analitos, com picos de oxidação bem resolvidos, evidenciando elevado desempenho analítico mesmo em sistemas complexos. Os sensores também demonstraram boa estabilidade operacional e reprodutibilidade ao longo de medições sucessivas.

Os resultados demonstram que filmes eletropolimerizados baseados em corantes são eficientes na modulação das propriedades eletroquímicas de eletrodos de grafite, permitindo a detecção seletiva e sensível de múltiplos analitos. As plataformas desenvolvidas apresentam forte potencial para aplicações em monitoramento ambiental, diagnósticos clínicos e análise de compostos bioativos.

Keywords: Eletropolimerização; eletrodo de grafite; sensores baseados em corantes; voltametria cíclica; detecção eletroquímica; detecção multianalito.

ABSTRACT

Electropolymerized Dye-Modified Graphite Electrodes for Selective and Sensitive Multi-Analyte Electrochemical Detection in Biomedical and Environmental Systems

Dye-sensitized graphite-based sensors constitute a versatile platform for electrochemical detection, combining the high conductivity of carbon materials with the functional properties of electropolymerized dye films. In this work, graphite electrodes were modified via electropolymerization using three dyes: brilliant cresyl blue, thymol blue, and bromophenol blue to develop selective and sensitive electroanalytical sensors.

The modified electrodes exhibited distinct selectivity toward different classes of analytes. The brilliant cresyl blue-based electrode enabled the detection of nucleobases and related biomolecules, including guanine, adenine, thymine, uric acid, and ascorbic acid. The thymol blue-modified electrode was effective for detecting amino acids and organic compounds such as pyridoxine, tyrosine, vanillin, cysteine, and tryptophan. The bromophenol blue-based electrode showed high sensitivity toward phenolic compounds and nitrogen-containing species, including catechol, resorcinol, hydroquinone, hydrazine, and pyrogallol.

Electrochemical characterization was performed using cyclic voltammetry (CV), differential pulse voltammetry (DPV), linear sweep voltammetry (LSV), and chronoamperometry (CA), complemented by scan rate and pH studies. Surface analyses by scanning electron microscopy (SEM) and atomic force microscopy (AFM) confirmed the formation of homogeneous and electroactive polymeric films.

The sensors exhibited significantly enhanced electrochemical responses compared to the bare graphite electrode, with excellent linearity ($R^2 \approx 0.99$), low relative standard deviation values (RSD $< 10\%$), and fast response times on the order of seconds. In addition, the modified electrodes enabled the selective and simultaneous detection of multiple analytes with well-resolved oxidation peaks, demonstrating their high analytical performance even in complex systems. The sensors also showed good operational stability and reproducibility over repeated measurements.

These results demonstrate that electropolymerized dye films effectively tailor the electrochemical properties of graphite electrodes, enabling selective and sensitive multi-analyte detection. The developed sensing platforms show strong potential for applications in environmental monitoring, clinical diagnostics, and analysis of bioactive compounds.

Keywords: Electropolymerization; graphite electrode; dye-based sensors; cyclic voltammetry; electrochemical detection; multi-analyte sensing.

LIST OF FIGURES

Figure 1 – Representation of the basic structure of a sensor. 17
Figure 2 – Structure of phenazines 17
Figure 3 – Electropolymerization of BCB, Figure adapted from [19]. 18
Figure 4 – Electropolymerization of TB, Figure adapted from [20] 19
Figure 5 – Electropolymerization of BP, Figure adapted from [21]. 20
Figure 6 – Diagram showing the double layer. Figure adapted from [22] with the aid of artificial intelligence tools. 21
Figure 7 – Simplified diagram of the connection between electrodes and potentiostat. 23
Figure 8 – The potentiostat used in this work is located in Laboratory of Experimental and Applied Physics (LaFEA). 24
Figure 9 – Simplified diagram of the AFM 26
Figure 10 – The atomic force microscope at LaFEA. 27
Figure 11 – Schematic diagram of a scanning electron microscope (SEM). Adapted from [50]. 29
Figure 12 – The Scanning Electron Microscope of the High-Resolution Electron Microscopy Laboratory (LaMAR) at the Universidade Federal Fluminense (UFF). 30
Figure 13 – Coating machine of the High Resolution Electron Microscopy Laboratory (LaMAR) of the Universidade Federal Fluminense (UFF): (a) Coating machine; (b) Coating chamber. 30
Figure 14 – High Resolution Electron Microscopy Laboratory (LaMAR) of the Universidade Federal Fluminense (UFF): (A) TEM; (B) FIB. 31
Figure 15 – Schematic representation of an ATR-FTIR system. Adapted from [59] 32
Figure 16 – The FTIR scanner used in this study is located in the LaFEA laboratory. 33

Figure 17 – Photograph of the solutions used: bromophenol blue (BPB), thymol blue (TB), and brilliant cresyl blue (BCB). 39
Figure 18 – Graphite used: (A) Whole graphite; (B) Enlarged image of the graphite. 41
Figure 19 – Method for sanding and polishing graphite electrodes. Figure adapted from [77]. 42
Figure 20 – Analytes and chemical structure. 46
Figure 21 – AFM Image: A - AFM image for the electrode without electropolymerization; B - AFM image for the electrode electropolymerized with BCB. 51
Figure 22 – AFM image: (A) - Electrode electropolymerized with BP and (B) - Electrode electropolymerized with TB. 51
Figure 23 – Scanning electron microscopy images: (A) - Undeposed graphite with x 50000 magnification; (B) - Graphite with PBCB with × 10000 magnification; (C) - Graphite with PBP with × 5000 magnification; (D) - Graphite with PTB with × 10000 magnification. 52
Figure 24 – Micrograph TEM PBCB. 54
Figure 25 – FTIR: (A) PBCB and BCB; (B) PBP and BP and (C) PTB and TB. 56
Figure 26 – Electrochemical study of BCB deposition: (A) Cyclic voltammetry of the cycle showing the current peak for the monomer and polymer; (B) All electropolymerization cycles; (C) Scan Rate: Cyclic voltammetry performed with different scan rates (5mV/s to 1000mV/s); (D) Calibration curve Ip *vs* Scan Rate; (E) Calibration curve Ip *vs* the square root of the Scan Rate; (F) Study of the polymer behavior with PBS at pH 2, pH 7 and pH 10; (G) Study from pH 2 to pH 10; (H) DPV of the polymerized electrode. 59

Figure 27 – Electrochemical study of BP deposition: (A) Cyclic voltammetry of the cycle showing the current peak referring to the monomer and the polymer; (B) Cyclic voltammetry with all cycles; (C) Scan Rate: Cyclic voltammetry performed with different scan rates (5mV/s to 1000mV/s); (D) Calibration curve Ip *vs* Scan Rate; (E) Calibration curve log Ip *vs* log Scan Rate; (F) Study of pH 2, pH 7 and pH 10; (G) Study of the polymer behavior with PBS from pH 2 to pH 10; (H) DPV of the polymerized electrode. 61

Figure 28 – Electrochemical study of TB deposition: (A) Cyclic voltammetry of the cycle showing the peak current related to the monomer and the polymer; (B) Scan Rate: Cyclic voltammetry performed with different scan rates (5mV/s to 400mV/s); (C) Calibration curve Ip *vs* square root of the Scan Rate; (D) Study of the polymer behavior with PBS at pH 2, pH 7 and pH 10; (E) Study from pH 2 to pH 10; (F) Analysis of pH behavior in relation to peak current and potential; (G) DPV of the polymerized electrode. 63

Figure 29 – Guanine Detection: (A) CV: curve (a) Mod 0μM, curve (b) Mod 9.99μM, curve (c) Bare 160μM, curve (d) Mod 81.33μM and curve (e) Mod 160μM; (B) CV test calibration curve; (C) DPV; (D) DPV test calibration curve; (E) LSV; (F) LSV summary; (G) Chronoamperometry; (H) Chronoamperometry test calibration curve. 71

Figure 30 – Guanine Validation: (A) pH; (B) pH Summary; (C) Repeatability; (D) Repeatability Summary; (E) Reproducibility; (F) Reproducibility Summary; (G) Stability; (H) Stability Summary. 72

Figure 31 – Adenine Detection: (A) CV: curve (a) refers to Bare 213.34μM, curve (b) Mod 0μM, curve (c) Mod 11.98μM, curve (d) Mod 136.12μM and curve (e) Mod 213.34μM; (B) CV test calibration curve; (C) DPV: curve (a) refers to Bare 267.63μM, curve (b) Mod 0μM, curve (c) Mod 49.75μM and curve (d) Mod 267.63μM; (D) DPV test calibration curve; (E) LSV; (F) LSV summary; (G) Chronoamperometry; (H) Chronoamperometry test calibration curve. 73

Figure 32 – Adenine Validation: (A) pH; (B) pH Summary; (C) Repeatability; (D) Repeatability Summary; (E) Reproducibility; (F) Reproducibility Summary; (G) Stability; (H) Stability Summary. 74

Figure 33 – Thymine Detection: (A) CV: curve (a) refers to Bare 0μM, curve (b) Bare 375.36μM, curve (c) Mod 0μM and curve (d) Mod 375.36μM; (B) CV with various concentrations; (C) CV test calibration curve; (D) DPV: curve (a) refers to Bare 0μM, curve (b) Bare 1680.5μM and curve (c) Mod 0μM; (E) DPV test calibration curve; (F) LSV; (G) LSV summary; (H) Chronoamperometry; (I) Chronoamperometry test calibration curve. 75

Figure 34 – Thymine Validation: (A) pH; (B) pH Summary; (C) Repeatability; (D) Repeatability Summary; (E) Reproducibility; (F) Reproducibility Summary; (G) Stability; (H) Stability Summary. 76

Figure 35 – Uric acid detection: (A) CV; (B) CV referring to curve (a) Bare 0μM, curve (b) Mod 0μM, curve (c) Bare 1010.42μM and curve (d) Mod 1010.42μM; (C) CV test calibration curve; (D) DPV; (E) DPV: curve (a) referring to Bare 0μM, curve (b) Mod 0μM, curve (c) Bare 1016.88μM and curve (d) Mod 1016.88μM; (F) DPV test calibration curve; (G) LSV; (H) LSV summary; Chronoamperometry; (J) Chronoamperometry test calibration curve. 77

Figure 36 – Uric Acid Validation: (A) pH; (B) pH Summary; (C) Repeatability; (D) Repeatability Summary; (E) Reproducibility; (F) Reproducibility Summary; (G) Stability; (H) Stability Summary. 78

Figure 37 – Ascorbic Acid Detection: (A) CV; (B) CV for curve (a) referring to Mod 0μM, curve (b) Mod 9.99 μM, curve (c) Bare 1258.74 μM and curve (d) Mod 1258.74μM; (C) CV test calibration curve; (D) DPV: curve (a) referring to Bare 0μM, curve (b) Bare 566.03 μM, curve (c) Mod 0μM and curve (d) Mod 566.03μM; (E) DPV test calibration curve; (F) LSV; (G) LSV summary; (H) Chronoamperometry; (I) Chronoamperometry test calibration curve. 79

Figure 38 – Ascorbic Acid Validation: (A) pH; (B) pH Summary; (C) Repeatability; (D) Repeatability Summary; (E) Reproducibility; (F) Reproducibility Summary; (G) Stability; (H) Stability Summary. 80

Figure 39 – Analyte detection scheme using the PBCB electrode. Figure produced by the author using artificial intelligence tools. 81
Figure 40 – Catechol Detection: (A) CV; (B) CV with various concentrations; (C) CV test calibration curve; (D) DPV; (E) DPV test calibration curve; (F) LSV; (G) LSV summary; (H) Chronoamperometry; (I) Chronoamperometry test calibration curve. 86
Figure 41 – Catechol Validation: (A) pH; (B) pH Summary; (C) Repeatability; (D) Repeatability Summary; (E) Reproducibility; (F) Reproducibility Summary; (G) Stability; (H) Stability Summary. 87
Figure 42 – Resorcinol Detection: (A) CV; (B) CV with various concentrations; (C) CV test calibration curve; (D) DPV; (E) DPV test calibration curve; (F) LSV; (G) LSV summary; (H) Chronoamperometry; (I) Chronoamperometry test calibration curve. 88
Figure 43 – Resorcinol Validation: (A) pH; (B) pH Summary; (C) Repeatability; (D) Repeatability Summary; (E) Reproducibility; (F) Reproducibility Summary; (G) Stability; (H) Stability Summary. 89
Figure 44 – Hydroquinone Detection: (A) CV with various concentrations; (B) CV ; (C) CV test calibration curve; (D) DPV; (E) DPV test calibration curve; (F) LSV; (G) LSV summary; (H) Chronoamperometry; (I) Chronoamperometry test calibration curve. 90
Figure 45 – Hydroquinone Validation: (A) pH; (B) pH Summary; (C) Repeatability; (D) Repeatability Summary; (E) Reproducibility; (F) Reproducibility Summary; (G) Stability; (H) Stability Summary. 91
Figure 46 – Hydrazine Detection: (A) CV; (B) CV with various concentrations; (C) CV test calibration curve; (D) DPV; (E) DPV test calibration curve; (F) LSV; (G) LSV summary; (H) Chronoamperometry; (I) Chronoamperometry test calibration curve. 92
Figure 47 – Hydrazine Validation: (A) pH; (B) pH Summary; (C) Repeatability; (D) Repeatability Summary; (E) Reproducibility; (F) Reproducibility Summary; (G) Stability; (H) Stability Summary. 93

Figure 48 – Pyrogallic Acid Detection: (A) CV; (B) CV with various concentrations; (C) CV test calibration curve; (D) DPV; (E) DPV test calibration curve; (F) LSV; (G) LSV summary; (H) Chronoamperometry; (I) Chronoamperometry test calibration curve. 94

Figure 49 – Pyrogallic Acid Validation: (A) pH; (B) pH Summary; (C) Repeatability; (D) Repeatability Summary; (E) Reproducibility; (F) Reproducibility Summary; (G) Stability; (H) Stability Summary. 95

Figure 50 – Analyte detection scheme using the PBP electrode.Figure produced by the author using artificial intelligence tools. 96

Figure 51 – Vanillin Detection: (A) CV; (B) CV: curve (a) referring to Bare0μM, curve (b) Mod 0μM, curve (c) Bare 812.20μM and curve (d) Mod 812.20μM; (C) CV test calibration curve; (D) DPV; (E) DPV: curve (a) referring to Bare 0μM, curve (b) Mod 0μM, curve (c) Bare 1441.29 μM and curve (d) Mod 1441.29 μM; (F) DPV test calibration curve; (G) LSV: curve (a) referring to Mod 0μM, curve (b) Bare 0 μM, curve (c) Mod 23.94μM, curve (d) 122.48μM, curve (e) Mod 461.65μM, curve (f) Bare 1441.28μM and curve (g) Mod 1441.28μM; (H) LSV reflecting curve (a) Mod 0μM, curve (b) Bare 0μM and curve (c) Mod 23.94μM; (I) LSV Summary: curve (a) referring to Mod 0μM, curve (b) Mod 23.94 μM, curve (c) Mod 122.48μM and curve (d) Mod 461.65μM; (J) Chronoamperometry; (K) Chronoamperometry test calibration curve. 101

Figure 52 – Vanillin Validation: (A) pH; (B) pH Summary; (C) Repeatability; (D) Repeatability Summary; (E) Reproducibility; (F) Reproducibility Summary; (G) Stability; (H) Stability Summary. 102

Figure 53 – Tyrosine Detection: (A) CV; (B) CV referring to curve (a) Bare 0μM, curve (b) Mod 0μM, curve (c) Bare 1441.29μM and curve (d) Mod 1441.29μM; (C) CV test calibration curve; (D) DPV; (E) DPV referring to curve (a) Bare 0μM, curve (b) Mod 0μM, curve (c) Bare 1441.29μM and curve (d) Mod 1441.29μM; (F) DPV test calibration curve; (G) LSV: curve (a) referring to Bare 0μM, curve (b) Mod 23.94μM, curve (c) Mod 122.48μM, curve (d) Mod 0μM, curve (e) Bare 1441.28μM and curve (f) Mod 1441.28μM; (H) LSV referring to curve (a) Bare 0μM, curve (b) Mod 0μM, curve (c) Bare 1441.28μM and curve (d) Mod 1441.28μM; (I) LSV Summary: curve (a) referring to Bare 0μM, curve (b) Mod 0μM, curve (c) Mod 122.48μM and curve (d) Mod 1441.28μM; (J) Chronoamperometry; (K) Chronoamperometry test calibration curve. 103

Figure 54 – Tyrosine Validation: (A) pH; (B) pH Summary; (C) Repeatability; (D) Repeatability Summary; (E) Reproducibility; (F) Reproducibility Summary; (G) Stability; (H) Stability Summary. 104

Figure 55 – Tryptophan Detection: (A) CV; (B) CV referring to curve (a) Bare 0μM, curve (b) Mod 0μM, curve (c) Bare 1441.28μM and curve (d) Mod 1441.28μM; (C) CV test calibration curve; (D) DPV; (E) DPV referring to curve (a) Bare 0μM, curve (b) Mod 0μM, curve (c) Bare 1441.28μM and curve (d) Mod 1441.28μM; (F) DPV test calibration curve; (G) LSV: referring to curve (a) Bare 0μM, curve (b) Mod 0μM, curve (c) Mod 23.94 μM, curve (d) Bare 1441.28μM, curve (e) Mod 461.65μM and curve (f) Mod 1441.28μM; (H) LSV Summary: referring to curve (a) Mod 0μM, curve (b) Bare 0μM, curve (c) Mod 23.94μM, curve (d) Bare 1441.28μM and curve (e) Mod 1441.28μM; (I) Chronoamperometry; (J) Chronoamperometry test calibration curve. 105

Figure 56 – Tryptophan Validation: (A) pH; (B) pH Summary; (C) Repeatability; (D) Repeatability Summary; (E) Reproducibility; (F) Reproducibility Summary; (G) Stability; (H) Stability Summary. 106

Figure 57 – Cysteine Detection: (A) CV; (B) CV referring to curve (a) Bare 0μM, curve (b) Mod 0μM and curve (c) Mod 2447.13μM; (C) CV test calibration curve; (D) DPV; (E) DPV zoom; (F) DPV test calibration curve; (G) LSV: referring to curve (a) Bare 0μM, curve (b) Mod 0μM, curve (c) Mod 138.06μM, curve (d) Mod 601.5μM, curve (e) Bare 2447.12μM, curve (f) Mod 2088.6μM and curve (g) Mod 2447.12μM; (H) LSV Summary: referring to curve (a) Bare 0μM, curve (b) Mod 0μM, curve (c) Mod 138.06μM, curve (d) 601.5μM and curve (e) Mod 2447.12μM; (I) Chronoamperometry; (J) Chronoamperometry test calibration curve. 107

Figure 58 – Cysteine Validation: (A) pH 2 to pH 7; (B) pH 2 to pH 5; (C) pH Summary; (D) Repeatability; (E) Repeatability Summary; (F) Reproducibility; (G) Reproducibility Summary; (H) Stability; (I) Stability Summary. 108

Figure 59 – Pyridoxine Detection: (A) CV; (B) CV referring to curve (a) Bare 0μM, curve (b) Mod 0μM, curve (c) Bare 1441.29μM and curve (d) Mod 1441.29μM; (C) CV test calibration curve; (D) DPV; (E) DPV referring to curve (a) Bare 0μM, curve (b) Mod 0μM, curve (c) Bare 1441.29μM and curve (d) Mod 1441.29μM; (F) DPV low concentrations; (G) DPV test calibration curve; (H) LSV: referring to curve (a) Bare 0μM, curve (b) Mod 0μM, curve (c) Mod 23.94μM, curve (d) Mod 122.48μM, curve (e) Mod 461.65μM, curve (f) Bare 1441.29μM and curve (g) Mod 1441.29μM; (I) LSV summary referring to: curve (a) Bare 0μM, curve (b) Mod 0μM, curve (c) Mod 122.48μM, curve (d) Mod 461.65μM and curve (e) Mod 1441.29μM; (J) Chronoamperometry; (I) Chronoamperometry test calibration curve. 109

Figure 60 – Pyridoxine Validation: (A) pH; (B) pH Summary; (C) Repeatability; (D) Repeatability Summary; (E) Reproducibility; (F) Reproducibility Summary; (G) Stability; (H) Stability Summary. 110

Figure 61 – PTB electrode analyte detection scheme. Figure produced by the author using artificial intelligence tools. 111

Figure 62 – Simultaneous analyte detection: (A) PBCB electrode for the detection of AA, AU, G, A and T; (B) PBP electrode for the detection of CC, RS and HQ; and (C) PBP electrode for the detection of AP and HZ. 113

Figure 63 – Detection of real samples: (A) Lagoon in a residential neighborhood in Volta Redonda - RJ; (B) pH 7.32 of the lagoon water; (C) Rodrigo de Freitas Lagoon - Rio de Janeiro; (D) pH 6.61 of the Rodrigo de Freitas Lagoon water; (E) Paraíba do Sul River in Volta Redonda and (F) pH of the Paraíba do Sul River water. 115

Figure 64 – Detection of real samples: (A) AP in river water; (B) HZ in CV river water; (C) AP in Rodrigo de Freitas lagoon water; (D) HZ in Rodrigo de Freitas lagoon water; (E) AP in lagoon water; (F) HZ in lagoon water; (G) AP and HZ in river water. 116

Figure 65 – Detection of real samples (Urine): (A) CV AU; (B) CV AA; (C) CV guanine; (D) CV adenine; (E) CV thymine; (F) Urine without analyte; (G) Amplification of the detection peak of urine without analyte; (H) Simultaneous detection of analytes detected by the PCBC electrode. 118

LIST OF TABLES

Table 1 – Cut-off according to ISO 4288 standard. 27

Table 2 – Table of critical values for Dixon's Q test for an outlier (adapted from [72]). 37

Table 3 – Table of critical values for the Grubbs test for an outlier (adapted from[73]). 37

Table 4 – Materials used in PBS and key information. 38

Table 5 – Analytes and technical information regarding quantities used and dilution. 47

Table 6 – Compilation of information from tests performed with analytes detected by the PBCB electrode. 69

Table 7 – Compilation of information from validation tests with analytes detected by the PBCB electrode. 70

Table 8 – Compilation of information from tests performed with analytes detected by the PBP electrode. 83

Table 9 – Compilation of information from validation tests with analytes detected by the PBP electrode. 84

Table 10 – Compilation of information from tests performed with analytes detected by the PTB electrode. 98

Table 11 – Compilation of information from validation tests with analytes detected by the PTB electrode. 99

Table 12 – Comparison of analyte detection results with the literature. 120

LIST OF ABBREVIATIONS

A	Adenine
AA	Ascorbic Acid
AFM	Atomic Force Microscope
AP	Pyrogallic Acid
AU	Uric Acid
BCB	Brilliant Cresyl Blue
BP	Bromophenol Blue
CA	Chronoamperometry
CC	Catechol
CE	Counter Electrode
CT	Cysteine
CV	Cyclic Voltammetry
DPV	Differential Pulse Voltammetry
EP	Peak Detection Voltage Or Peak Potential
FTIR	Fourier Transform Infrared Spectroscopy
G	Guanine
GS	Grubbs Test
HQ	Hydroquinone
HZ	Hydrazine
INI	Initial
IP	Peak Current
IPA	Anodic Peak Current
LAFEA	Laboratory Of Experimental And Applied Physics
LD	Detection Limit
LQ	Limit Of Quantification
LSV	Linear Sweep Voltammetry

MOD	Modified Electrode
PBCB	Polymerized Brilliant Cresyl Blue
PBP	Polymerized Bromophenol Blue
PBS	Phosphate Buffered Saline
PCET	Proton-coupled Electron Transfer
PD	Pyridoxine
PTB	Polymerized Thymol Blue
RE	Reference Electrode
RS	Resorcinol
RSD	Relative Standard Deviation
SEM	Scanning Electron Microscopy
T	Thymine
TB	Thymol Blue
TEM	Transmission Electron Microscope
TP	Tryptophan
TS	Tyrosine
V	Vanillin
WE	Working Electrode

CONTENTS

Introduction 14

1 Introduction 14

1.1 Objectives 15

2 Fundamental Concepts 16

2.1 Sensors 16

2.2 Electroanalytical Techniques 22

2.3 Atomic Force Microscope (AFM) 25

2.4 Scanning Electron Microscopy (SEM) and Coating 28

2.5 Transmission Electron Microscopy (TEM) 29

2.6 Fourier Transform Infrared Spectroscopy (FTIR) 32

2.7 Validation 34

2.7.1 Sensitivity 34

2.7.2 Detection range 34

2.7.3 Response time 35

2.7.4 Stability 35

2.7.5 Reproducibility 35

2.7.6 Repetitiveness 35

2.7.7 Detection Limit Detection limit (LD) and Limit of Quantification Limit of quantification (LQ) 36

2.7.8 Outlier 36

3 Materials and methods 38

3.1 Buffer solution 38

3.2 Dyes 39

3.2.1 Brilliant Cresyl Blue 40

3.2.2 Bromophenol blue 40

3.2.3 Thymol blue 40
3.3 Graphite 41
3.4 Analytes 42
3.4.1 Analytes detected by the Polymerized brilliant cresyl blue (PBCB) electrode. 42
3.4.2 Analytes detected by the Polymerized bromophenol blue (PBP) electrode. 43
3.4.3 Analytes detected by the PTB electrode. 44
3.5 General considerations for test preparation, measurement, and calculation. 47
3.6 Complex matrices 48

4 Results and discussions 50
4.1 Study of electrodes 50
4.1.1 Physical and morphological characteristics 50
4.1.1.1 AFM Analyses 50
4.1.1.2 SEM analyses 51
4.1.1.3 TEM Analysis 53
4.1.1.4 FTIR analysis 54
4.1.2 Electrochemical Characterizations of the Electrodes 57
4.1.2.1 PBCB electrode study 57
4.1.2.2 PBP electrode study 60
4.1.2.3 PTB electrode study 62
4.2 Analyte results 64
4.2.1 Electroanalytical results of analytes identified by the PBCB electrode 66
4.2.2 Results of analytes identified by the PBP electrode. 82
4.2.3 Results of analytes identified by the PTB electrode. 97
4.2.4 Simultaneous detection 112
4.2.5 Real samples 114
4.2.6 Comparison with the literature 119

Final considerations 119
4.3 Future Perspectives 123

References 124

1- Introduction

Sensors and biosensors are essential tools of contemporary engineering, widely used in various technological applications [1], healthcare [2], agriculture [3], industry [4], among others. Throughout history, sensors have undergone significant milestones that contributed to the development of modern sensing technology. Although it is difficult to identify a single event as the "invention" of the first sensor, the concept of sensing dates back to ancient times, with simple devices used to detect environmental changes. Biosensors, in turn, are more recent devices [5], with the first reference to such devices recorded in 1962 [6], when Leland C. Clark Jr. and Champ Lyons described the development of an enzyme-based oxygen sensor. This sensor enabled continuous measurement of oxygen in biological systems, such as blood, and is considered the precursor of modern biosensors.

The evolution of sensors and biosensors has been marked by the use of various combinations of biomaterials and sensing elements, enabling the manufacture of sensors for detecting different analytes. The continuous development of new sensors is driven by the need to improve the accuracy, selectivity, and reliability of measurements, to detect new analytes, and to integrate these emerging technologies. These advances have an important impact on areas such as health, safety, sustainability, and technological innovation.

This thesis addresses sensing devices that use graphite as a transducer and three different types of dyes as receptor elements: Brilliant Cresyl Blue (BCB), bromophenol blue (BP), and thymol blue (TB). These dyes are used separately and developed via electropolymerization, using the cyclic voltammetry technique in LaFEA. Each sensor produced is capable of recognizing a specific group of analytes: the PBCB sensor detects Guanine (G), Adenine (A), Thymine (T), ascorbic acid (AA), and uric acid (AU) at different voltage potentials; the Polymerized thymol blue (PTB) sensor detects Pyridoxine (PD), Tyrosine (TS),Vanillin (V), Cysteine (CT), and Tryptophan (TP); and the PBP sensor detects Catechol (CC), Resorcinol (RS), Hydroquinone (HQ), Hydrazine (HZ), and pyrogallic acid (AP).

Due to their advantages, such as low production costs, fast response times, portability, and the ability to measure biological materials on a small scale with high sensitivity and accuracy, electropolymerized sensors have become highly important tools, offering

countless research possibilities [7]. For the detection of the analytes investigated in this study, electrochemical techniques were used, such as cyclic voltammetry (CV), linear sweep voltammetry (LSV), differential pulse voltammetry (DPV), and chronoamperometry (CA). Voltammetry is an electrochemical analytical technique employed to study the electrical properties generated by electrochemical reactions at an electrode. It involves applying a controlled electrical potential to the electrode and the measurement of the resulting current, providing valuable information about the characteristics of the electrochemical reaction. The name "voltammetry" derives from the fact that the technique is based on varying the applied potential (voltage) to obtain this information.

In addition to the electrochemical techniques mentioned, characterization of the electrodes was also carried out by means of scanning electron microscopy (SEM), atomic force microscopy atomic force microscope (AFM), and Fourier-transform infrared spectroscopy (FTIR). These techniques are essential for analyzing the structural, morphological, and chemical characteristics of the materials, providing information for the development, quality control, and application of new sensor devices.

1.1- Objectives

The present thesis work has as its overall objective the development and in-depth characterization of low-cost electrochemical platforms based on graphite electrodes modified by electropolymerization of organic dyes, such as poly(brilliant cresyl blue) (PBCB), poly(bromophenol blue) (PBP), and poly(thymol blue) (PTB). The aim is to explore and optimize the electrocatalytic and molecular recognition properties of these polymeric films for the simultaneous and selective detection of a wide range of analytes of biological and environmental relevance, including purines (guanine and adenine), pyrimidines (thymine), phenols (catechol, resorcinol, hydroquinone, pyrogallol acid), hydrazine, amino acids (tyrosine, tryptophan and cysteine), and vitamins (ascorbic acid, pyridoxine and vanillin). The research thus seeks to enhance the capacity for data collection and analysis in electrochemical sensing systems, combining high analytical performance with sustainability and cost reduction, in line with the growing demand for efficient and accessible analytical technologies.

2- Fundamental Concepts

In this chapter, the fundamental concepts of sensors, electrode construction, voltammetry techniques, image analysis techniques, and the validation concepts used in this work are presented.

2.1- Sensors

A sensor is a device that detects or measures a physical or chemical quantity and converts this information into a measurable or processable signal, playing a fundamental role in a wide variety of applications, from industrial control systems to medical devices. They are classified into different types based on their applications, input signals, conversion mechanisms, materials used, and sensor characteristics, such as cost, accuracy, or range [8].

The basic structure of a sensor consists of three main components: the receptor, the transducer, and the interface [9]. This structure can also be applied to specific sensors, where the receptor layer may have a different configuration, comprising one or more layers.

Figure 1 shows a schematic representation of an electrochemical sensor and its respective basic units. The receptor is the chemically active part of the sensor, that is, the part of the system responsible for specifically recognizing and binding to the analyte (target substance), whether a molecule, ion, or other type of signal. The transducer converts the signal generated by the interaction between the receptor and the target substance into a measurable signal, usually an electrical or optical signal. There are different types of transducers, including electrochemical, optical, and piezoelectric, among others. The choice of transducer depends on the properties of the target substance and on the characteristics of the sensor [10].

The receptor layer, together with the transducer, is one of the most important elements; this layer can be made from numerous materials and techniques. For this work, the electrodeposition technique was selected, and three dyes were studied separately. These dyes, when electropolymerized, form thin layers of conductive polymers. Conductive polymers are a relatively new class of materials [11] and, when exposed to certain electrolytic

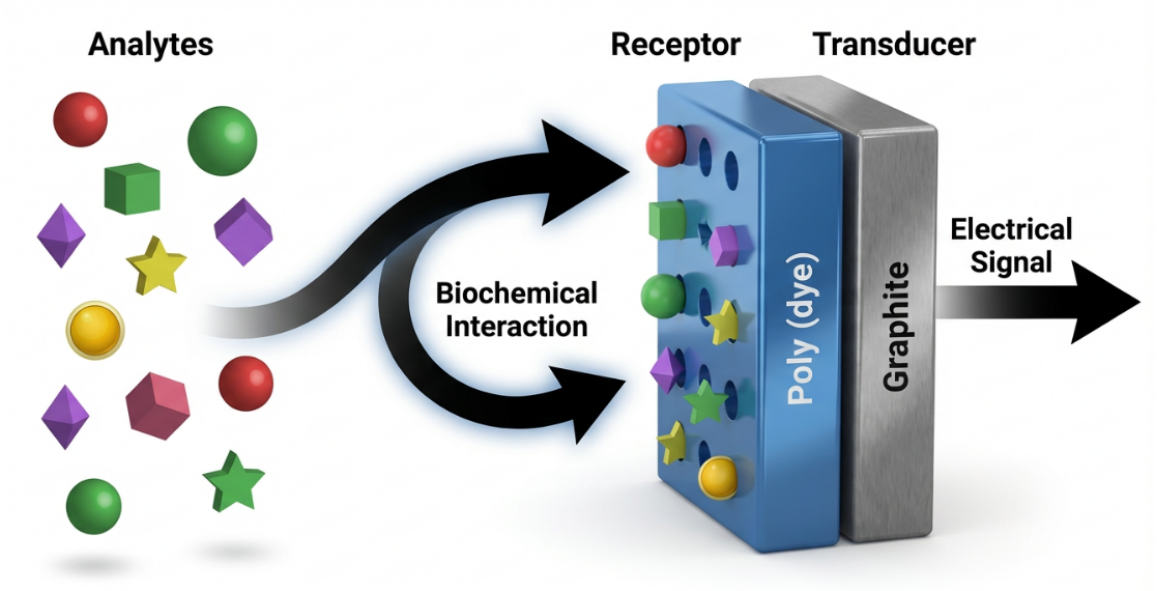


Figure 1 – Representation of the basic structure of a sensor.

solutions, they simultaneously exhibit electronic and ionic conductivity. Generally, electropolymerized materials possess unique properties that are not characteristic of the corresponding monomers [12]. Following the discovery of conductive polymers, the formation of electroactive polymers through the reduction or oxidation of organic compounds became a promising technique for the development of sensors and biosensors. Phenazines are examples of compounds that are widely used as redox indicators and mediators in a variety of fields. The general formula of phenazines can be shown as in Figure 2:

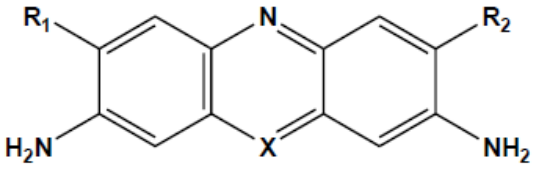


Figure 2 – Structure of phenazines [12].

where X = N, S, O are, respectively, the phenazines, phenothiazines, and phenoxazines [12]. The phenazines most commonly used in electrochemical applications in polymer form are Nile blue [13], neutral red [14], methylene blue [15], methylene green [16], brilliant cresyl blue [17], and toluidine blue [18], among others. The oxidation of the dye's functional groups during the electropolymerization process occurs due to the application of an electric current through the electrolyte solution. This process is facilitated by the presence of an

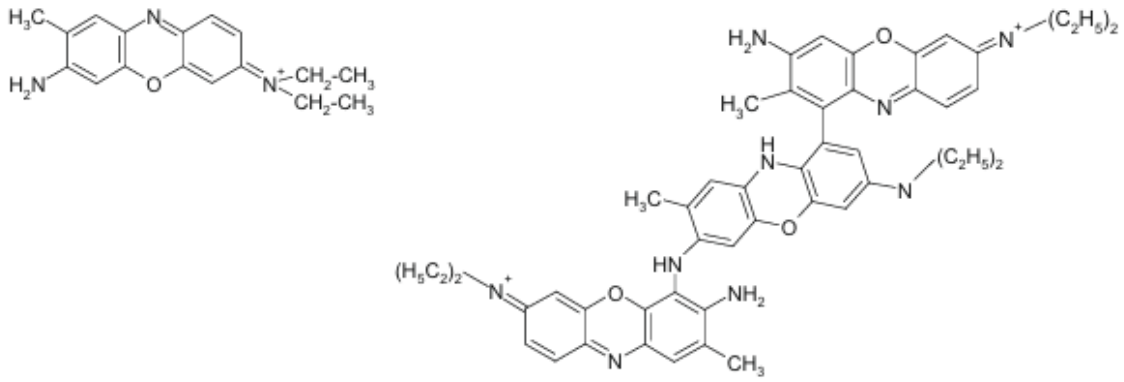


Figure 3 – Electropolymerization of BCB, Figure adapted from [19].

electrolyte in the solution, which can assist in electrical conduction and charge transfer between the electrode and the molecular species to be oxidized. Figure 3 shows this process for the PBCB electrode.

When an electric current is applied, electrons are transferred from the electrode to the dye's functional groups on the surface of the conductive substrate. This results in the oxidation of these functional groups, that is, in the loss of electrons, turning them into free radicals or positive ions. These reactive radicals or ions then initiate the polymerization reaction, bonding with each other or with other monomers present in the electrolytic solution. Figure 4 illustrates this process for the TB electrode.

Electropolymerization is evidenced by the increase in peak current attributed to monomer-type redox activity, as well as by the appearance and growth of new set(s) of peak(s) at more positive potentials [12].

In summary, the oxidation of the dye's functional groups during electropolymerization is initiated by the transfer of electrons from the electrode to the functional groups on the surface of the conducting substrate, resulting in the formation of reactive radicals or ions that initiate the polymerization reaction. This process is important for the formation of polymer films from the dye. Figure 5 shows this process for the PBP electrode.

At the electrode interface, an electropolymerization process occurs in two distinct stages: the first consists of the electrochemical step, in which radical cations of the monomers present in the electrical double layer are generated through the application of an electric potential and, consequently, a flow of current; the second stage, called the chemical step, takes place when these radical cations react with each other and with other available monomers. The sequential repetition of these stages enables the formation of a

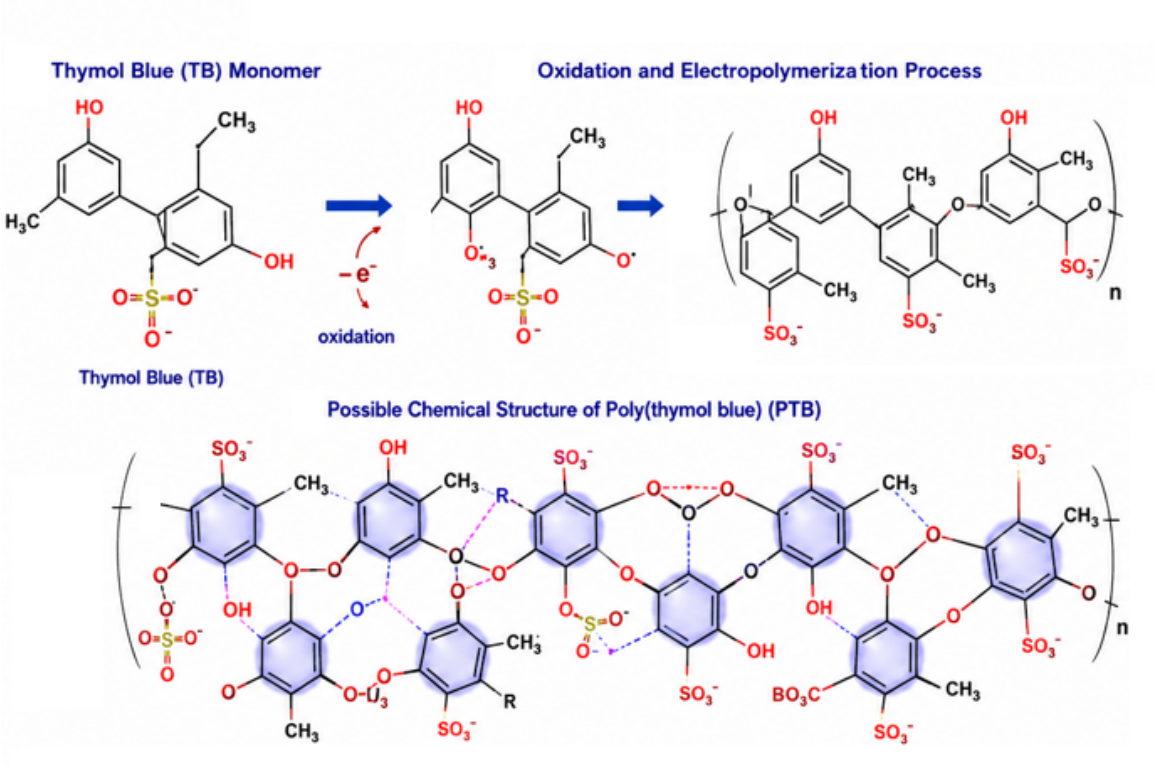


Figure 4 – Electropolymerization of TB, Figure adapted from [20]

.

polymeric film. The representation of the double layer can be seen in Figure 6.

In this thesis, the current flowing through the electrolytic solution must be controlled, and the method used for this control is cyclic voltammetry.

For analyte detection, the polymerized electrodes act as redox mediators, facilitating electron transfer between the analyte and the conducting substrate [23]. The mechanism can be described as the initial oxidation of the polymer on the electrode surface, generating an oxidized species that chemically reacts with the analyte at the interface, thereby regenerating the mediator for a new catalytic cycle. In addition, the presence of functional groups in the polymeric film allows for specific interactions, such as π-π interactions [24].

A classic mediated electrocatalysis process also occurs, in which the electroactive polymeric film acts as an intermediary in the charge transfer between the analyte and the electrode. In this context, the polymer does not behave as an inert coating but rather as an active redox mediator, capable of directly participating in the oxidation and reduction steps, providing an energetically more favorable alternative pathway for the electrochemical reaction [25]. This type of mechanism is often classified as an EC-type

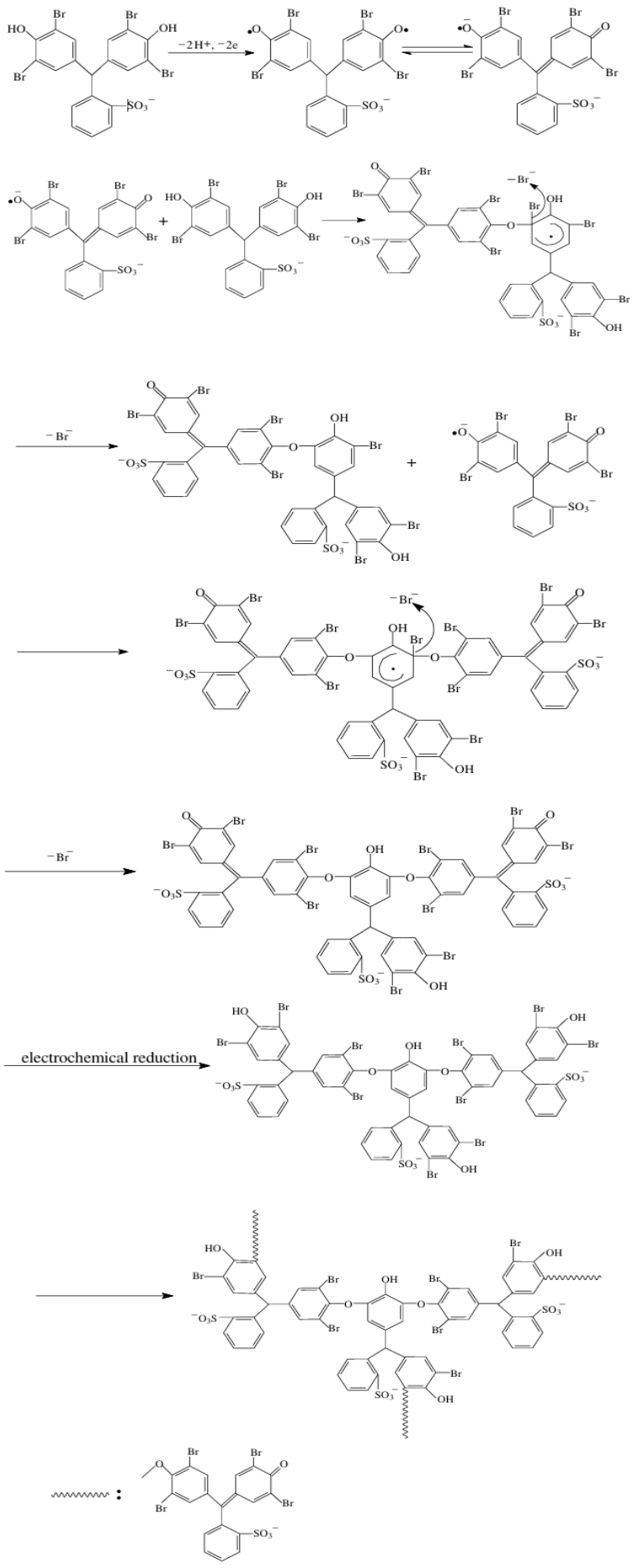


Figure 5 – Electropolymerization of BP, Figure adapted from [21].

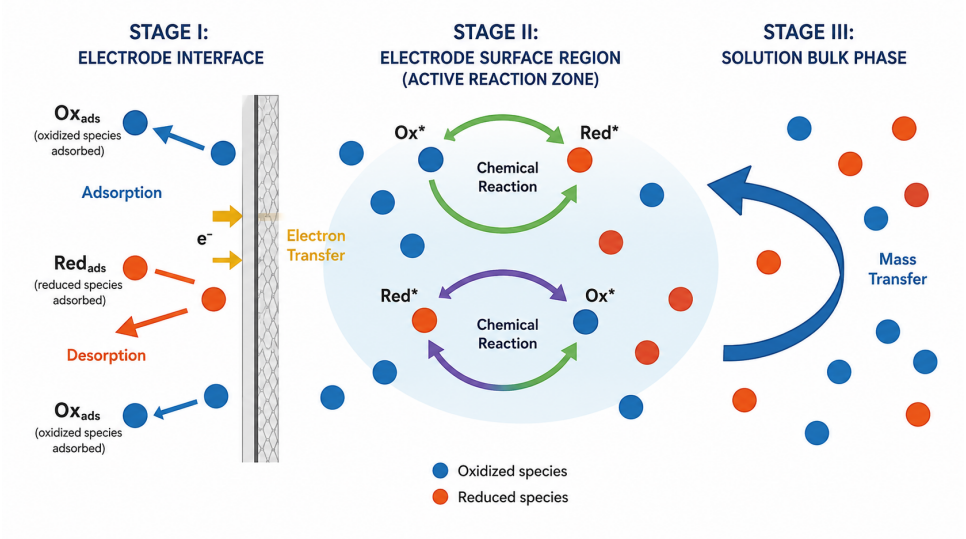


Figure 6 – Diagram showing the double layer. Figure adapted from [22] with the aid of artificial intelligence tools.

process, in which an electrochemical step is followed by a regenerative chemical step, resulting in a continuous catalytic cycle [26].

Initially, the polymer in its reduced form (P-red) undergoes oxidation at the electrode surface, releasing electrons to the external circuit and forming the oxidized species (P-ox). This step occurs at potentials lower than those required for the direct oxidation of the analyte, since the polymeric material has its own redox states that are more energetically accessible [27]. As a consequence, the modified electrode operates under milder potential conditions, significantly reducing the overpotential of the electrochemical process [28]. Next, the oxidized form of the polymer (P-ox), which is highly reactive, chemically interacts with the analyte in the solution, promoting its oxidation through electron transfer. In this process, the reduced analyte (Analyte-red) is converted into its oxidized form (Analyte-ox), while the polymer is simultaneously regenerated to its reduced form (P-red), closing the catalytic cycle.

This process is often accompanied by the release of protons, characterizing a proton-coupled electron transfer (PCET) mechanism [29], which is especially relevant for the analytes studied, such as phenolic compounds, nitrogenous bases, and biomolecules containing hydroxyl and amine groups. The involvement of protons indicates that the local chemical environment, particularly the solution pH, exerts a strong influence on the kinetics and thermodynamics of the reaction, directly affecting the peak potentials and the intensity of the electrochemical current [30]. Indeed, the maximum efficiency observed at neutral pH

suggests an ideal balance between the protonated and deprotonated forms of the analytes and the polymer's active sites, simultaneously favoring adsorption, molecular orientation, and charge transfer.

The cyclical nature of this mechanism is one of the most relevant aspects of the electrocatalytic process, since the polymer is not consumed during the reaction but is continuously regenerated [31]. This allows a single mediating unit to participate in the transfer of multiple electrons. This allows a single mediator unit to participate in multiple electron transfer events, resulting in a significant amplification of the peak current. In kinetic terms, this implies that the process is no longer limited exclusively by the diffusion of the analyte to the electrode surface, but also depends on the regeneration rate of the mediator and on the rate of the chemical reaction between the oxidized polymer and the analyte [32]. This change in the kinetic regime directly contributes to the increase in the analytical sensitivity of the sensors. From an energetic point of view, the presence of the redox mediator promotes a reduction of the overall activation barrier of the electrochemical process. Instead of a direct electron transfer between the analyte and the electrode, which often exhibits high kinetic resistance, the system begins to operate through two sequential lower-energy steps: the oxidation of the polymer and the chemical oxidation of the analyte mediated by the oxidized polymer. This unfolding of the reaction pathway makes the process more efficient, both thermodynamically and kinetically [33].

2.2- Electroanalytical Techniques

In this work, the following methods will be used: Cyclic Voltammetry - cyclic voltammetry (CV), Linear Sweep Voltammetry - linear sweep voltammetry (LSV), Differential Pulse Voltammetry - differential pulse voltammetry (DPV), and Chronoamperometry - chronoamperometry (CA)

Voltammetry is an electrochemical method based on the interaction between the working electrode surface and the thin layer of the adjacent solution. The electrochemical half-cell, shown in Figure 7, is used together with an electric current, which is controlled by applying a potential [34].

With this method, information about the analyte is obtained by measuring the magnitude of the electric current that flows between the working electrode and the reference electrode, while applying a potential difference between the working electrode and

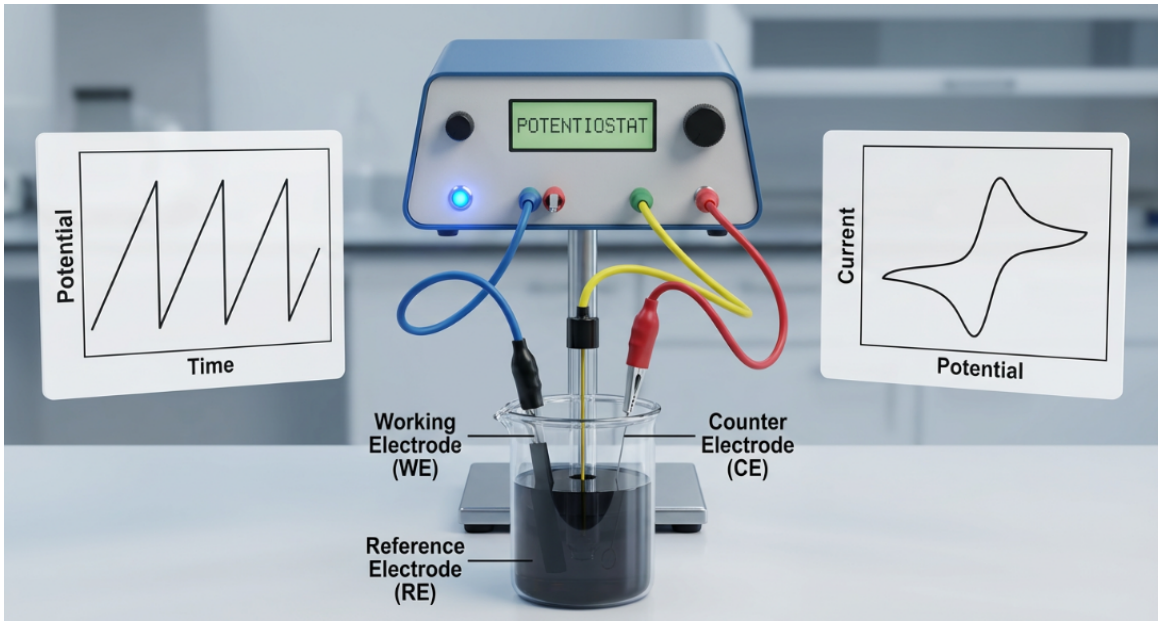


Figure 7 – Simplified diagram of the connection between electrodes and potentiostat.

the counter electrode. Figure 7 shows a simplified schematic of the connections between the electrodes and the potentiostat. The electrodes are: reference electrode (RE), working electrode (WE), and counter electrode (CE), the latter also known as the auxiliary electrode. The reference electrode used is Ag/AgCl (3.5 M KCl). It consists of a silver wire that is coated with AgCl at its lower end; this wire is inside a glass tube that has a porous material at its lower tip. Inside, the reference electrode contains a KCl solution. The reference electrode has a high impedance. The working electrode, in turn, is where the redox reaction takes place. It is in direct contact with the electrolytic solution that contains the ions or chemical species to be analyzed or studied. The equipment that controls the current passing through these electrodes is the potentiostat. The potentiostat used is an Ivium™ Compactat model, located at LaFEA, as shown in Figure 8.

Cyclic voltammetry is an electrochemical technique used to investigate the reduction and oxidation processes of molecular species, [35], and consists of linearly sweeping the potential of a working electrode (in an unstirred solution) using a triangular potential waveform. The graph generated (current vs. potential) is called a voltammogram. One of the main advantages that contributes to the popularity of cyclic voltammetry is its ease of use and adaptability. It is generally the first experiment carried out in studies aimed at analyzing the electrochemical behavior of a substance or of an electrode surface, since it allows the observation of the redox behavior of a system over a range of potentials. The type of voltammogram generated depends on the type of redox mechanism that the



Figure 8 – The potentiostat used in this work is located in LaFEA.

compound in question undergoes at the electrode [36]. These types can be divided into three groups: reversible, quasi-reversible, and irreversible reactions.

The linear sweep voltammetry used in this work is hydrodynamic voltammetry, in which the solution is stirred; in this case, the reagent is brought to the electrode surface mainly by convection. The LSV technique is based on the hydrodynamic method, which involves the movement of the solutions used as electrolyte and the forces acting on the immersed working electrode. Due to this hydrodynamics, there is an increase in electron diffusion between the electrode and the electrolyte, which is relevant for studies that show its effect on mass transfer [37].

Another voltammetric technique used in this work is differential pulse voltammetry, in which a pulse of fixed amplitude is superimposed on a linearly increasing potential ramp. The pulses occur in step-ramp type plots. Two current measurements are taken: one before the pulse is applied and the other immediately after the pulse ends. The voltammogram is constructed from the difference in current, pulse by pulse, as a function of a linear increase in voltage, and is represented as a Gaussian curve. The peak height is directly proportional to the analyte concentration.

Chronoamperometry is an electrochemical technique used to study the kinetics of electrochemical reactions. Initially, the electric potential required to reach the limiting current is determined using a voltammetric techniques, such as cyclic voltammetry, and kept constant throughout the experiment. The current is then monitored over time, and

variations in its intensity are proportional to the analyte concentration. The resulting chronoamperometric graph represents current as a function of time. In sensor development, current measurements are carried out using the same electrochemical system, with successive quantities of analytes being added [38].

The comparison between the techniques shows that no single approach is sufficient to fully characterize the performance of electrochemical sensors based on electropolymerized films. In general terms, the CV provides fundamental mechanistic information and is initially used for electropolymerization and primary detections. DPV offers higher sensitivity and lower detection limits. Hydrodynamic LSV makes it possible to evaluate performance under improved control of mass transport. Chronoamperometry is particularly suitable for studies of temporal stability and applications in continuous monitoring.

The integrated use of these techniques enables the correlation of the structural properties of the electropolymerized film with its electrocatalytic behavior, providing a solid basis for analytical validation and comparison among the different sensing platforms developed in this work.

2.3- Atomic Force Microscope (AFM)

In this technique, images are obtained by measuring the attractive or repulsive forces between the sample surface and a sharp tip that scans across it. The scanning process is performed by a piezoelectric system that moves the tip along the x, y, and z directions with sub-nanometer precision, controlled by variations in the applied voltage. To maintain constant force or height, a feedback circuit continuously adjusts the tip position [39].

Because the interaction forces are typically on the order of 10^{-12} N, an ultrasensitive detection system is required. To measure such forces, the tip is mounted at the end of a cantilever with a low spring constant, allowing the detection of deflections caused by tip–sample interactions. An optical system composed of a laser and a photodetector is used to monitor the cantilever deflection as a function of surface topography [40]. Figure 9 shows a simplified schematic representation of an AFM system.

The atomic force microscope used in this work is from the brand EasyScan Nanosurf™, which is located in the LaFEA laboratory, as shown in Figure 10.

The main sensing elements of an AFM are the cantilever and the tip. The tip,

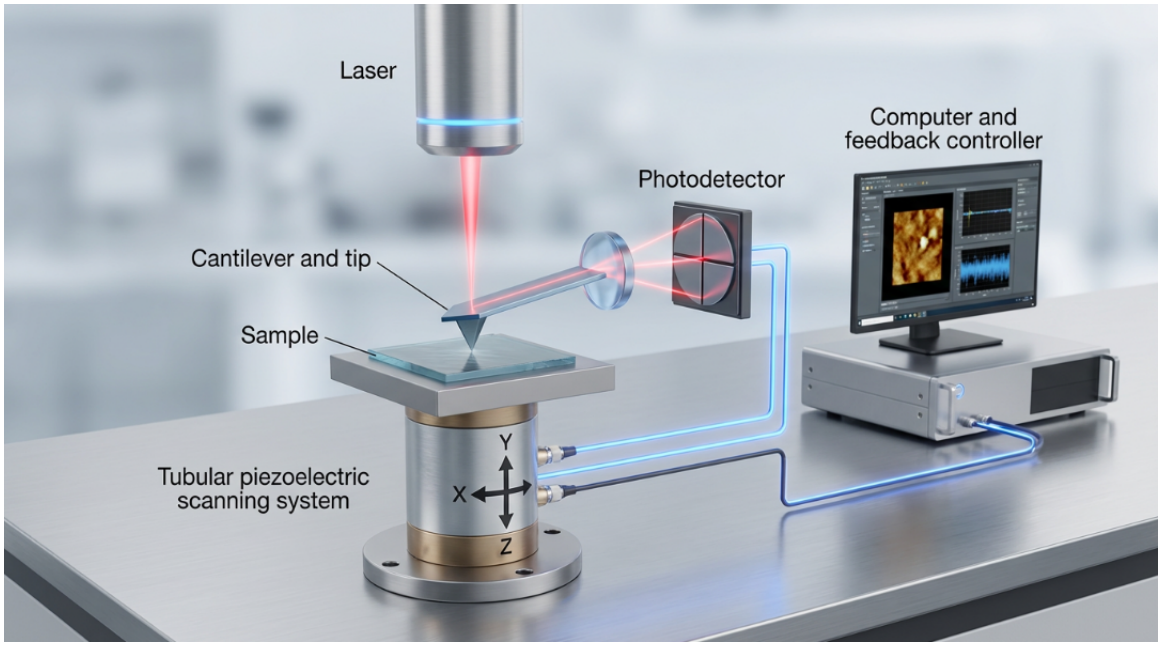


Figure 9 – Simplified diagram of the AFM
Figure adapted from [41].

located at the free end of the cantilever, is responsible for scanning the sample surface, while the cantilever measures the interaction forces. To obtain topographical images, the tip is brought into continuous or intermittent contact with the surface and scanned laterally. Cantilevers are typically fabricated from silicon or silicon nitride, with lengths ranging from 100 to 500 μm and thicknesses between 0.5 and 5 μm. The tip length is typically a few micrometers, with an apex diameter below 400 Å [42].

Atomic force microscopy can operate in different modes, which are mainly distinguished by the nature of the interaction between the tip and the sample surface during scanning. This interaction governs the acquisition of topographical and morphological information at the nanometric scale, and the choice of operating mode strongly influences image quality and sample integrity [43]. The three main AFM operating modes are contact mode, tapping (intermittent contact) mode, and non-contact mode.

In this work, the contact mode was employed. In this mode, the tip remains in continuous contact with the sample surface during scanning, and the topography is obtained from the cantilever deflection caused by repulsive forces between the tip and the surface.

ISO 16610 [44] describes geometrical product specifications (GPS) and filtration methods for surface texture analysis. These standards provide guidelines for the application of filters to reduce the bandwidth of the measured signal, enabling correlation with

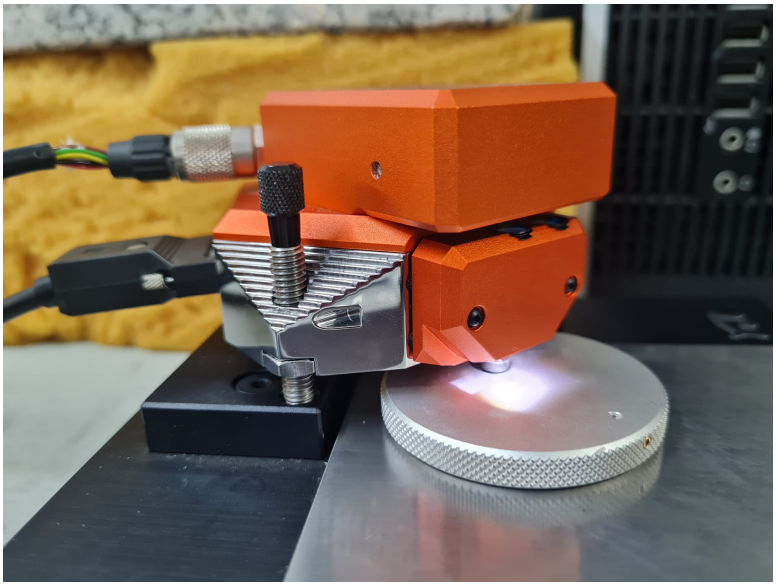


Figure 10 – The atomic force microscope at LaFEA.

physical phenomena such as friction, wear, and adhesion. For example, filters can be used to separate roughness and waviness components of the primary profile or to perform multiscale decomposition to identify the scale at which specific phenomena occur.

According to ISO 16610 [44], the measured surface topography consists of three components: form, waviness, and roughness. The separation of these components is achieved using Gaussian filters defined by a cut-off wavelength. This cut-off represents the limiting wavelength of the filter and determines which surface features are included in the roughness evaluation and which are excluded as waviness.

The ISO 4288 standard [45] specifies the appropriate cut-off values based on the average roughness (R_a), for non-periodic profiles as summarized in Table 1.

Table 1 – Cut-off according to ISO 4288 standard.

R_a (μm)	Cut-off (mm)
$0.006 < R_a \leq 0.02$	0.08
$0.02 < R_a \leq 0.1$	0.25
$0.1 < R_a \leq 2$	0.8
$2.0 < R_a \leq 10$	2.5
$10 < R_a \leq 80$	8.0

In this work, surface roughness was calculated after applying a Gaussian filter with a cut-off of 0.25 mm.

Surface roughness is a fundamental parameter in the morphological characteriza-

tion of electrodes, as it directly influences the electroactive area, the adsorption of species, and, consequently, the electrochemical performance of the sensor [46].

Among the most commonly used parameters to describe surface topography, the arithmetic mean roughness (R_a) and the root mean square roughness (R_q), defined according to ISO 4287 [47], are widely employed. The R_a parameter is defined as the arithmetic mean of the absolute values of the profile height deviations from the mean line over the sampling length and is commonly used as a general indicator of surface irregularity.

In contrast, the R_q parameter, also known as root mean square (RMS) roughness, is defined as the square root of the mean of the squared profile height deviations from the mean line, making it more sensitive to pronounced peaks and valleys on the surface [48].

2.4- Scanning Electron Microscopy (SEM) and Coating

The Scanning Electron Microscopy (SEM) makes it possible to analyze organic and inorganic materials on scales ranging from nanometers to micrometers. The SEM operates at high magnifications, reaching up to 300.000× and even 1.000.000× in modern models [49].

The scanning electron microscope operates by emitting electron beams from a tungsten filament (negative electrode) through the application of a potential difference that ranges from 0.5 to 30 kV. This variation in voltage controls the speed of the electrons and also heats the filament. The positive electrode, relative to the microscope filament, strongly attracts the generated electrons, accelerating them toward it. The trajectory of the beams is adjusted by the condenser lenses, which align them toward the objective aperture. The objective lens, in turn, focuses the electron beam before it reaches the sample for analysis. Figure 11 shows a simplified diagram of how the SEM works.

For SEM analyzes, samples must be small enough to fit on the sample stage and may require special preparation to increase their electrical conductivity and stabilize them so that they can withstand the high-vacuum conditions and the high-energy electron beam. Because the electron beam must interact with the sample, some electrons are absorbed by the sample, which must conduct them to ground. Therefore, the samples need to be conductive. If this is not the case, they can be made conductive by various physical processes, such as evaporation or ion deposition (sputtering). Another reason for coating the samples is that the deposited layers can increase electron emission, since they emit more

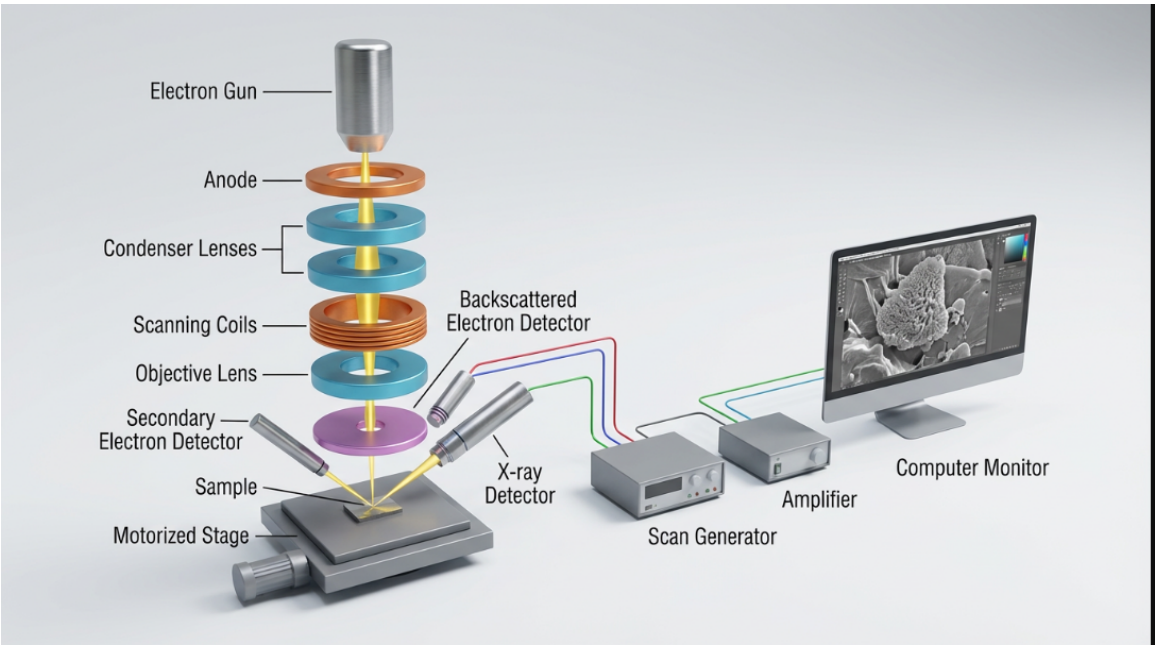


Figure 11 – Schematic diagram of a scanning electron microscope (SEM). Adapted from [50].

electrons than the sample material, facilitating image formation [51]. The Scanning Electron Microscope used in this work is a Jeol™JSM-7100F model, from the High-Resolution Electron Microscopy Laboratory (LaMAR) at Universidade Federal Fluminense (UFF). This equipment is shown in Figure 12.

For this work, the S3 Alliance™G20 Ion Sputter Coater coating machine from the High-Resolution Electron Microscopy Laboratory (LaMAR) of the Universidade Federal Fluminense (UFF) was used, as shown in Figure 13.

2.5- Transmission Electron Microscopy (TEM)

Transmission Electron Microscope (TEM) operates based on the interaction of a high-energy electron beam with an ultrathin sample. Unlike optical microscopes that use photons, TEM employs electrons, which have a much shorter wavelength, allowing for significantly higher resolutions on the order of angstroms [52]. An electron beam is generated by an electron gun (usually a tungsten filament or a field emission source) and accelerated by a high voltage (typically 80–300 kV). This beam is then focused and collimated by electromagnetic lenses to impinge on the sample. As the electrons pass through the sample, they interact with the atoms in different ways: some are scattered



Figure 12 – The Scanning Electron Microscope of the High-Resolution Electron Microscopy Laboratory (LaMAR) at the Universidade Federal Fluminense (UFF).

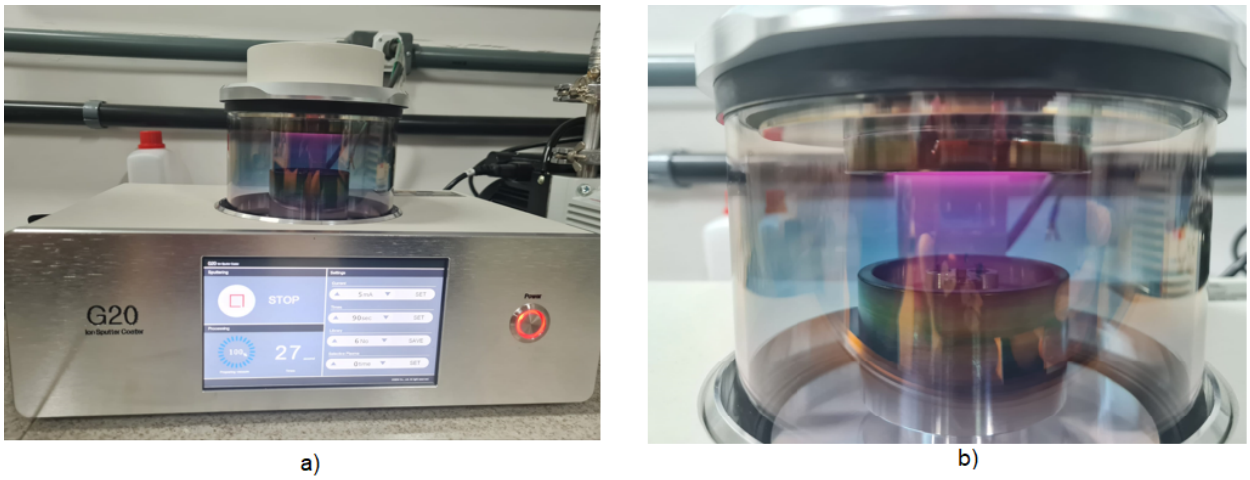


Figure 13 – Coating machine of the High Resolution Electron Microscopy Laboratory (LaMAR) of the Universidade Federal Fluminense (UFF): (a) Coating machine; (b) Coating chamber.

elastically (without energy loss), others inelastically (with energy loss), and some are transmitted directly [53]. The transmitted and scattered electrons are collected by an objective lens system and projected to form an enlarged image on a detector. Image formation in TEM can occur through mass–thickness contrast, diffraction contrast, or phase contrast, depending on the predominant interactions and the acquisition conditions [54]. One of the critical aspects of obtaining high-quality TEM images is proper sample preparation. In order for the electrons to pass through the sample and form an image, it must be extremely thin, typically with a thickness below 100 nm, and preferably in the range of 10–50 nm for high resolution [55].

There are several sample preparation techniques; the most common methods include ultramicrotomy, focused ion beam (FIB), and dispersion. For this work, the FIB technique was used. This technique is employed to prepare precise cross-sections of specific regions of the electrode. An ion beam (usually Ga+) is used to remove material and create a thin lamella, which is then transferred to a TEM grid [56].

The Transmission Electron Microscope used in this work is a Jeol™ model JEM-2100F, Figure 14 (A), and the FIB is a TESCAN AMBER™, Figure 14 (B), both from the High-Resolution Electron Microscopy Laboratory (LaMAR) at the Universidade Federal Fluminense (UFF).



(A) (B)

Figure 14 – High Resolution Electron Microscopy Laboratory (LaMAR) of the Universidade Federal Fluminense (UFF): (A) TEM; (B) FIB.

2.6- Fourier Transform Infrared Spectroscopy (FTIR)

Fourier-transform infrared spectroscopy is a technique used for the identification of functional groups, analysis of chemical bonds, and evaluation of structural modifications in materials. It is based on the interaction between infrared radiation and matter. When a sample is irradiated with infrared light in the range of approximately 4000 to 400 cm ^{1}, selective absorption of the radiation occurs due to specific vibrational modes of the chemical bonds present in the material. Each type of bond has characteristic vibrational frequencies, resulting in a spectrum that acts as a molecular fingerprint of the sample [57].

Unlike conventional dispersive spectrometers, Fourier Transform Infrared Spectroscopy (FTIR) uses a Michelson interferometer, in which the infrared radiation is modulated by a moving mirror, generating an interferometric signal in the time domain. This interferogram contains information from all frequencies simultaneously and is converted into an absorption spectrum in the frequency domain by means of the mathematical Fourier transform. This approach offers FTIR advantages such as higher spectral resolution, better signal-to-noise ratio, and shorter acquisition times [58].

There are several FTIR measurement methods that depend on the nature of the sample, the most common of which are Transmission and Attenuated Total Reflectance (ATR). In the transmission mode, the infrared radiation passes through the sample and requires transparent samples or samples prepared as KBr pellets or thin films, as shown in Figure 15.

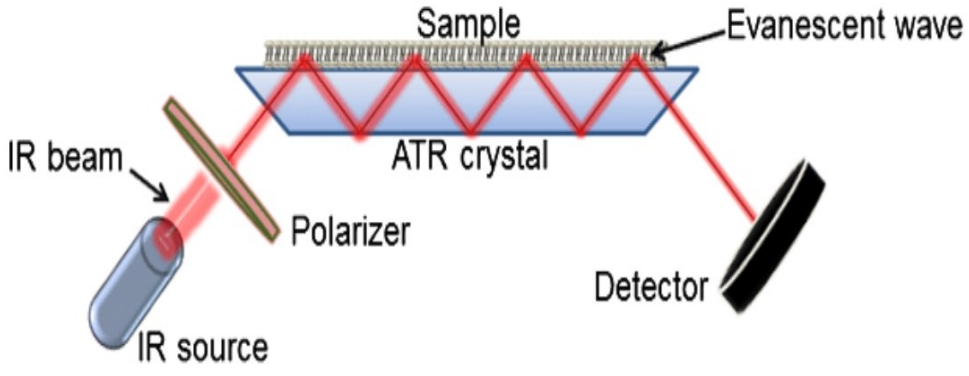


Figure 15 – Schematic representation of an ATR-FTIR system. Adapted from [59]

ATR is suitable for solid, opaque, or thin-film samples, such as electrodes. The infrared radiation is directed onto a high-refractive-index crystal (for example, diamond, ZnSe) and is internally reflected at the crystal–sample interface. An evanescent wave pen-

etrates a few micrometers into the sample, and the sample's absorption is detected. ATR is ideal for analyzing of the surfaces of electropolymerized graphite electrodes, because it requires no extensive sample preparation and allows direct analysis of the deposited polymer film.



Figure 16 – The FTIR scanner used in this study is located in the LaFEA laboratory.

For this work, the FTIR instrument from Agilent Technologies was used. ™model Cary 630 FTIR, which is located in the LAFEA laboratory, is shown in Figure 16.

2.7- Validation

The validation of analytical methods based on electrodes modified by electropolymerization is an important step to ensure the reliability, accuracy, and precision of electrochemical measurements. This process involves the systematic evaluation of several performance parameters, as recommended by regulatory agencies and international organizations such as IUPAC and ANVISA [60, 61].

2.7.1 Sensitivity

Sensitivity is defined as the slope of the calibration curve, representing the variation of the analytical signal (current or potential) as a function of the analyte concentration. A highly sensitive electrode allows the detection of small variations in analyte concentration [62]. The analytical sensitivity of the sensor is determined from the slope of the analytical curve obtained by linear regression of the peak current as a function of the analyte concentration. This parameter represents the variation of the electrochemical signal for a given concentration change and is therefore directly related to the electrode's ability to respond to small changes in the amount of analyte present in the solution. In sensors based on electropolymerized electrodes, sensitivity can be influenced by factors such as the electroactive area, the film conductivity, the charge-transfer efficiency, and possible specific interactions between the polymer and the analyte. However, to enable a more rigorous comparison between different sensing platforms—especially when they have distinct geometric areas—it is advisable to use the normalized sensitivity, defined as the ratio between the sensitivity and the electroactive area of the electrode. Normalized sensitivity, usually expressed in $\mu A\ \mu M^{-1}\ cm^{-2}$, provides an intrinsic measure of the efficiency of the active material per unit area, eliminating purely geometric effects and allowing a more accurate evaluation of the electrocatalytic performance of the polymer film.

2.7.2 Detection range

The detection range, or linear range, is the concentration interval in which the electrode response is directly proportional to the analyte concentration. For modified electrodes, the linear behavior is modeled by the linear regression equation. At high con-

centrations, saturation of the active sites of the polymer may occur, leading to deviations from linearity [63].

2.7.3 Response time

The response time is the interval required for the electrode to reach a stable value (usually 90% or 95% of the equilibrium signal) after an abrupt change in the analyte concentration. In electropolymerized films, the response time is influenced by the diffusion rate of the analyte through the polymer matrix and by the electron-transfer kinetics at the electrode/film/solution interface. Thinner and more porous films tend to exhibit faster responses [64] [65]. Electrochemical sensors are traditionally recognized for their ability to provide real-time responses, with response times typically in the range of seconds to minutes. This characteristic is one of the main advantages for dynamic monitoring applications [66].

2.7.4 Stability

Stability assesses the maintenance of the analytical signal over time. It refers to the electrode's ability to maintain its activity when stored under controlled conditions. Degradation of the polymer by oxidation can affect this parameter [67].

2.7.5 Reproducibility

Reproducibility refers to the variability between assays carried out on different independently manufactured electrodes or on different days, reflecting the robustness of the electropolymerization modification process [68].

2.7.6 Repetitiveness

Repeatability is an aspect of precision that evaluates the variability between successive measurements carried out under the same conditions, generally expressed as the relative standard deviation (RSD) of the results of replicated tests. A low RSD indicates high consistency between measurements, reflecting the intrinsic reliability of the electrode

[69]. Repeatability, reproducibility, and stability are all evaluated using the RSD.

2.7.7 Detection Limit LD and Limit of Quantification LQ

The Limit of Detection is the lowest concentration of the analyte that can be detected, but not necessarily quantified, with a given level of statistical confidence (usually 95% to 99%). The Limit of Quantification is the lowest concentration that can be measured with acceptable precision and accuracy. To calculate these limits, there are several methods. According to IUPAC, ANVISA and ICH guidelines, the limits are calculated based on the signal-to-noise ratio, the standard deviation of the blank, and the parameters of the calibration curve [70]. The method based on the parameters of the analytical curve, often referred to as straight-line extrapolation, is one of the most robust and widely used in quality control and research laboratories. It is based on the premise that the variability of the instrumental response near zero can be estimated from the data of the linear calibration curve [71]. For these calculations, quations 1 and 2 were used. The LD and LQ values were estimated from the residual standard deviation of the linear regression, using the relationships:

$$LD = \frac{3.3\text{Intercept error}}{\text{Slope}} \tag{1}$$

$$LQ = \frac{10\text{Intercept error}}{\text{Slope}} \tag{2}$$

The limit of detection was calculated using the factor 3.3, as recommended for estimates based on the linear regression of the analytical curve, considering the statistical confidence level associated with the Student's t-distribution and the residual variability of the model. The limit of quantification was calculated using the factor 10, which corresponds to a signal-to-noise ratio high enough to ensure adequate analytical precision, as recommended by IUPAC and ICH.

2.7.8 Outlier

An outlier (or discrepant value) is a data point that deviates from the other values in a set of measurements. The presence of outliers can be assessed using two statistical tests: Dixon's Q test and the Grubbs test. These tests are applied to evaluate whether one

Table 2 – Table of critical values for Dixon's Q test for an outlier (adapted from [72]).

n/Reliability	80%	85%	90%	95%	99%
5	0.557	0.602	0.642	0.710	0.821
8	0.399	0.435	0.468	0.526	0.634

Table 3 – Table of critical values for the Grubbs test for an outlier (adapted from[73]).

n/Reliability	80%	85%	90%	95%	99%
5	1.496	1.571	01.672	1.715	1.887
8	1.852	1.936	2.032	2.126	2.321

(or more) given value can be statistically considered an outlier and, if justified, removed from the analysis. For this purpose, these tests follow a confidence table: Dixon's Q test uses Table 2 and the Grubbs Grubbs Test (Gs) test uses Table 3. These parameters were calculated according to the following formulas:

$$Q = \frac{\text{gap}}{\text{Range}} \tag{3}$$

where gap is the difference between the suspicious value and the nearest neighboring value, and range is the difference between the largest and the smallest value.

$$Gs = \frac{|x_i - m|}{s} \tag{4}$$

where x_i is the suspected value, m is the mean of the values, and s is the standard deviation.

3- Materials and methods

In this chapter, the materials, preparation, and experimental procedures used in this research are presented. The experimental procedure is based on the electrochemical polymerization of dyes and on the recognition of analytes.

3.1- Buffer solution

The phosphate buffered saline (PBS) used is a saline solution of monobasic potassium phosphate KH_2PO_4 at a concentration of 0.1 M and dibasic potassium phosphate K_2HPO_4 at a concentration of 0.005 M; all these chemicals are from the supplier Êxodo®. A buffer solution is a mixture that keeps the pH of the medium under control, preventing it from changing when acids or bases are added. The saline concentration present in PBS is the same as that of the human body (isotonic solution). Table 4 presents the materials used and their main characteristics.

To increase the sensitivity of the electrode, a 0.1 mM sodium nitrate $NaNO_3$ solution was used, as mentioned in the literature [74]. The pH of this PBS solution with $NaNO_3$ was measured using the pH meter of the LAFEA laboratory, which showed a pH value of 5.5. According to research [75], [19] and studies that will be presented in Section 4.1, the ideal pH for sensor production is 7.0, thus requiring the addition of a base to raise the pH of the solution. Sodium hydroxide NaOH at a concentration of 1 M was used. The buffer solution and all experiments were prepared with distilled water.

Table 4 – Materials used in PBS and key information.

Reagents	Formula	Molar Mass (g/mol)	Density(g/cm^3)	Concentration (M)
Monobasic potassium phosphate	KH_2PO_4	136.09	2.34	0.1
Bibasic potassium phosphate	K_2HPO_4	174.2	2.44	0.005
Sodium nitrate	$NaNO_3$	84.99	2.26	0.1
Sodium hydroxide	NaOH	40	2.13	1

3.2- Dyes

All dyes shown in Figure 17 were electropolymerized in a 50 mL electrochemical half-cell containing phosphate PBS at pH 7, at room temperature of 23°C, at a concentration of 0.1 mM. As shown in the study conducted in [19], this is the concentration that presents the best result for electrodeposition, since at higher concentrations the monomer is more strongly adsorbed on the electrode surface, hindering polymer growth. For the mass calculations, the molarity formula described in Eq.5 was used.

$$Con = \frac{m_{\text{solut}}}{\text{Molar Mass} \times V_{\text{sol}}} \tag{5}$$

where m_{solut} is the mass of the solute, V_{sol} is the volume of the solution and Con is the concentration.

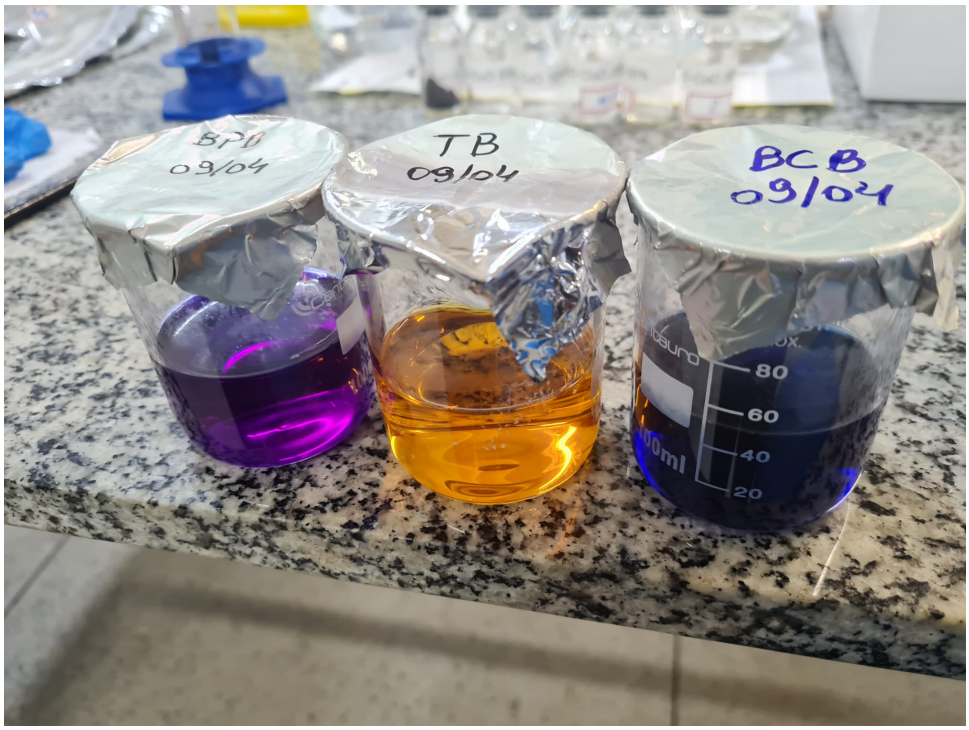


Figure 17 – Photograph of the solutions used: bromophenol blue (BPB), thymol blue (TB), and brilliant cresyl blue (BCB).

3.2.1 Brilliant Cresyl Blue

Brilliant Cresyl Blue (BCB), with the formula $C_{17}H_{20}ClN_3O$ and molar mass of 332.84 g/mol, is a dye used in electrophoresis for staining nucleic acids, facilitating the visualization of DNA and RNA in molecular biology experiments. It is a dye that belongs to a class of organic compounds widely used in various applications, including tissue staining, histological staining, and as a sensitizer in analytical detection methods. Figure 17 shows the PBS solution with BCB in blue. For the preparation of the polymerization solution, BCB at 0.1 mM (approximately 0.0017 g) was used.

3.2.2 Bromophenol blue

Bromophenol blue, $C_{19}H_{10}Br_4O_5S$, is also a dye used in various applications in research and diagnostic laboratories. It is known for its ability to stain proteins in gels, helping in the visualization and evaluation of the protein separation process. In addition, bromophenol blue is also used as a pH indicator in aqueous solutions. Its color varies depending on the pH of the medium: in acidic solutions, bromophenol blue appears yellow, while in alkaline solutions it exhibits a blue color. This color-change effect makes bromophenol blue useful for monitoring and measuring pH in a variety of aqueous systems. In Figure 17, BP in PBS solution is shown with a purple color because the solution has a pH of 7. For the preparation of the polymerization solution, BP at 0.1 mM was used (approximately 0.00335 g).

3.2.3 Thymol blue

Thymol blue $C_{27}H_{30}O_5S$ is a chemical indicator frequently used in laboratories to determine the pH of a solution. It is a blue dye that changes color depending on the pH of the medium in which it is present. In microbiology, thymol blue can be used in culture media to help distinguish different types of microorganisms. It is used in biochemical assays and tests to evaluate the presence or activity of certain enzymes and metabolic processes. In Figure 17, TB in PBS solution is shown with a yellow color, because the solution has a pH of 7. For the preparation of the polymerization solution, TB at 0.1 mM (approximately 0.00233 g) was used.

3.3- Graphite

Natural graphite is one of the allotropic forms of carbon that occur in nature, while synthetic graphite is industrially produced at high temperature and pressure in the presence of raw materials such as petroleum coke or anthracite. The two best-known forms of elemental carbon are graphite and diamond, two materials that have completely different characteristics. Graphite is an opaque material and an excellent conductor of electricity, while diamond is transparent and insulating. This breadth of possibilities is what makes carbon such an interesting element. Graphite is known for its electrical conductivity and is used in applications ranging from graphite pencils to high-tech electronics, such as lithium-ion batteries. In addition, it is an interesting material in areas such as composite materials, flexible electronics, non-stick coatings, and even medical applications. Carbon-based electrodes are generally low cost and are available in a variety of forms.



Figure 18 – Graphite used: (A) Whole graphite; (B) Enlarged image of the graphite.

The slow kinetics of carbon oxidation leads to a wide range of useful potential, especially in the anodic direction. This specification is an important advantage over metal electrodes. Carbon-based electrodes exhibit significantly lower oxidation currents compared to metal electrodes [35]. The graphite used for this work is from the supplier Sigma Aldrich™, with 99% purity and 3 mm in diameter, as shown in Figure 18 (A) and (B). PGE is one of the most popular carbon-based electrode materials for electrochemical detection of a variety of compounds. This is due to its many advantages, including high electrochemical reactivity, ease of use, good mechanical rigidity, disposability, low cost, low technology requirements, and easy replacement [76]. The cleaning and preparation of the graphite electrode initially involved mechanical cleaning (polishing) with 300-grit waterproof sandpaper, performing 10 sanding cycles in a figure-eight pattern, as shown in

Figure 19. Next, polishing was carried out with 3000-grit sandpaper and a polishing cloth, also with 10 cycles in a figure-eight pattern. After sanding, the electrode was rinsed with distilled and deionized water and placed in an ultrasonic bath for 10 min in a solution of 50% ethanol in water. Finally, the electrode was rinsed again with distilled water.

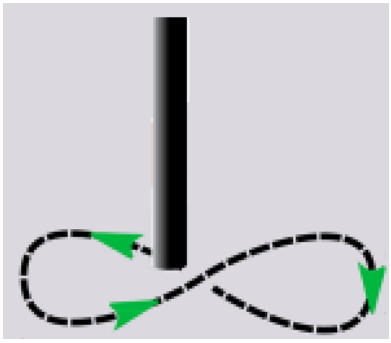


Figure 19 – Method for sanding and polishing graphite electrodes. Figure adapted from [77].

3.4- Analytes

The general information on the analytes was condensed in Table 5 and Figure 20. All analytes were used at a concentration of 0.01 M. Some analytes are not soluble in water; therefore, they were diluted by adding 1 M NaOH solution, while others were only heated, as shown in Table 5.

3.4.1 Analytes detected by the PBCB electrode.

The electrode modified with BCB was used in the detection of some analytes, such as G, A, T, AU, and AA. The nitrogenous bases G, A, and T are part of DNA. DNA plays a very important role in the maintenance of life; it is the molecule responsible for the storage and transfer of genetic information [78].

Guanine is one of the four main nitrogenous bases that make up DNA and RNA, being a purine that pairs with cytosine through three hydrogen bonds. Guanine is essential in protein synthesis, as it is involved in the genetic code that determines the sequence of amino acids in a protein [79].

Thymine is also part of DNA, being a pyrimidine that pairs with adenine through two hydrogen bonds. Damage to thymine in DNA, such as the formation of thymine

dimers due to exposure to UV radiation, can lead to mutations that are associated with the development of skin cancer.

Adenine is one of the four nitrogenous bases that are fundamental for the formation of the nucleic acids DNA and RNA. Belonging to the class of purines, adenine is characterized by a structure composed of a double ring of carbon and nitrogen [80].

AU is a chemical substance naturally produced by the human body during the metabolism of purines, which are compounds found in foods and in the cells of our organism. It is formed in the liver as a byproduct of the breakdown of purines, such as A and G [81].

AA, better known as vitamin C, is a water-soluble vitamin essential for the human body. It performs several important functions in the organism and is fundamental for maintaining health. Ascorbic acid is a powerful antioxidant that helps protect cells against damage caused by free radicals, which are unstable molecules that can contribute to cellular aging and to the development of various diseases. A growing number of studies has investigated the involvement of AA in the regulation of transcription and/or stabilization of specific mRNAs (messenger RNA) [82].

3.4.2 Analytes detected by the PBP electrode.

The BP-polymerized electrode detected several analytes: CC, RS, HQ, HZ, and AP. The CC molecule has a benzene ring with two hydroxyl (-OH) groups located at positions 1 and 2. This makes it different from other phenols, such as RS (1,3-dihydroxybenzene) and HQ (1,4-dihydroxybenzene), which have the hydroxyl groups in different positions.

CC is an organic compound belonging to the class of phenols; it is toxic to the liver and central nervous system and can disrupt DNA replication. In addition, it poses a major risk to human health and the environment worldwide [83].

The sensitive and selective detection of phenolic and nitrogen-containing compounds, such as catechol (CC), resorcinol (RS), hydroquinone (HQ), hydrazine (HZ), and pyrogallol (AP), has attracted growing interest due to the wide application of these compounds in various sectors, as well as the risks they pose to the environment and human health. These substances share the presence of redox-active functional groups (phenols or amines), which confer distinct electrochemical properties, making them relevant targets for high-precision electrochemical sensors. Catechol, resorcinol, and hydroquinone are

isomers of dihydroxybenzene, differing only in the position of the –OH groups on the aromatic ring (ortho, meta, and para, respectively) [84]. This structural difference, although subtle, significantly influences their electrochemical properties and reactivity. Catechol and hydroquinone, for example, exhibit reversible oxidation reactions, which makes them ideal models for studies of electron transfer. Resorcinol, on the other hand, tends to oxidize irreversibly, forming polymeric or quinonoid products. The simultaneous detection of these isomers requires care, demanding sensors capable of discriminating signals that are very close in potential, which drives the development of sensitive, selective materials with high resolution. Hydrazine (HZ), in turn, is a highly toxic and potentially carcinogenic compound, widely used as a reducing agent in chemical synthesis, as a propellant in aerospace systems, corrosion inhibitors, catalysts, pesticides, dyes, and pharmaceuticals [85]. Its detection is important in industrial environments and in contaminated waters. Chemically, hydrazine has a strong reducing capacity and can be easily oxidized electrochemically, forming gaseous nitrogen [86]. However, its oxidation usually occurs at high potentials, which can interfere with analytical selectivity, requiring surfaces modified with specific catalysts or nanoporous materials to reduce the oxidation overpotential. Finally, pyrogallol (3,4,5-trihydroxybenzoic acid) is a polyphenol naturally present in various foods and plants, widely recognized for its antioxidant properties [87]. Due to the presence of three phenolic hydroxyl groups, it exhibits intense redox behavior and a complex interaction with sensor surfaces. In addition to its beneficial role in health, pyrogallol is also used as a quality marker in plant extracts and can serve as a model in the evaluation of antioxidant capacity in natural matrices. Its detection is important both pharmaceutically and environmentally, as it can indicate the presence of phenolic compounds in wastewater.

3.4.3 Analytes detected by the PTB electrode.

The detection of bioactive compounds such as pyridoxine, tyrosine, vanillin, cysteine, and tryptophan is of great relevance in the fields of human health and environmental monitoring. These molecules, although belonging to different chemical classes, share properties that justify the development of sensitive analytical methods for their quantification in complex matrices. Structurally, they stand out for containing aromatic, phenolic, thiol, or heterocyclic functional groups, which give them distinct and important electrochemical and biological characteristics. Pyridoxine, known as vitamin B6, is a pyridine substituted

with hydroxyl and methyl groups, exhibiting water solubility and redox properties [88]. Its deficiency can lead to neurological disorders, while an excess, usually due to unregulated supplementation, is associated with peripheral neuropathies. The detection of pyridoxine is therefore important both for the clinical assessment of nutritional status and for the quality control of fortified foods and pharmaceuticals. Tyrosine, an aromatic amino acid with a free phenolic group, is a precursor of neurotransmitters such as dopamine, norepinephrine, and epinephrine [89]. Tyrosine levels are strongly associated with central nervous system activity, oxidative stress, and metabolic disorders such as phenylketonuria. Therefore, its detection is important in studies of metabolism and neurodegenerative diseases. Vanillin, in turn, is an aromatic phenolic aldehyde widely used as a natural or synthetic flavoring agent [90]. Its aldehyde functional group, in conjugation with the phenolic hydroxyl, confers characteristic electrochemical activity. Although it is safe at the usual concentrations found in foods, its presence in industrial effluents resulting from chemical synthesis may pose an ecotoxicological risk, as well as serve as a marker of contamination by phenolic compounds in the environment. Thus, vanillin assumes importance as a tracer analyte in environmental monitoring. Cysteine is a sulfur-containing amino acid whose main chemical feature is the highly reactive thiol (-SH) group, capable of forming disulfide bonds (S–S), which are essential for the three-dimensional stability of proteins [91]. In the body, it acts as a precursor of glutathione and is involved in antioxidant defense processes. Its detection is essential in studies of redox stress, inflammation, and diseases related to cellular oxidation. In the environment, sulfur-containing compounds such as cysteine can interfere with sulfur cycles and contribute to the formation of unpleasant odors in wastewater and contaminated soils. Tryptophan, another aromatic amino acid, is the main precursor of serotonin and melatonin, hormones that regulate mood, sleep, and behavior. The concentration of tryptophan in biofluids is associated with sleep disorders, depression, and neuropsychiatric diseases. Furthermore, its detection in sanitary effluents can be used as an indicator of human activity, being useful in studies of urban pollution and environmental epidemiology. Thus, the detection of these chemical species has multiple applications, ranging from clinical monitoring of physiological and pathological conditions to the tracking of emerging pollutants in aquatic and industrial environments.

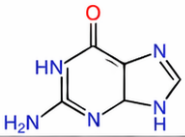
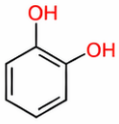
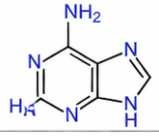
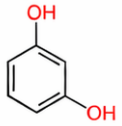
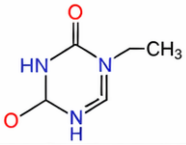
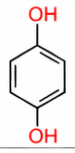
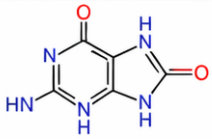
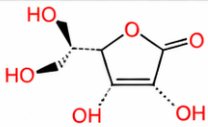
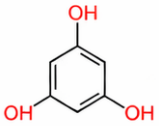
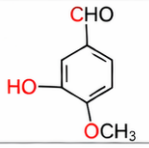
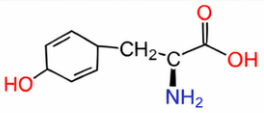
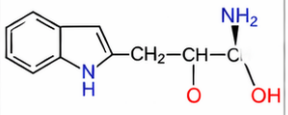
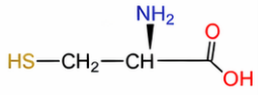
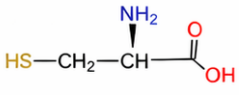
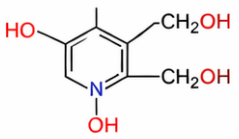
Analyte	Chemical Formula	Chemical Structure	Analyte	Chemical Formula	Chemical Structure
Guanine	$C_5H_5N_5O$		**Catechol**	$C_8H_6O_2$	
Adenine	$C_5H_5N_5$		**Resorcinol**	$C_8H_6O_2$	
Thymine	$C_5H_6N_2O_2$		**Hydroquinone**	$C_8H_6O_2$	
Uric Acid	$C_5H_4N_4O_3$		**Hydrazine**	N_2H_4	
Ascorbic Acid (Vitamin C)	$C_6H_8O_6$		**Pyrogallol** (Pyrogallic acid)	$C_8H_6O_3$	
Vanillin	$C_8H_8O_3$		**Tyrosine**	$C_9H_{11}NO_3$	
Tryptophan	$C_{11}H_{12}N_2O_2$		**Cysteine**	$C_3H_7NO_2S$	
Cisteína (Cysteine)	$C_3H_7NO_2S$		**Piridoxina** (Pyridoxine, Vitamin B6)	$C_8H_{11}NO_3$	

Figure 20 – Analytes and chemical structure.

Table 5 – Analytes and technical information regarding quantities used and dilution.

Analytes	Formula	Molar Mass (g/mol)	Mass (g)	Dilution	Supplier
Guanine	$C_5H_5N_5O$	151.13	0.0756	Added NaOH	Sigma Aldrich™
Adenine	$C_5H_5N_5$	135.13	0.0676	Heated to 50°C	Sigma Aldrich™
Thymine	$C_5H_6N_5O_2$	126.113	0.0631	Water + ultrasound	Sigma Aldrich™
Uric Acid	$C_5H_4N_4O_3$	168	0.084	Added NaOH	Sigma Aldrich™
Ascorbic Acid	$C_6H_8O_6$	176.12	0.0881	Water + ultrasound	Dinâmica™
Catechol	$C_6H_8O_6$	110.11	0.055	Water + ultrasound	Neon™
Hydroquinone	$C_6H_6O_2$	110.11	0.055	Water + ultrasound	Neon™
Resorcinol	$C_6H_6O_2$	110.11	0.055	Water + ultrasound	Neon™
Hydrazine	N_2H_4	32.04	0.06506	Water + ultrasound	Dinâmica™
Pyridoxine	$C_8H_{11}NO_3$	169.18	0.10282	Water + ultrasound	Êxodo ™
Triptophan	$C_{11}H_{12}N_2O_2$	204.23	0.10211	Water + ultrasound	Neon™
Vanillin	$C_8H_8O_3$	152.15	0.07607	Water + ultrasound	Dinâmica™
Cysteine	$C_3H_7N_2O_2S$	121.16	0.08781	Water + ultrasound	Êxodo ™
Tyrosine	$C_9H_{11}N_2O_3$	181.19	0.09059	Added NaOH	Dinâmica™
Pyrogallic acid	$C_6H_6O_3$	126.11	0.06305	Water + ultrasound	Dinâmica™

3.5- General considerations for test preparation, measurement, and calculation.

According to the specific characteristics of each analyte, different preparation procedures were required (heating or addition of NaOH). Table 5 shows the characteristics, quantities, and type of preparation for each analyte. All analytes were prepared in 50 mL of distilled and deionized water at a concentration of 0.01 M, in addition to their specific preparation. All tests were carried out in a 50 mL electrochemical half-cell with PBS at pH 7, prepared as indicated in subsection 3.1 (except for the pH test, which used pH values ranging from 2 to 10). The system was stirred for 10 s at a constant speed of 600 rpm using a magnetic stir bar (*pellet*) and a magnetic stirrer, and a resting time of 20 s was allowed before starting each voltammetric analysis in all tests. For each analyte, it was necessary to adjust the potential window, since the detection potential varies according to the analyte. The CA test was carried out in PBS solution, with the addition of 0.1 mM of analyte at each step. Ten steps were performed, i.e., 10 additions of analyte, with 60 s intervals. The analysis potential of the CA test is set based on the peak potential detected in the CV test. The LSV test is a hydrodynamic test; thus, a 10 s wait was allowed only for homogenization of the analyte in the PBS solution before starting the measurement, noting that the measurement was performed with the solution under gentle stirring. The evaluations of repeatability, reproducibility, and stability were carried out by means of the CV test. The repeatability of the sensor was evaluated by means of five successive mea-

surements using the same electrode in a solution containing a given analyte concentration. Reproducibility was assessed using five different electrodes, electropolymerized under the same conditions, measuring the same concentration value. Stability was evaluated using one electrode prepared for each analyte, with measurements taken every 7 days over a period of 2 months; in other words, 8 measurements were performed with the same electrode. After the stability, repeatability, and reproducibility measurements, the Relative Standard Deviation (RSD) was calculated for each measurement. When calculating the RSDs, high values were found due to some outlying points. The presence of outliers was investigated using Dixon's Q test and Grubbs' test for a set of five measurements of reproducibility and repeatability; for stability, a set of eight measurements was used. Dixon's Q test and Grubbs' test are recommended when the number of measurements is small $n < 10$.

In experimental analyses, outliers may arise due to several factors, such as experimental errors, instrumental failures, or sample contamination. The presence of outliers in some measurements in this work may be associated with experimental limitations of the procedure used. During the analyses, the graphite electrode must be positioned in the region of the buffer solution's surface tension both for the electrochemical measurement and for electrodeposition. Precise control of the electrode height at this interface is operationally challenging and may cause small variations in the area actually immersed or in the deposition conditions. These variations can result in fluctuations in the electrochemical response, which explains the occasional occurrence of outliers.

3.6- Complex matrices

The performance evaluation of the electrochemical electrode in real samples (complex matrices) was carried out with the aim of verifying its applicability, in which different chemical species and interferents may be present. This type of analysis is essential for validating the use of the electrode outside ideal laboratory conditions, bringing the system closer to the conditions found in environmental or biological applications.

Initially, the environmental samples were collected directly from their respective sites of origin and stored at 4°C. To evaluate the sensor's detection capability in these complex matrices, the standard addition method was employed, in which known concentrations of the analytes of interest were added to the real samples [92]. This procedure helps minimize matrix effects and makes it possible to verify whether the observed electro-

chemical response is proportional to the increase in analyte concentration in the presence of the sample's natural components.

The measurements were carried out by cyclic voltammetry, recording the current responses as a function of the applied potential.

Another complex matrix used was urine, which was collected and used immediately after collection.

4- Results and discussions

In this chapter, the results of the physical and morphological characterizations of the electropolymerized electrodes, the results of the electrochemical study of dye deposition, and the results of the analyte detections and validations are presented.

4.1- Study of electrodes

4.1.1 Physical and morphological characteristics

4.1.1.1 AFM Analyses

All images were analyzed in an area of 625 μm^2 with 256 $\times$ 256 points and 25μm $\times$ 25μm, in contact mode with a cut-off of 0.25 mm.

Figure 21 (A) shows the atomic force microscopy image of the electrode surface without deposition, and Figure 21 (B) shows the image of the electrode surface electropolymerized with BCB.

In Figure 21 (B) and 22 (A) and (B), the electrodes modified with PBCB, PBP, and PTB exhibit a rough surface topography, resulting from a homogeneous coating of the polymer on the electrode surface. In contrast, the unmodified electrode displayed a smooth surface topography. The surface roughness increased significantly after electropolymerization. The PBCB electrode showed average roughness values of Ra = 44.66 nm and Rq (root mean square – RMS) of 53.77 nm, the PBP electrode Ra = 47.69 nm and Rq = 55.13 nm, and the PTB electrode Ra = 58.32 nm and Rq = 62.43 nm, while the roughness of the unmodified electrode (RMS) was 6.48 nm, clearly indicating the uniform deposition of a thin polymeric film on the electrode surface.In this work, surface roughness was calculated after applying a Gaussian filter with a cut-off of 0.25 mm, as shown in 1.

The electrode without polymerization showed a height variation of 0.18 m, whereas the electropolymerized electrodes with BCB, BP, and TP showed height variations of 0.40 m, 0.36 m, and 0.74 m, respectively, indicating that the polymerization layer amplified

the height variation. A difference in surface morphology is also observed: the electrode without deposition has a smooth surface with some imperfections, while the surface of the electropolymerized electrode is rougher. The increase in surface roughness is directly related to the nucleation and growth of the polymer during electropolymerization; this behavior is typical of processes controlled by diffusion and charge transfer.

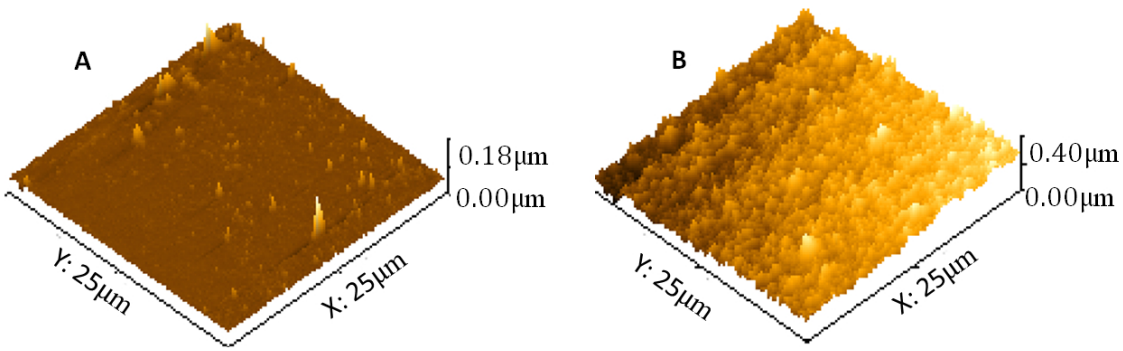


Figure 21 – AFM Image: A - AFM image for the electrode without electropolymerization; B - AFM image for the electrode electropolymerized with BCB.

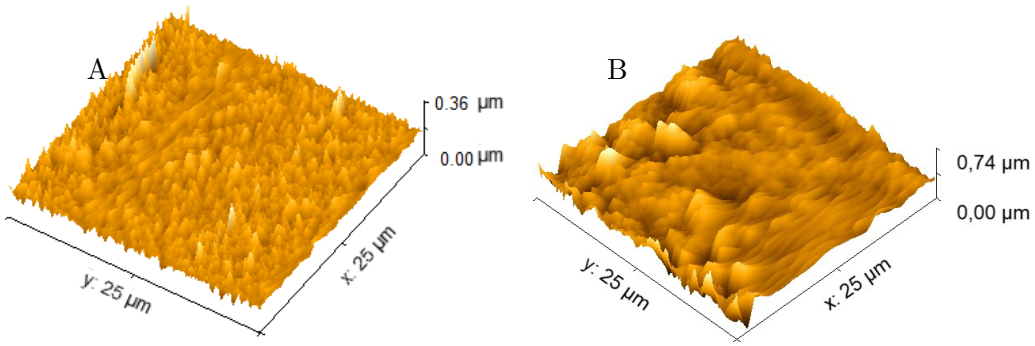


Figure 22 – AFM image: (A) - Electrode electropolymerized with BP and (B) - Electrode electropolymerized with TB.

4.1.1.2 SEM analyses

For surface characterization, scanning electron microscopy was performed on the surfaces of the electrodes with dye electropolymerization and without deposition; all samples were analyzed with a beam power of 15 kV. Figure 23 - (A) shows SEM micrographs of the electrode without deposition. Figure 23 (B) shows the PBCB electropolymerized

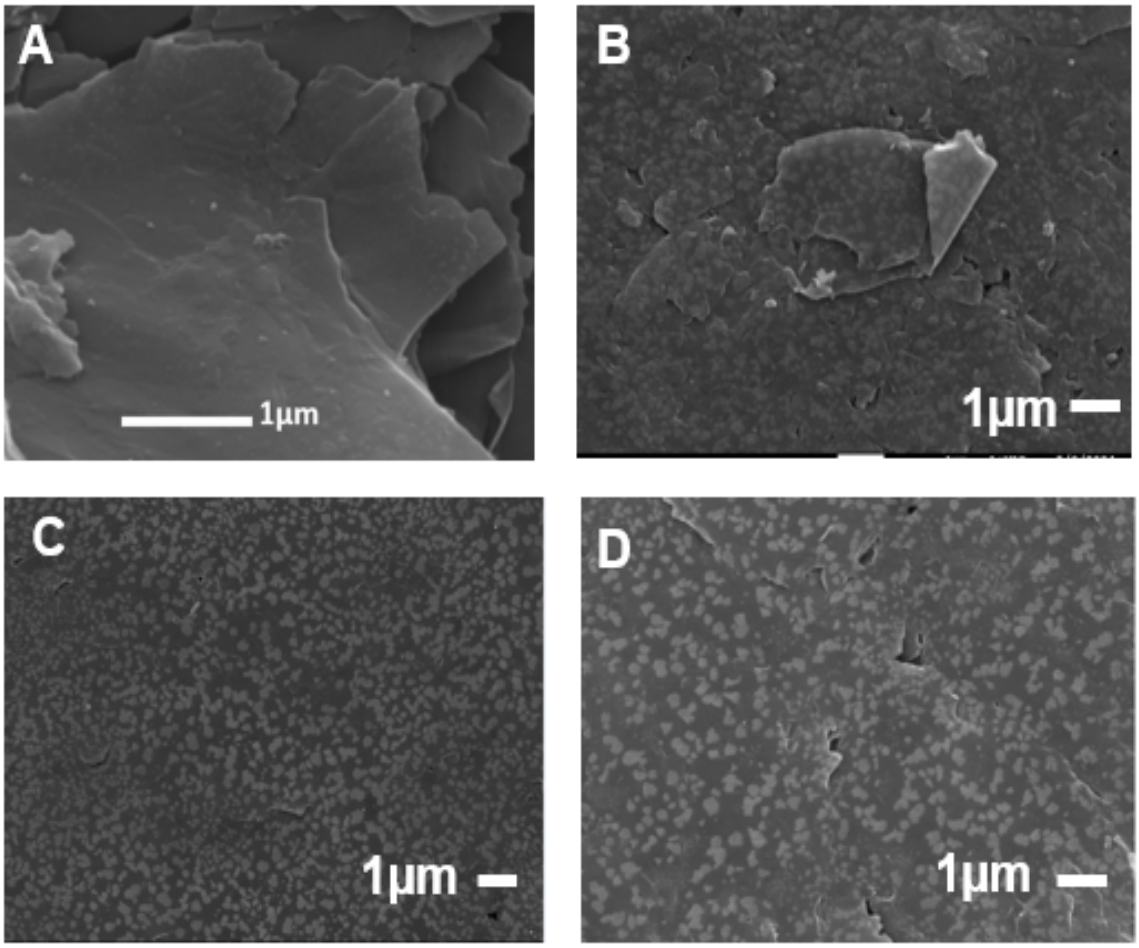


Figure 23 – Scanning electron microscopy images: (A) - Undeposed graphite with x 50000 magnification; (B) - Graphite with PBCB with × 10000 magnification; (C) - Graphite with PBP with × 5000 magnification; (D) - Graphite with PTB with × 10000 magnification.

graphite electrode at 10000× magnification. Figure 23 (C) shows the PBP electropolymerized graphite electrode at 5000× magnification. Figure 23 (D) shows the PTB electropolymerized graphite electrode at 10000× magnification. The analysis of these micrographs reveals the presence of spherical and irregular structures with a lighter coloration, dispersed over the surface of the substrate. These structures are interpreted as regions where dye polymerization occurred, forming a film. The presence of these aggregates or partially distributed structures suggests that the growth of the polymeric film occurs in a heterogeneous manner and may be associated with the initial nucleation of the polymer at specific points on the graphite surface.

In contrast to the micrograph in Figure 23 - (A), which illustrates the surface of a graphite electrode without any polymeric modification, a relatively smooth surface is observed, composed of lamellar structures characteristic of graphite.

4.1.1.3 TEM Analysis

The morphology of the electropolymerized poly(brilliant cresyl blue) film on the graphite electrode was investigated by high-resolution transmission electron microscopy (HR-TEM), as shown in Figure 24. The micrograph reveals a complex and heterogeneous structure with distinct morphological regions at the interface between the substrate and the polymeric film. In the lower portion of the image, the characteristic lamellar structure of the graphite substrate is observed, identified by the darker region and the regular organization of graphene planes. Over this surface, the polymeric film exhibits a morphology with a crystallinity gradient. The upper region of the film, more distant from the substrate, presents an ordered arrangement with prominent transverse lattice fringes, indicating the formation of well-defined crystalline domains. This organization suggests polymeric growth with a significant degree of structural ordering at the external surface of the film. In contrast, the central region, located at the interface between the graphite substrate and the upper crystalline layer, exhibits a predominantly amorphous morphology. However, immersed in this disordered matrix, multiple crystallization nuclei are visible. These nuclei represent the initial stages of crystalline domain formation, from which the ordered growth of the polymer propagates. The coexistence of amorphous and crystalline phases, together with the presence of nucleation sites, indicates a complex growth mechanism, where the graphite substrate structure may act as a nucleating agent, inducing partial ordering in the adjacent polymeric film, which evolves to a more crystalline structure as the film thickens.

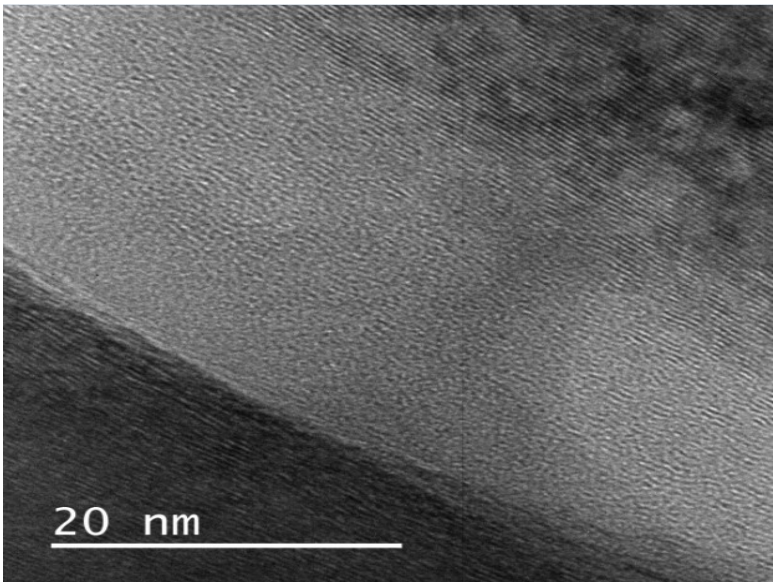


Figure 24 – Micrograph TEM PBCB.

4.1.1.4 FTIR analysis

Figure 25 (A) shows the FTIR spectra of the BCB monomer and the PBCB polymer, highlighting the structural changes resulting from the electropolymerization process. The electropolymerization of the BCB monomer occurs through the initial electrochemical oxidation of the monomeric species, forming radical cations that undergo intermolecular coupling via amino groups, resulting in the formation of conjugated polymer chains [68]. In the BCB spectrum, characteristic bands are observed that are assigned to the stretching of the hydroxyl group (-OH) at approximately 3505 and 3315 cm^{-1}, as well as bands associated with C–H and N–H stretching around 3130 cm^{-1} and with aliphatic C–H stretching at approximately 2973 cm^{-1} [93][94]. In the fingerprint region, the bands corresponding to carbonyl (C=O) stretching at 1654 cm^{-1}, amino group (NH_2) deformation at 1590 cm^{-1}, C–H deformation vibrations at 1442 cm^{-1}, C–O stretching at 1378 cm^{-1}, and characteristic C–O–C bond vibrations distributed between 1544 and 820 cm^{-1} stand out, all of which are attributed to the aromatic structures of the dye [95]. After the electropolymerization process, broadening of the band around 3220 cm^{-1} is observed, as well as the reduction or disappearance of the bands associated with NH_2 and C=O groups, indicating the participation of these groups in the formation of the polymer chain and the establishment of intermolecular interactions, such as hydrogen bonding [96]. Additionally,

the persistence of the bands related to C–H and C–O vibrations in a modified chemical environment suggests the formation of a conjugated polymeric structure [97].

The structural characterization of the BP monomer and the PBP polymer, Figure 25 (B), was also carried out by FTIR, with the aim of identifying the main chemical modifications resulting from the formation of the polymeric film on the electrode surface. In the BP spectrum, a broad band is initially observed in the region of 3400 cm^{-1}, attributed to the stretching vibrations of the hydroxyl group (-OH) present in the phenolic structure of the dye [21]. After the polymerization process, a significant decrease in the intensity of this band is noted in the PBP spectrum, suggesting the involvement of these hydroxyl groups in the electrochemical oxidation mechanism and in the formation of the film. Bands located in the region between 1500 and 1600 cm^{-1} are assigned to the stretching vibrations of the C=C bonds of the aromatic ring. In the PBP spectrum, a slight shift of these bands toward lower wavenumbers is observed, which may be associated with the electronic delocalization promoted by the formation of an extended conjugated system along the polymer chain. This spectral shift indicates an increase in π conjugation in the polymer.

A comparative analysis of the two spectra provides clear evidence of the successful formation of the polymer while preserving the fundamental structural features of the BP molecule. The characteristic C–Br stretching vibrations observed at approximately 747 and 861 cm^{-1} are preserved in the polymer spectrum, confirming that the brominated aromatic structure remains intact after electropolymerization. This structural conservation is essential to maintain the intrinsic electrochemical properties of the dye within the polymer network. For the TB electropolymerized electrode, FTIR analysis was also carried out. TB belongs to the sulfonephthalein class and exhibits a molecular architecture rich in aromatic rings and oxygenated and sulfonic functional groups, whose vibrations are identifiable. The bands located at 3053 and 2939 cm^{-1} in the TB spectrum correspond to the C–H stretching of aromatic and aliphatic carbons originating from the methyl and isopropyl substituents in the structure. The band at 1583 cm^{-1} is attributed to C=C stretching vibrations of the benzene ring, whereas the region between 1460 and 1228 cm^{-1} reveals the complexity of the system, with overlapping phenolic stretching and asymmetric vibrations of the sulfone (S=O) group [98]. The peaks at 1139 and 1013 cm^{-1} correspond to the symmetric stretching of the S=O group, and the band at 895 cm^{-1} is associated with out-of-plane deformation characteristic of substituted aromatic rings. Upon forma-

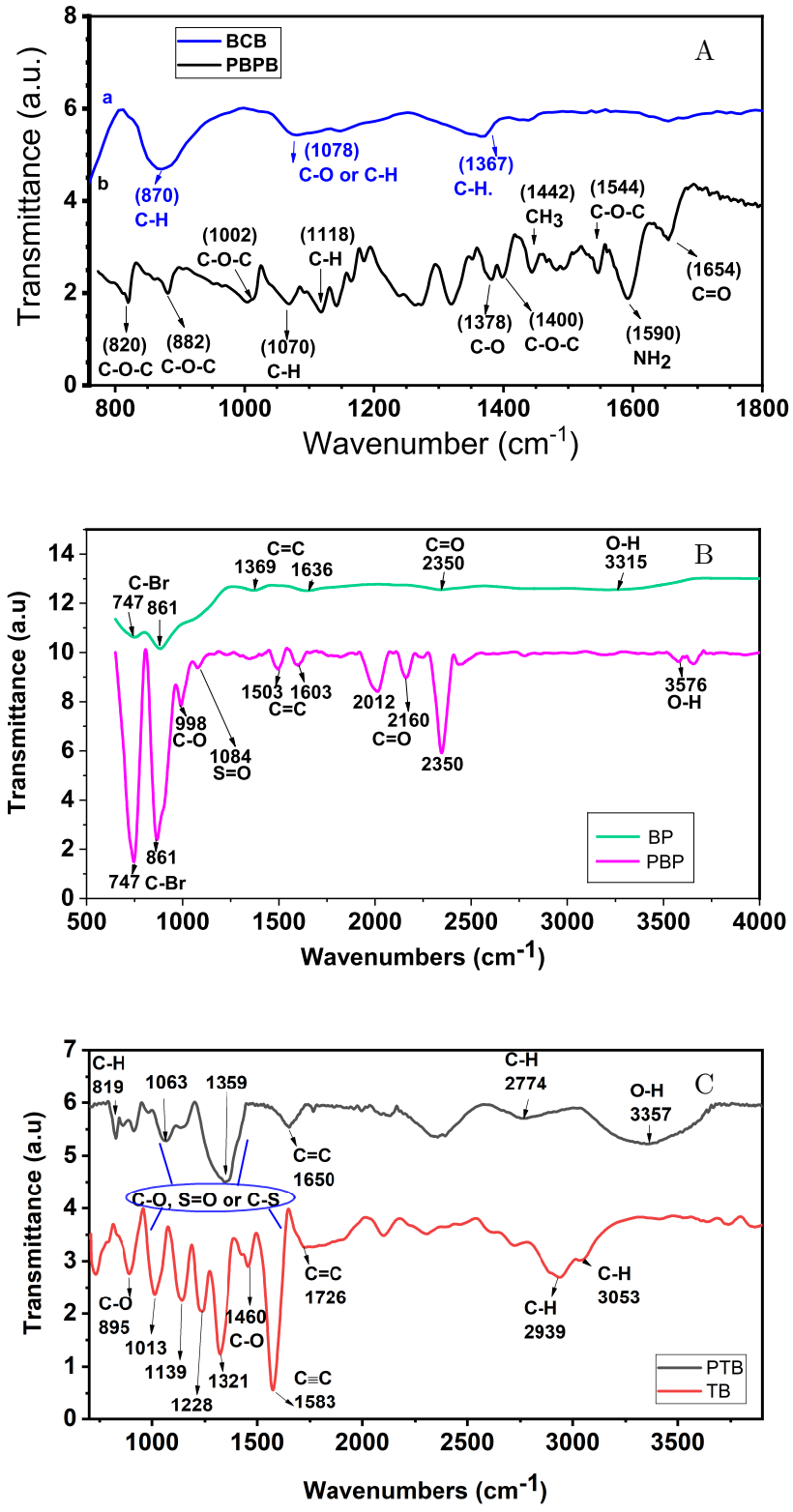


Figure 25 – FTIR: (A) PBCB and BCB; (B) PBP and BP and (C) PTB and TB.

tion of PTB, significant spectral changes are observed that corroborate the occurrence of polymerization and the formation of a macromolecular network. Noteworthy is the emergence of a broad, intense band centered at 3357 cm^{-1}, associated with O–H stretching, which suggests that the hydroxyl groups of the polymer are involved in a complex network of intermolecular hydrogen bonds. The C=C stretching band is shifted to 1650 cm^{-1}, indicative of an increase in the electronic conjugation of the π system after coupling of the monomeric units. The most significant change occurs in the region around 1350 cm^{-1}, where the multiplicity of sharp peaks of the monomer is replaced by a broad, consolidated band that encompasses C–O, S–O and possibly C–S vibrations. This phenomenon is typical of the loss of vibrational resolution in polymeric materials due to increased chain rigidity and the overlap of energetic modes arising from polymer chain extension [99]. The broadening of the bands in the 1000–1400 cm^{-1} region and the persistence of the band at 819 cm^{-1} (C–H) with lower intensity are indicative of polymer formation.

4.1.2 Electrochemical Characterizations of the Electrodes

In the electrodes electropolymerized with BCB, BP, and TB, polymerization was carried out using the cyclic voltammetry technique with 30 cycles, a scan rate of 50 mV/s, and a potential range from −0.6 V to 1.0 V [100]. The electrodes were stored at 4 °C for 24 h before use, following the method employed in the literature [101] and [102].

4.1.2.1 PBCB electrode study

Figures 26 (A) and (B) show the result of the electrochemical deposition of BCB, and Figure 26 (B) displays all thirty cycles performed for the electrodeposition. The current peak generated by the polymer can be observed at 162.57 mA and 0.07 V [103]. In the first scan cycle, an oxidation peak of the monomer is observed, as shown in Figure 26 (A). This peak decreases as the number of cycles increases, and a peak corresponding to the growth of the polymer appears, which can be seen in the curve of the second scan cycle, marking the beginning of polymer growth.

However, the increase in current intensity could no longer be observed as the elec-

tropolymerization process progressed, indicating a limit to the number of applied potential cycles. This occurs due to the increase in the number of cycles, which leads to an increase in the film thickness and, consequently, in the resistivity of the polymeric films. This affects electron transfer, reducing the electrochemical activity of the material.

Figure 26 (C) shows the results of the PBCB scan rate. The scan rate refers to the speed at which a measuring device performs readings or samplings; in other words, it is the rate at which the device updates the data. For the PBCB electrode, a scan was carried out from 5 mV/s to 1000 mV/s in a 50 mL electrolytic cell with PBS at pH 7.

This study was carried out to determine whether the electrochemical process of PBCB deposition occurs via diffusion or adsorption. For this analysis, it is necessary to construct a standard curve, a calibration curve, or an analytical curve that compares the peak current with different concentrations of the analyte or, in this case, different scan rates. Two calibration plots were constructed: one with peak current (Ip) vs. scan rate, shown in Figure 26 (D), which, if it exhibits linear behavior, will indicate that the polymer is immobilized on the electrode surface; that is, the process is adsorption. Meanwhile, linear behavior for the Ip vs. square root of the scan rate plot in Figure 26 (E) would indicate a diffusion-controlled process [104] [105]. The straight lines shown in Figure 26 (D) have a coefficient of determination $R^2 = 0.99$, indicating the quality of the fit to a linear model. The closer this value is to 1, the better the line fits the applied model (the data points lie on or very close to the line).

Figures 26 (F) and (G) show the results of the study of pH in the deposition of BCB, with pH values ranging from 2 to 10. Figure 26 (G) is also presented. This study was carried out using an electrolytic cell with PBS at pH 7. To modify the pH, a 1 M NaOH solution was used, increasing the hydrogen potential up to 10, which was verified with a pH meter. To reduce the pH value, a 1 M H_2SO_4 solution was used.

The cyclic voltammograms obtained can be seen in more detail in Figure 26 (F), which compares pH 2, pH 7, and pH 10. The best pH condition was chosen as the one that provided the highest peak current intensity, which in this work was pH 7. In addition to this practical study, some research describes the electropolymerization of dyes in neutral solutions [17]. The potential window used was from -0.4 V to 0.6 V with a scan rate of 50 mV/s.

Differential pulse voltammetry was also performed for the electrode modified with BCB, which showed a very clear current peak at -0.05 V with a current of 0.061 mA, as

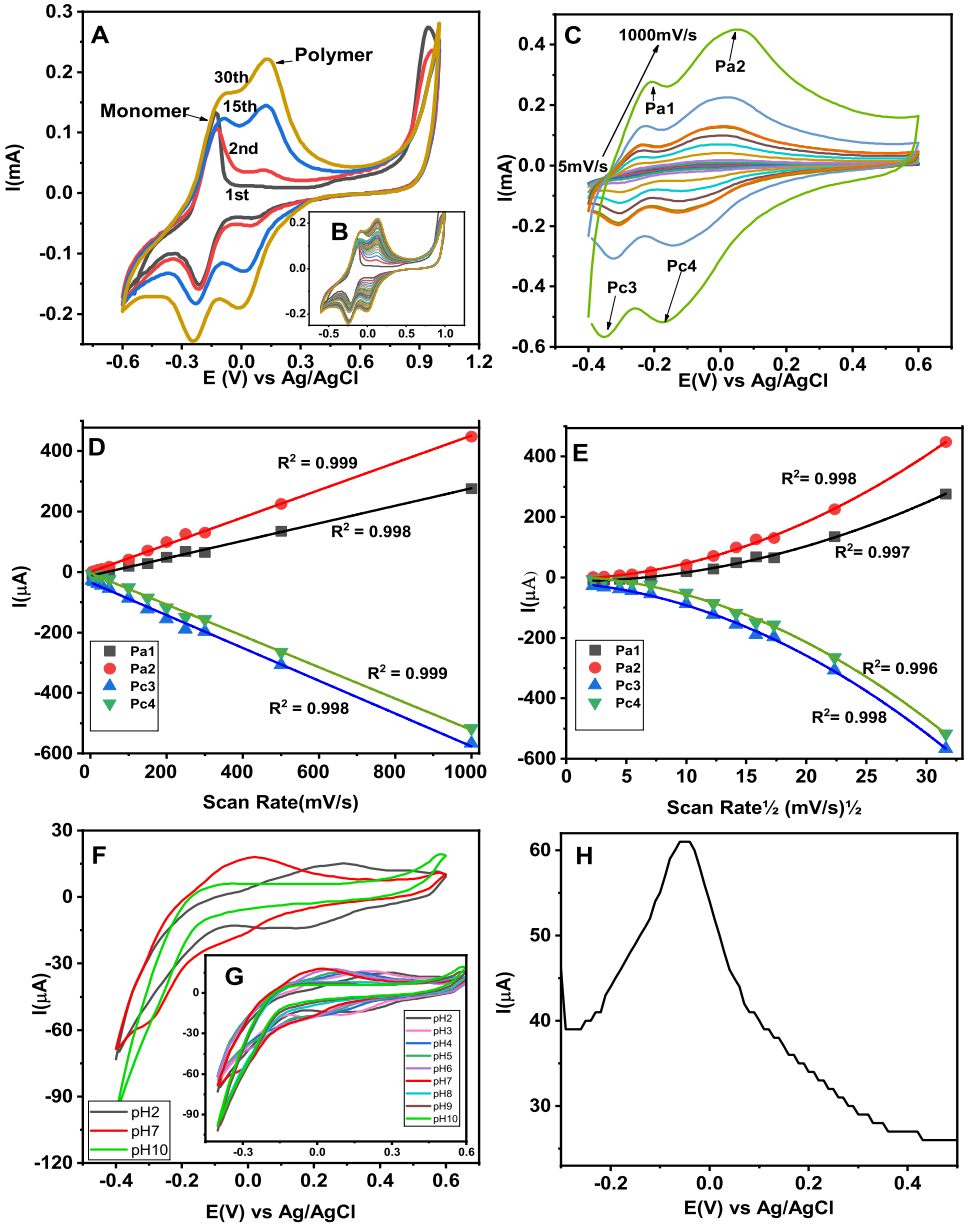


Figure 26 – Electrochemical study of BCB deposition: (A) Cyclic voltammetry of the cycle showing the current peak for the monomer and polymer; (B) All electropolymerization cycles; (C) Scan Rate: Cyclic voltammetry performed with different scan rates (5mV/s to 1000mV/s); (D) Calibration curve Ip *vs* Scan Rate; (E) Calibration curve Ip *vs* the square root of the Scan Rate; (F) Study of the polymer behavior with PBS at pH 2, pH 7 and pH 10; (G) Study from pH 2 to pH 10; (H) DPV of the polymerized electrode.

can be seen in Figure 26 (H), indicating the deposition of the dye. The potential window used ranged from -0.3 V to 0.7 V, with a scan rate of 20 mV/s.

4.1.2.2 PBP electrode study

Figure 27 (A) shows the result of the electrochemical deposition of BP; the current peak generated by the polymer can be observed at 30 μA and 0.2 V. In the first scan cycle, an oxidation peak of the monomer can be observed, as indicated in Figure 27 (A); this peak decreases as the number of cycles increases, and a peak corresponding to the growth of the polymer appears, which can be seen in the curve of the last scan cycle. The electrode polymerized with BP also shows saturation at around thirty cycles, with no increase in peak current, a behavior that is also observed for the electrode with BCB deposition.

Figure 27 (B) shows the scan rate results for PBP. Scans were performed from 5 mV/s to 1500 mV/s in a 50 mL electrolytic cell with PBS at pH 7. The analysis focused on scan rates from 5 mV/s to 500 mV/s.

This study was carried out to verify whether the electrochemical process of PBP deposition occurs via diffusion, adsorption, or a mixed process. For this analysis, it is necessary to construct a standard curve. Two calibration curve plots were constructed: one with the peak currents Peak current (Ip) vs. the scan rate, shown in Figure 27 (D), which presented a coefficient of determination $R^2 = 0.98$. This correlation was close to 1, but the analysis of the calibration plot using the logarithm showed a coefficient of determination even closer to 1. Based on this analysis, the other graph plotted from the Scan Rate analysis data was log anodic peak current (Ipa) vs. log Scan Rate, Figure 27 (E).

The analysis of the dependence of the anodic peak current (Ipa) on the scan rate revealed a linear relationship between log Ipa and log scan rate, indicating that the electrochemical process follows a well-defined power law. The slope value obtained from the linear fit provides direct information about the reaction control mechanism. For electropolymerized graphite electrodes, slopes close to unity or intermediate between 0.5 and 1.0 are typical of processes predominantly controlled by redox species confined to the

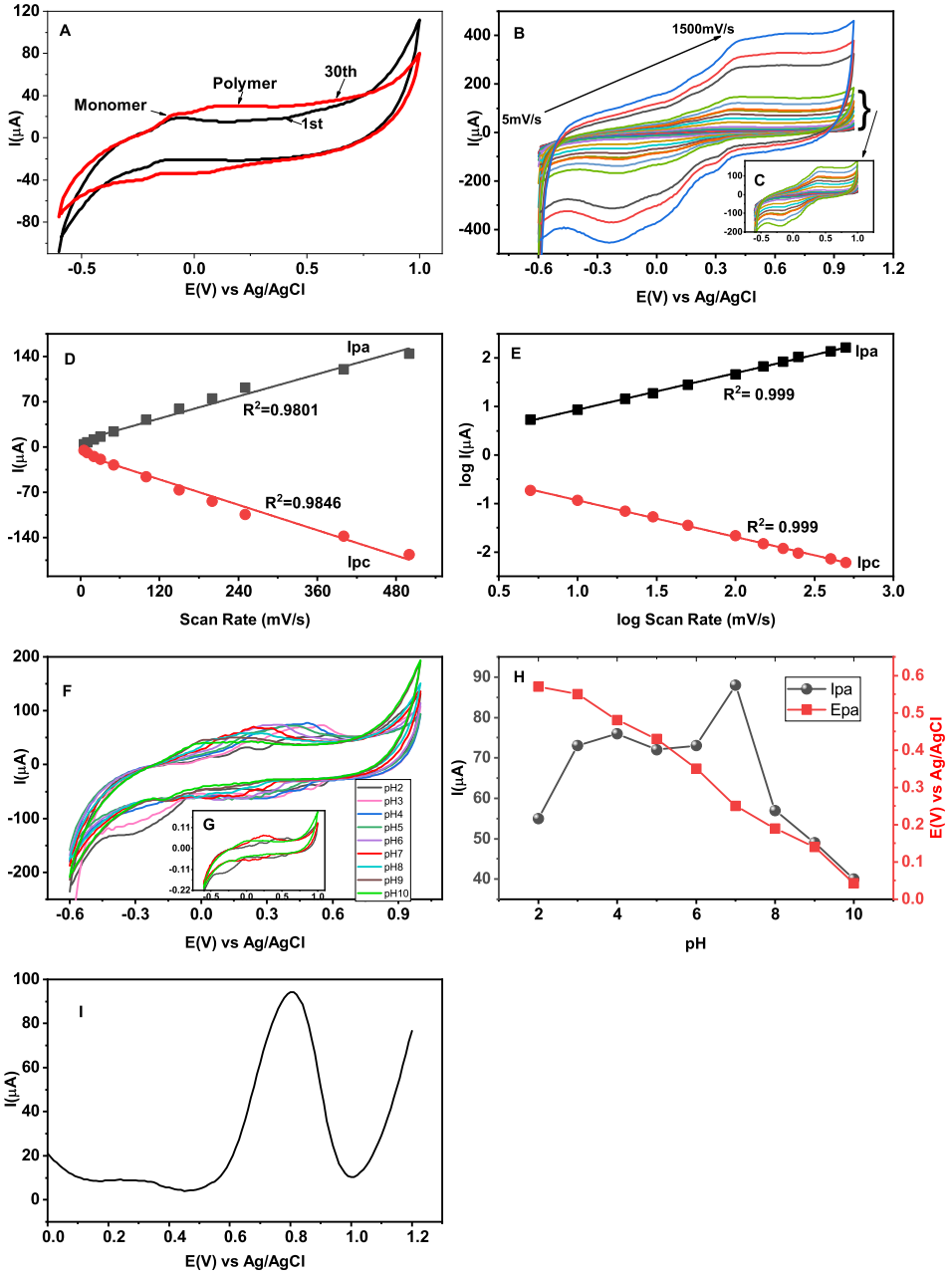


Figure 27 – Electrochemical study of BP deposition: (A) Cyclic voltammetry of the cycle showing the current peak referring to the monomer and the polymer; (B) Cyclic voltammetry with all cycles; (C) Scan Rate: Cyclic voltammetry performed with different scan rates (5mV/s to 1000mV/s); (D) Calibration curve Ip *vs* Scan Rate; (E) Calibration curve log Ip *vs* log Scan Rate; (F) Study of pH 2, pH 7 and pH 10; (G) Study of the polymer behavior with PBS from pH 2 to pH 10; (H) DPV of the polymerized electrode.

surface or within the polymer film, with a diffusional contribution associated with ion transport through the polymer matrix [106]. In this test, the slope of the line was 0.7. This behavior shows that the electropolymerized film is electroactive, adheres well to the graphite substrate, and promotes electronic transport along the polymer chain.

Figures 27 (F) and (G) show the results of the pH study in the deposition of BP, with pH values ranging from 2 to 10, as presented in Figure 27 (F). This study was carried out using the electrolytic cell with PBS at pH 7. To modify the pH, the same procedure described for the BCB electrode was used.

The cyclic voltammograms obtained can be observed in more detail in Figure 27 (G), which compares pH 2, pH 7, and pH 10. The best pH condition was chosen as the one that provided the highest peak current intensity, which in this work was pH 7. Figure 27 (H) shows an analysis between the observed peak current and the potential of this peak current, and this presentation facilitates the visualization of the optimal pH for the test.

Differential pulse voltammetry was also carried out for the BP-modified electrode, which showed a very pronounced current peak at 0.81 V with a current of 94.17 μA, as can be seen in Figure 27 (I), indicating the deposition of the dye.

4.1.2.3 PTB electrode study

Figure 28 presents the detailed electrochemical study of the deposition and behavior of electropolymerized TB on the graphite electrode.

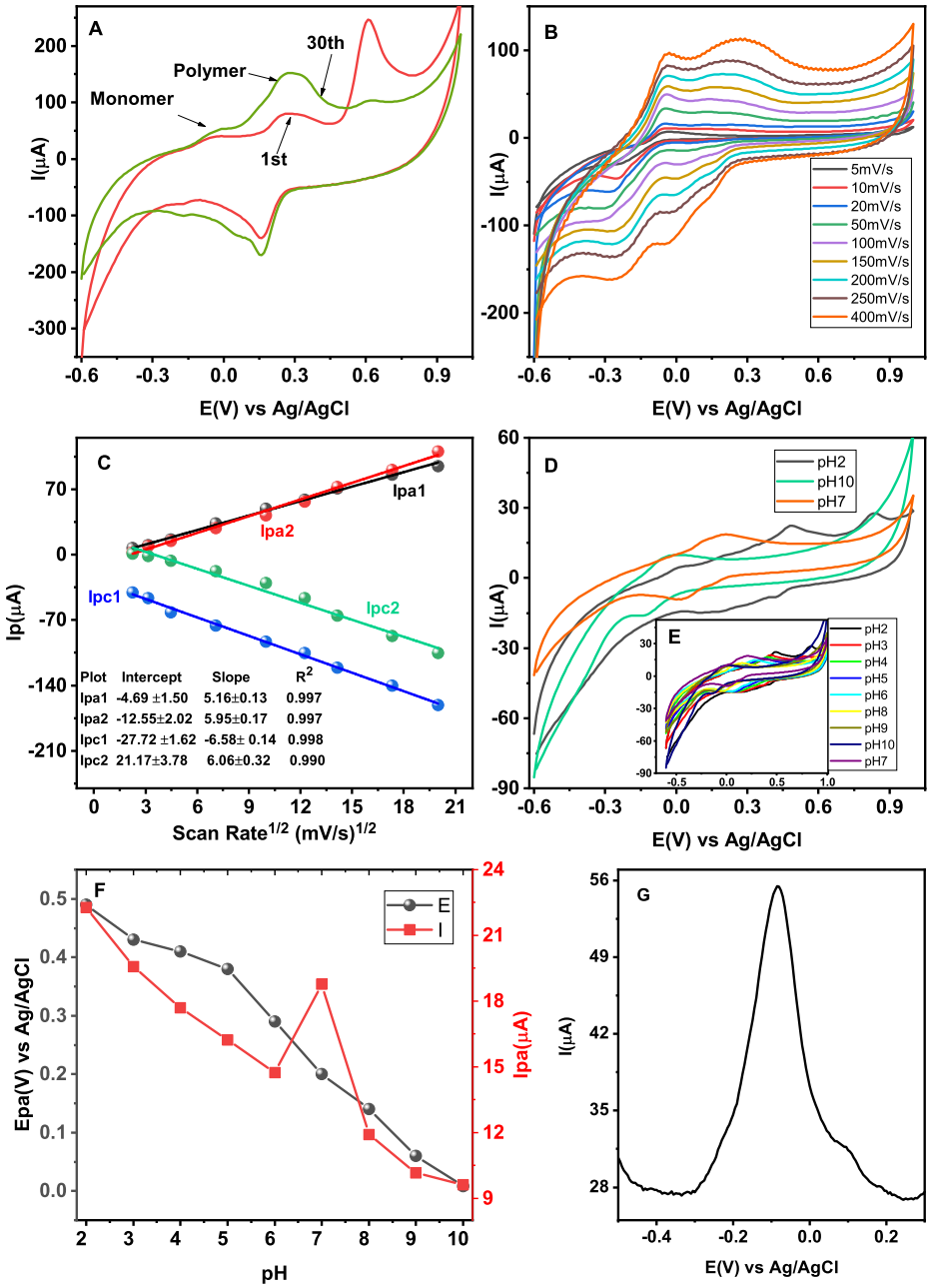


Figure 28 – Electrochemical study of TB deposition: (A) Cyclic voltammetry of the cycle showing the peak current related to the monomer and the polymer; (B) Scan Rate: Cyclic voltammetry performed with different scan rates (5mV/s to 400mV/s); (C) Calibration curve Ip *vs* square root of the Scan Rate; (D) Study of the polymer behavior with PBS at pH 2, pH 7 and pH 10; (E) Study from pH 2 to pH 10; (F) Analysis of pH behavior in relation to peak current and potential; (G) DPV of the polymerized electrode.

The cyclic voltammetry recorded, Figure 28 (A), over the course of 30 cycles reveals the process of formation of the polymeric film. In the first cycle, an oxidation peak associated with the TB monomer is observed, and the curve also shows the appearance of the PTB polymer at 0.3 V.

With the progression of the cycles, there is a progressive increase in the current and a modification of the voltammetric profile, characterizing the formation of the polymer on the graphite electrode. The cyclic voltammograms recorded at different scan rates (5 to 400 mV/s), shown in Figure 28 (B), exhibit a systematic increase in peak currents with increasing scan rate. The preservation of the voltammogram shape indicates the stability of the polymer film. To complement the study of the scan rates, the calibration curve shown in Figure 28 (C) was obtained, which displays a linear relationship between the peak current (Ip) and the square root of the scan rate, indicating a relevant diffusional contribution to the electrochemical process. The voltammograms recorded in PBS with different pH values are shown in Figures 28 (D) and (E), where Figure (E) presents pH values from 2 to 10 and Figure 28 (D) shows a comparison of the analyzed limits (pH 2 and pH 10) with pH 7. This analysis shows variations in both current and peak potential. The increase in pH causes a shift of the oxidation potential to less positive values. The pH analysis together with the quantitative analysis of the data, Figure 28 (F), indicated an ideal working potential (pH 7). The DPV profile, Figure 28 (G), shows a well-defined and narrow peak, demonstrating high sensitivity.

4.2- Analyte results

The Figures from 29 to 60 present the results of the analyses carried out with the electropolymerized electrodes and the respective detected analytes. In the CV, DPV, and LSV graphs, the curves were shown:

- Modified electrode analyzing PBS with no analyte identified as Modified Electrode (Mod) 0μM,
- Modified electrode analyzing analyte identified as Mod (concentration)μM,
- Unmodified electrode (pure graphite) analyzing PBS with no analyte identified as Bare 0μM,
- Unmodified electrode (pure graphite) analyzing PBS with analyte identified as Bare

(Concentration) μM.

The CV, DPV, and LSV tests for all analytes present a comparison between the modified electrodes (Mod) and the bare electrode (Bare), where it can be observed that the modified electrode exhibited a higher detection peak current than the unmodified electrode. This behavior indicates that the electropolymeric modification promotes an electrocatalytic effect, favoring charge transfer and enhancing the electroanalytical response.

For the LSV test, a summary plot was prepared showing the detection points in a concise way to allow better comparison between the bare electrodes (Bare) and the modified electrode (Mod).

For better understanding, tables were prepared compiling the test results. Table 6 presents the compiled results of the analytes detected by the PBCB electrode. Table 8 presents the compiled results of the analytes detected by the PBP electrode, and Table 10 presents the results of the analytes detected by the PTB electrode..

The CV graphs show the concentration curves of the analytes tested and display a well-defined detection peak. In Tables 6, 8 and 10, in the row CV - Ep (V), the peak detection potential values for each analyte are presented.

The DPV and LSV graphs also show the concentration curves of the analytes tested and display detection peaks; some analytes showed less well-defined peaks compared with the CV test. In Tables 6, 8, and 10, in the rows DPV - Ep (V) and LSV - Ep, the peak detection potential values for each analyte are presented. Comparing the detection peaks from the CV, DPV, and LSV tests, it is observed that the detection potential values remain around the same value for each analyte. The agreement of the peak potentials obtained by the CV, DPV, and LSV techniques indicates that the observed redox process is characteristic of the analyte and independent of the voltammetric method employed. The maintenance of similar detection potential values demonstrates the electrochemical stability of the system, the absence of significant experimental effects, and good reliability in the identification of the analyte. This behavior reinforces that the electrode modification promotes signal amplification without altering the fundamental electrochemical mechanism of the species analyzed.

A large part of the plots related to the calibration curve (linear regression) shows linear behavior with $R^2 \approx 0.99$, indicating that the peak detection current increases linearly with increasing analyte concentration. The limits of detection (LD) and quantification (LQ) were calculated from the calibration curves of the respective tests and are presented

in Tables 6, 8, and 10 in the rows CV - LD, CV - LQ, DPV - LD, DPV - LQ, CA - LD, CA - LQ.

The storage stability of the electrode was evaluated by comparing the peak current obtained immediately after sensor preparation with the currents measured after different storage periods. The electrodes were stored under controlled conditions (4 °C) and analyzed every seven days for two months. Stability was expressed as the percentage of electrochemical signal retention, calculated as the ratio between the peak current measured at a given storage time and the initial current of the freshly prepared electrode. High signal retention values indicate that the polymer film remains stable and adhered to the electrode surface, preserving its electrocatalytic activity over time.

The Figures 30, 32, 34, 36, 38, 41, 43, 45, 47, 49, 52, 54, 56, 58 e 60 (A) and (B) show the analyses of analyte detection using the CV test at different pH values, ranging from 2 to 10. The pH study was carried out with the aim of identifying the experimental condition that would provide the best electrochemical response of the system. The optimal response was considered to be that corresponding to the pH which showed the highest peak current associated with the lowest detection potential, indicating greater electrocatalytic efficiency and better analytical performance of the modified electrode. For all analytes, the best response was obtained at pH 7. The analytical efficiency of electrodes modified with Poly(Cresyl Brilliant Blue) (PBCB), Poly(Bromophenol Blue) (PBPB), and Poly(Thymol Blue) (PTB) films is intrinsically dependent on the pH of the electrolyte medium, since most of the oxidation and reduction processes of these systems involve proton-coupled electron transfer (PCET).

4.2.1 Electroanalytical results of analytes identified by the PBCB electrode

Table 6 presents a compilation of the results shown in Figures 29, 31, 33, 35, and 37, in addition to presenting the values of LD, LQ, and Sensitivity of the tests CV, DPV, and CA. Guanine, adenine, and thymine used a potential window from 0.4 V to 1.4 V for the CV, DPV, and LSV tests, while for AU a window from 0.0 V to 1.0 V was required, and for AA the potential window was from -0.2 V to 0.6 V for the same voltammetric tests.

The response time presented by the PBCB electrode was between 8 and 23 s, as shown in Table 6, row CA - Time.

Table 6 presents the main electroanalytical parameters obtained for the detection of G, A, T, AU, and AA using different voltammetric techniques, including CV, DPV, LSV, and CA. These results make it possible to evaluate the performance of the modified electrode in terms of linear detection range, sensitivity, limit of detection (LD), limit of quantification (LQ), and correlation coefficient (R^2), which are fundamental parameters for the validation of electroanalytical methods.

In cyclic voltammetry (CV), the analytes showed linear responses over different concentration ranges. For guanine, the linear range was from 4 to 160 µM, with a correlation coefficient $R^2 = 0.989$, indicating good linearity of the electrochemical response. For adenine, a linear range between 7 and 217 µM was observed, with $R^2 = 0.995$, whereas for thymine the detection range was significantly broader, from 10 to 375.35 µM, with $R^2 = 0.994$. In the case of uric acid, the linear range was between 7.9 and 101.42 µM ($R^2 = 0.995$), and for ascorbic acid a range from 9.99 to 1258.74 µM was obtained, with $R^2 = 0.997$, indicating excellent linearity. The limits of detection calculated by the CV technique were 3.816 µM (guanine), 6.809 µM (adenine), 0.251 µM (thymine), 0.204 µM (uric acid), and 0.168 µM (ascorbic acid), demonstrating high sensitivity of the electrochemical system for some of these analytes.

Using differential pulse voltammetry (DPV), the linear concentration ranges were 25 – 424.21 µM for guanine, 49.75 – 267.63 µM for adenine, 583.3 – 1680.5 µM for thymine, 65 – 101.68 µM for uric acid, and 38.84 – 566.03 µM for ascorbic acid. The correlation coefficients obtained were high (R^2 between 0.993 and 0.998), indicating excellent linear fitting between current and concentration. The limits of detection obtained by DPV were 24.416 µM for guanine, 14.772 µM for adenine, 40.246 µM for thymine, 62.117 µM for uric acid, and 18.029 µM for ascorbic acid, while the sensitivity values ranged from 0.028 to 0.142 µA μM^{-1}, depending on the analyte.

An important point of discussion lies in the comparison between cyclic voltammetry (CV) and differential pulse voltammetry (DPV). Although DPV is traditionally recognized for its higher sensitivity due to the discrimination of the capacitive current, the experimental results of this work revealed significantly lower detection limits in CV for analytes such as ascorbic acid (LD – CV = 0.168 μM vs. LD – DPV = 18.029 μM) and uric acid (LD – CV = 0.204 μM vs. LD – DPV = 62.117 μM). This apparently anomalous behavior suggests that the oxidation process at the PBCB electrode is not purely diffusion-controlled, but exhibits a strong adsorption component. In adsorption-controlled processes,

the peak current is proportional to the scan rate (v), whereas in diffusional processes it is proportional to the square root of the scan rate ($v^{1/2}$). By performing continuous scans, CV can favor an in situ preconcentration of the analyte on the polymer surface, resulting in more intense signals at low concentrations compared with the DPV pulses, which may not allow the same degree of surface interaction.

In cyclic voltammetry, the obtained linear ranges were robust, highlighting ascorbic acid (9.99 to 1258.74 μM; $R^2 = 0.997$) and thymine (10 to 375.35 μM; $R^2 = 0.994$).

Linear sweep voltammetry (LSV) also showed linear responses for different concentration ranges, notably 47.7 – 196 µM for adenine, 375.36 µM for thymine, 19.9 – 291.26 µM for uric acid, and 384.61 – 1258.74 µM for ascorbic acid, with characteristic oxidation potentials for each species analyzed. These results confirm the ability of the modified electrode to promote distinct electrocatalytic processes for different compounds.

Using the chronoamperometry (CA) technique, calibration curves with high linearity (R^2 between 0.976 and 0.996) were obtained. The calculated detection limits were 10.087 µM for guanine and 5.757 µM for adenine. 7.398 µM for thymine, 15.772 µM for uric acid, and 3.220 µM for ascorbic acid, while the sensitivity values varied between 0.760 and 1.488 µA μM^1, demonstrating a good amperometric response of the sensor.

Table 7 summarizes the analytical validation parameters obtained for the analytes guanine, adenine, thymine, uric acid, and ascorbic acid, including the studies of repeatability, reproducibility, and stability, evaluated before and after applying the statistical tests for outlier detection (Dixon's Q test and Grubbs' test). These tests were applied in order to identify possible experimental outliers and improve the statistical reliability of the results.

In the repeatability study, the initial RSD values (initial Repet RSD) ranged from 9.451% to 16.587%, indicating differences in the degree of dispersion among the measurements obtained for each analyte. After applying the statistical tests and removing outliers, a significant reduction in the final RSD (end Repet RSD) was observed for most analytes. For guanine, the RSD decreased from 16.587% to 4.618%, indicating a strong influence of an outlier on the initial measurements. Similar reductions were observed for thymine (from 9.451% to 6.173%) and adenine (from 7.260% to 3.089%).

For ascorbic acid, the final value was 7.682%, while for uric acid it was 1.674%, indicating high experimental precision for this analyte. These results show that the removal of outlier values contributed to improving precision. The initial RSD values (initial

Table 6 – Compilation of information from tests performed with analytes detected by the PBCB electrode.

Parameters	Guanine	Adenine	Thymine	AU	AA
CV [1]Plot	[5]Fig 29 A	[5]Fig 31 A	[5]Fig 33 A - B	[5]Fig 35 A - B	[5]Fig 37 A - B
CV - Range (μM)	4 - 160	7 - 213.64	10 - 375.35	7.9 - 1010.42	9.99 - 1258.74
CV - [2]Ep (V)	0.7	1.07	1.2	0.4	0.2
CV - [3]Line - [1]Plot	[5]Fig 29 B	[5]Fig 31 B	[5]Fig 33 C	[5]Fig 35 C	[5]Fig 37 C
CV - R^2	0.989	0.995	0.994	0.995	0.997
CV - LD (μM)	3.816	6.809	0.251	0.204	0.168
CV - LQ (μM)	11.566	20.635	0.762	0.620	0.510
CV - [4]Sens ($\mu A \mu M^{-1}$)	0.880	0.300	0.053	0.041	0.033
DPV [1]Plot	[5]Fig 29 C	[5]Fig 31 C	[5]Fig 33 D	[5]Fig 35 D	[5]Fig 37 D
DPV - Range (μM)	25 - 424.21	49.75 - 267.63	583.3 - 1680.5	65 - 1016.88	39.84 - 566.03
DPV - [2]Ep (V)	0.75	1.03	1.2	0.4	0.14
DPV - [3]Line -[1]Plot	[5]Fig 29 D	[5]Fig 31 D	[5]Fig 33 E	[5]Fig 35 E	[5]Fig 37 E
DPV - R^2	0.997	0.993	0.998	0.994	0.997
DPV - LD (μM)	24.416	14.772	40.246	62.117	18.029
DPV - LQ (μM)	73.989	44.763	121.960	188.236	54.634
DPV - [4]Sens ($\mu A \mu M^{-1}$)	0.057	0.055	0.032	0.142	0.028
LSV [1]Plot	[5]Fig 29 E - F	[5]Fig 31 E - F	[5]Fig 33 F - G	[5]Fig 35 G - H	[5]Fig 37 F - G
LSV [6]Concent (μM)	99	47.7 and 196	375.36	19.9 - 291.26	384.61 - 1258.74
LSV - [2]Ep (V)	0.72	1.08	1.2	0.38	0.1
CA - [1]Plot	[5]Fig 29 G	[5]Fig 31 G	[5]Fig 33 H	[5]Fig 35 I	[5]Fig 37 H
CA - Time (s)	21	23	17	8	13
CA - [3]Line - [1]Plot	[5]Fig29 H	[5]Fig 31 H	[5]Fig 33 I	[5]Fig 35 J	[5]Fig 37 I
CA - R^2	0.991	0.996	0.994	0.976	0.992
CA - LD (μM)	10	5.757	7.398	15.772	3.220
CA - LQ (μM)	30.568	17.446	22.418	47.796	9.759
CA - [4]Sens ($\mu A \mu M^{-1}$)	0.760	1.353	1.488	0.994	1.061

[1]Graphic, [2]Peak detection voltage or peak potential, [3]Linear regression or calibration curve, [4]Sensitivity, [5]Figure and [6]Concentration

Reprod RSD) showed greater dispersion for some analytes, such as adenine (21.081%) and thymine (36.845%), suggesting the presence of atypical measurements. After applying the Dixon and Grubbs tests, there was a significant reduction in the final RSD, reaching 5.179% for guanine, 0.989% for adenine, 12.430% for thymine, 1.453% for uric acid, and 9.438% for ascorbic acid. The observed improvement reinforces the importance of the statistical treatment of experimental data.

The stability study was conducted based on the initial retention stability (Stab ret ini), which represents the percentage of the electrode response maintained over time before the application of statistical tests. Satisfactory values were observed for all analytes, with emphasis on adenine (75.810%), thymine (67.180%), uric acid (50.911%), and ascorbic acid (80.459%), indicating good preservation of the electrochemical response. Although retention values above 90% are often reported as ideal for electrochemical electrodes, moderate variations may occur in systems based on electropolymerized films due to factors

Table 7 – Compilation of information from validation tests with analytes detected by the PBCB electrode.

Validation Parameters	Guanine	Adenine	Thymine	AU	AA
[2]Repet [1]Plot	[5]Fig 30 C - D	[5]Fig 32 C - D	[5]Fig 34 C - D	[5]Fig 36 C - D	[5]Fig 38 C - D
[3]RSD [2]Repet initial (ini) (%)	16.587	7.260	9.451	4.930	22.018
[6]Q [2]Repet	0.719 (95%)	0.644(90%)	0.407 (NA)	0.463 (NA)	0.699 (90%)
[7]Gs [2]Repet	1.743 (95%)	1.678(90%)	1.721 (90%)	1.674 (90%)	1.335(NA)
[3]RSD [2]Repet [8]end (%)	4.618	3.089	6.173	-	7.682
[9]Reprod Plot	[5]Fig 30 E - F	[5]Fig 32 E - F	[5]Fig 34 E - F	[5]Fig 36 E - F	[5]Fig 38 E - F
[3]RSD [9]Reprod [4]ini (%)	7.647	21.081	36.485	31.422	12.811
[6]Q [9]Reprod	0.385 ([11]NA)	0.140([11]NA)	0.701 (90%)	0.621 (85%)	0.288 ([11]NA)
[7]Gs [9]Reprod	1.469 (80%)	0.989 ([11]NA)	1.721 (90%)	1.674 (90%)	1335 ([11]NA)
[3]RSD [9]Reprod [8]end (%)	5.179	-	14.350	14.532	9.438
[10]Stab [1]Plot	[5]Fig 30 G - H	[5]Fig 32 G - H	[5]Fig 34 G - H	[5]Fig 36 G - H	[5]Fig 38 G - H
[10]Stab [12]ret [4]ini (%)	57.050	75.819	67.180	50.911	80.459
[3]RSD [10]Stab [4]ini (%)	19.341	8.951	14.844	25.455	7.920
[6]Q [10]Stab	0.543 (95%)	0.690 (99%)	0.619 (95%)	0.540 (95%)	0.295 ([11]NA)
[7]Gs [10]Stab	2.195 (95%)	2.300 (95%)	2.308 (95%)	2.229 ([11]NA)	1.872 (80%)
[10]Stab [12]ret [8]end (%)	74.410	91.008	84.737	69.316	85.386
[3]RSD [10]Stab [8]end (%)	10.267	3.671	6.079	12.998	6.092

[1]Graphic, [2]Repeatability, [3]Relative Standard Deviation, [4]Initial Result, [5]Figure, [6]Q Dixon, [7]G Grubbs, [8]Final Result, [9]Reproducibility, [10]Stability,[11]Not Apply and [12]Retention.

such as surface reorganization of the active material and interactions with the electrolyte matrix. Even so, the values observed indicate that the sensor retains a significant fraction of its electrochemical response over time, demonstrating adequate stability for analytical applications. The RSD values for the initial stability ranged between 7.920% and 25.455%, again reflecting the presence of possible outlier measurements.

After applying the outlier detection tests, the final retention stability (Stab ret end) and the respective final RSDs were obtained, which showed reduced and more consistent values. The final RSDs were 10.267% for guanine, 3.671% for adenine, 6.079% for thymine, 12.998% for uric acid, and 6.092% for ascorbic acid, confirming the improvement in data precision after the statistical treatment.

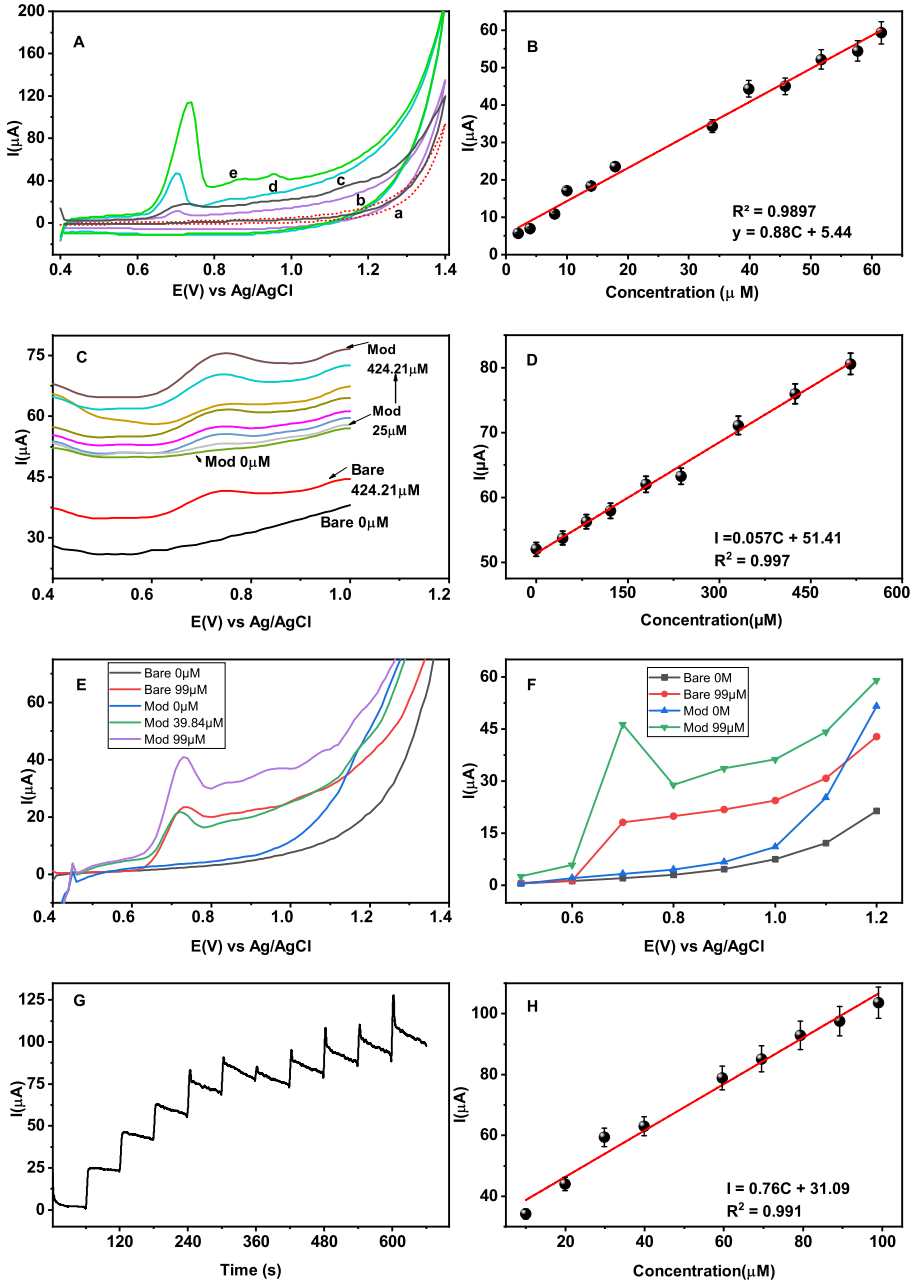


Figure 29 – Guanine Detection: (A) CV: curve (a) Mod 0μM, curve (b) Mod 9.99μM, curve (c) Bare 160μM, curve (d) Mod 81.33μM and curve (e) Mod 160μM; (B) CV test calibration curve; (C) DPV; (D) DPV test calibration curve; (E) LSV; (F) LSV summary; (G) Chronoamperometry; (H) Chronoamperometry test calibration curve.

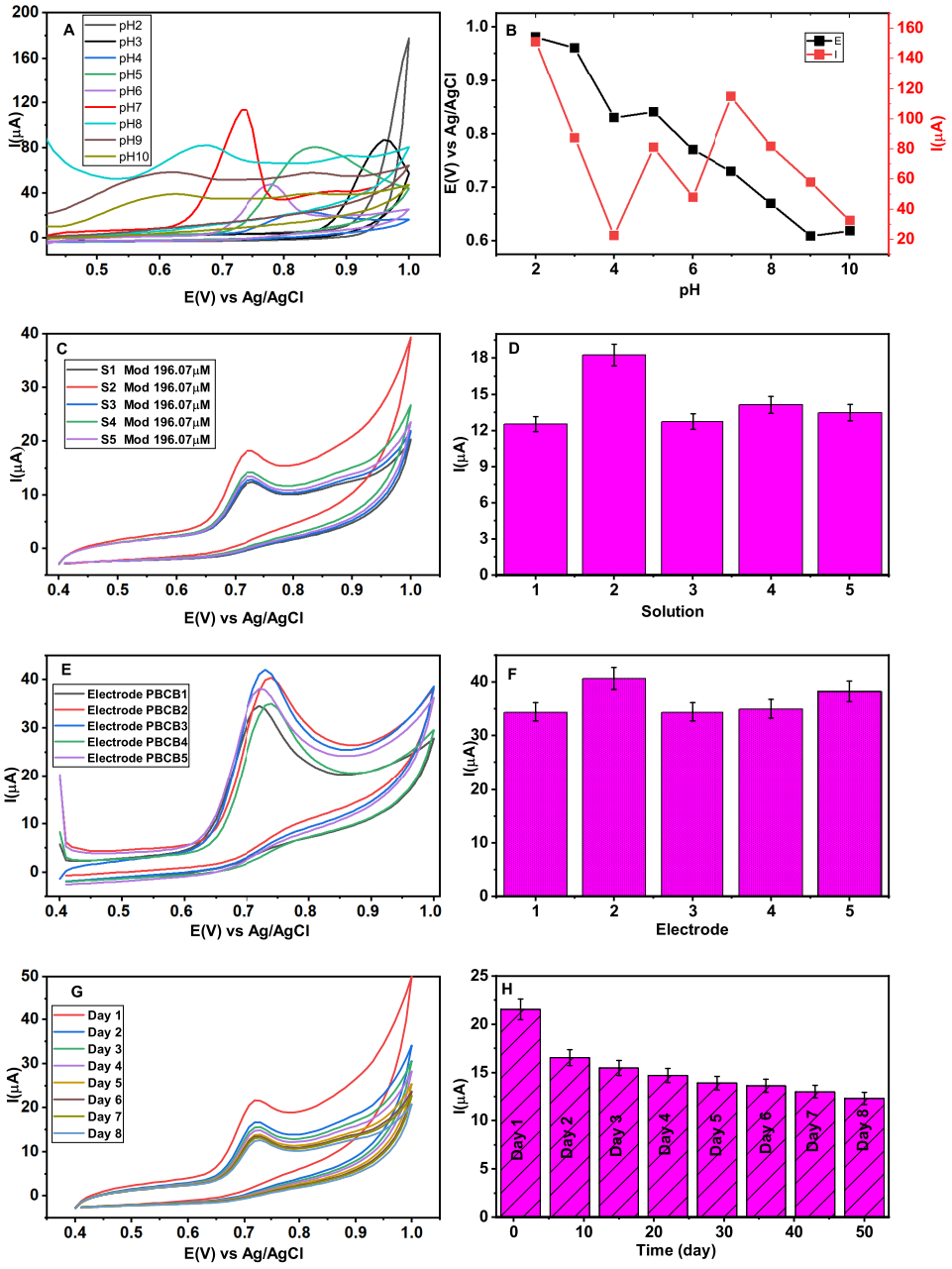


Figure 30 – Guanine Validation: (A) pH; (B) pH Summary; (C) Repeatability; (D) Repeatability Summary; (E) Reproducibility; (F) Reproducibility Summary; (G) Stability; (H) Stability Summary.

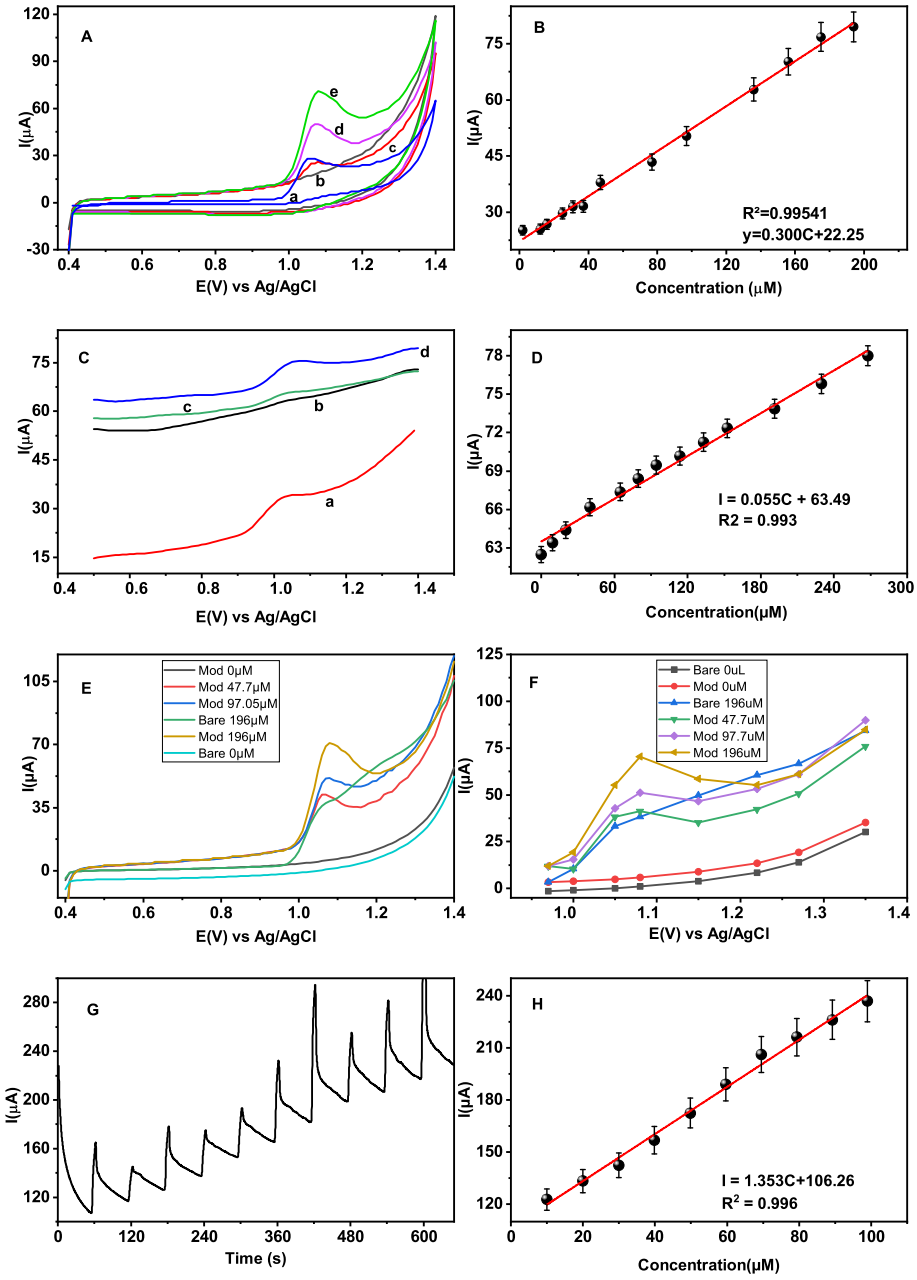


Figure 31 – Adenine Detection: (A) CV: curve (a) refers to Bare 213.34μM, curve (b) Mod 0μM, curve (c) Mod 11.98μM, curve (d) Mod 136.12μM and curve (e) Mod 213.34μM; (B) CV test calibration curve; (C) DPV: curve (a) refers to Bare 267.63μM, curve (b) Mod 0μM, curve (c) Mod 49.75μM and curve (d) Mod 267.63μM; (D) DPV test calibration curve; (E) LSV; (F) LSV summary; (G) Chronoamperometry; (H) Chronoamperometry test calibration curve.

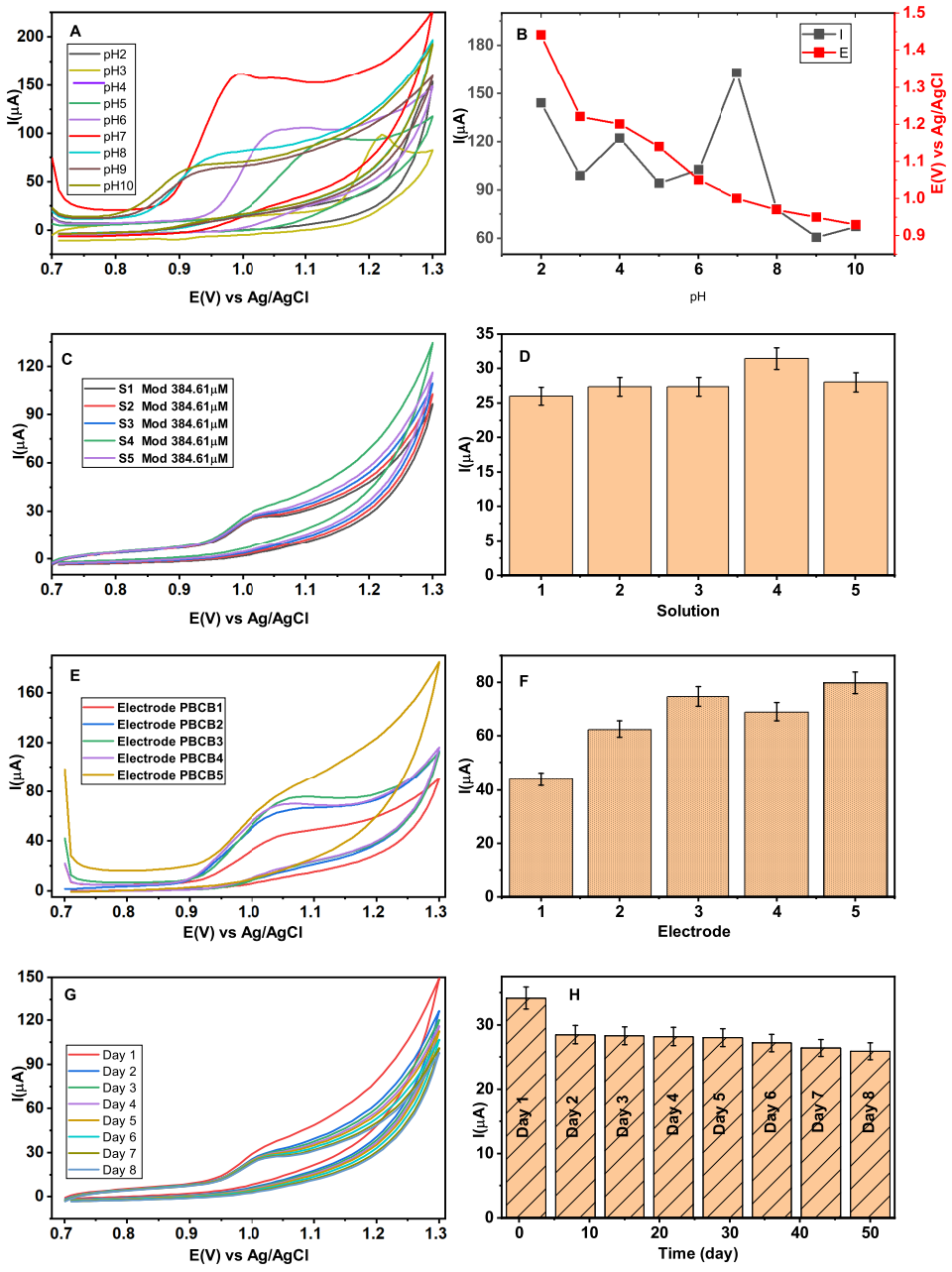


Figure 32 – Adenine Validation: (A) pH; (B) pH Summary; (C) Repeatability; (D) Repeatability Summary; (E) Reproducibility; (F) Reproducibility Summary; (G) Stability; (H) Stability Summary.

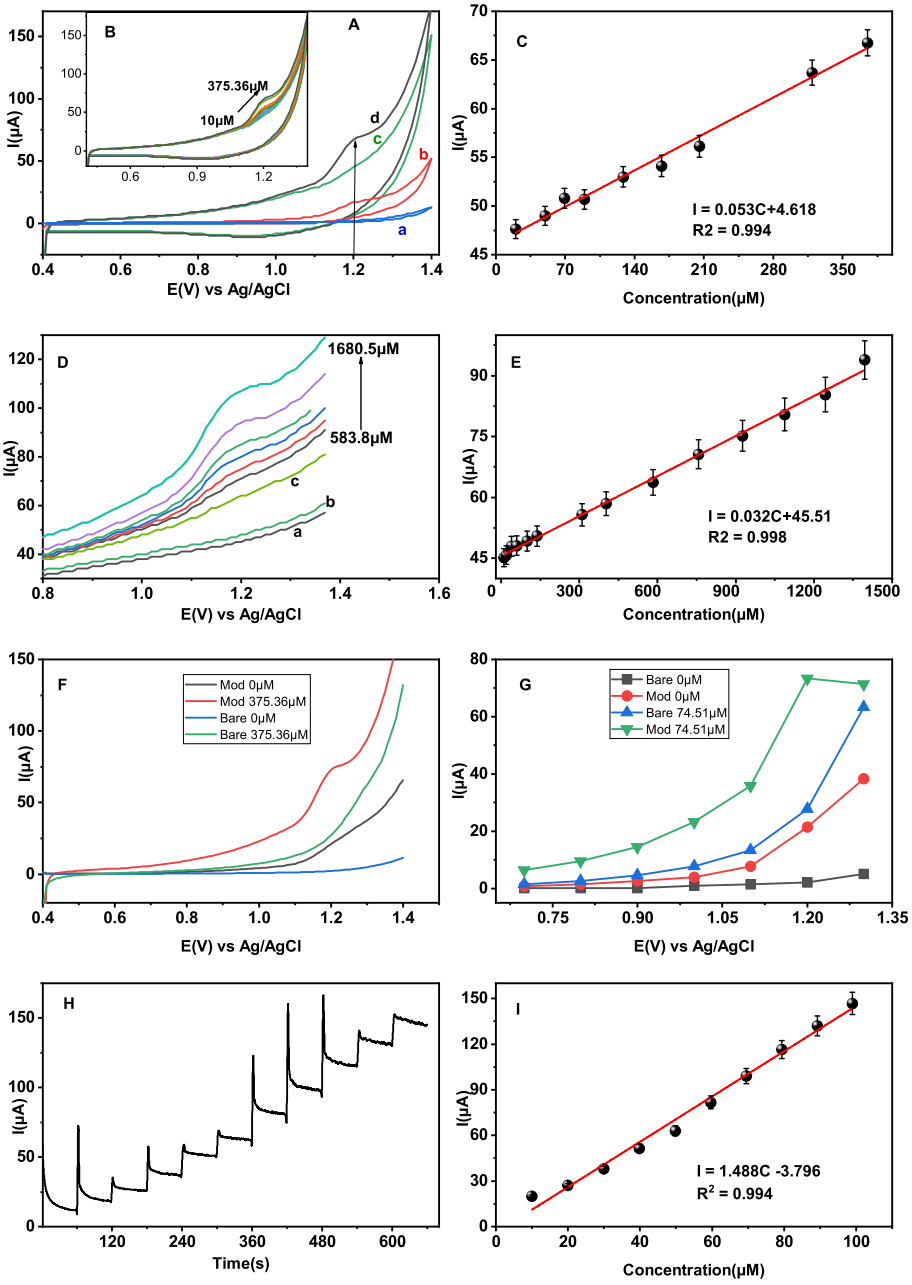


Figure 33 – Thymine Detection: (A) CV: curve (a) refers to Bare 0μM, curve (b) Bare 375.36μM, curve (c) Mod 0μM and curve (d) Mod 375.36μM; (B) CV with various concentrations; (C) CV test calibration curve; (D) DPV: curve (a) refers to Bare 0μM, curve (b) Bare 1680.5μM and curve (c) Mod 0μM; (E) DPV test calibration curve; (F) LSV; (G) LSV summary; (H) Chronoamperometry; (I) Chronoamperometry test calibration curve.

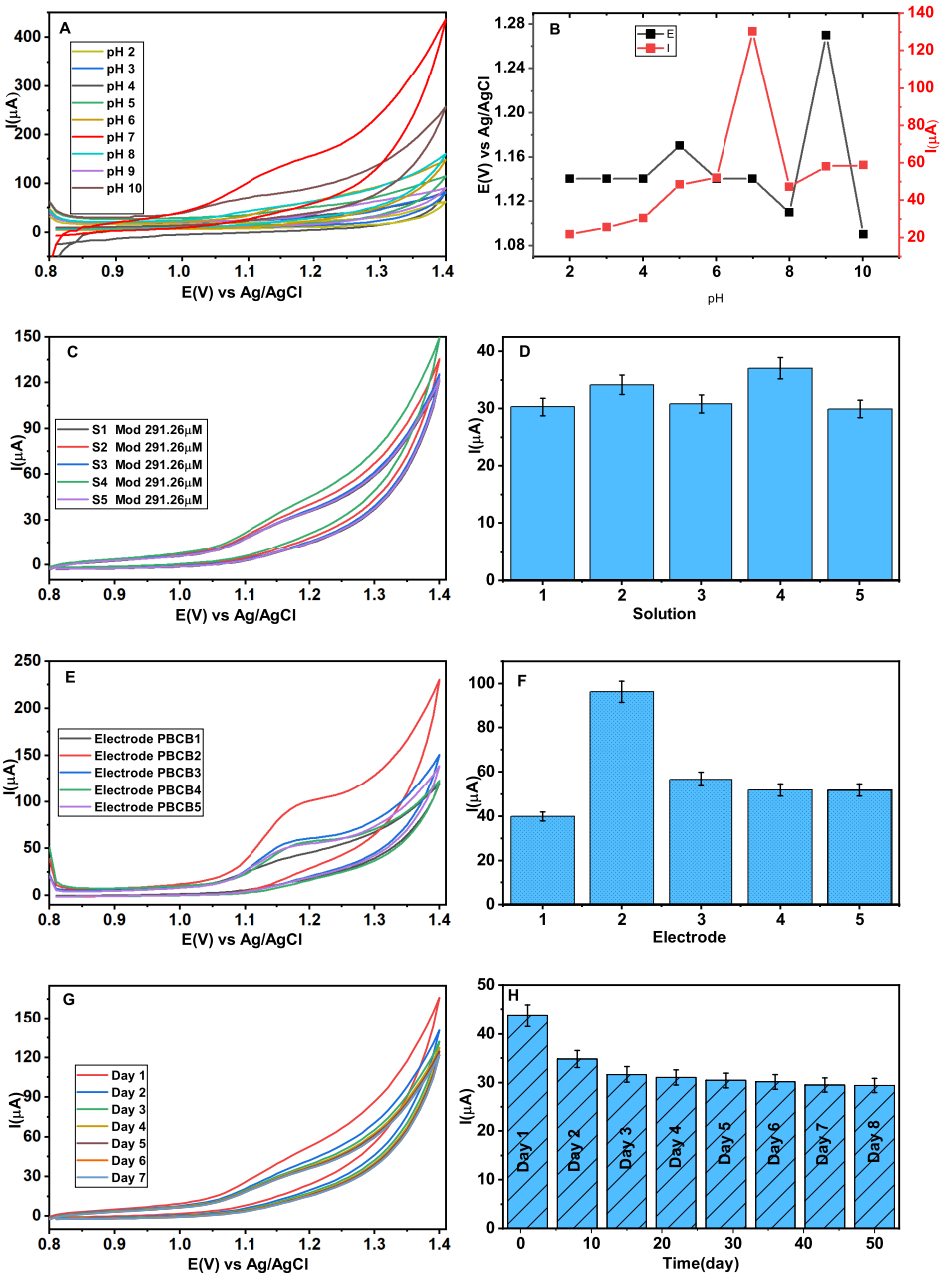


Figure 34 – Thymine Validation: (A) pH; (B) pH Summary; (C) Repeatability; (D) Repeatability Summary; (E) Reproducibility; (F) Reproducibility Summary; (G) Stability; (H) Stability Summary.

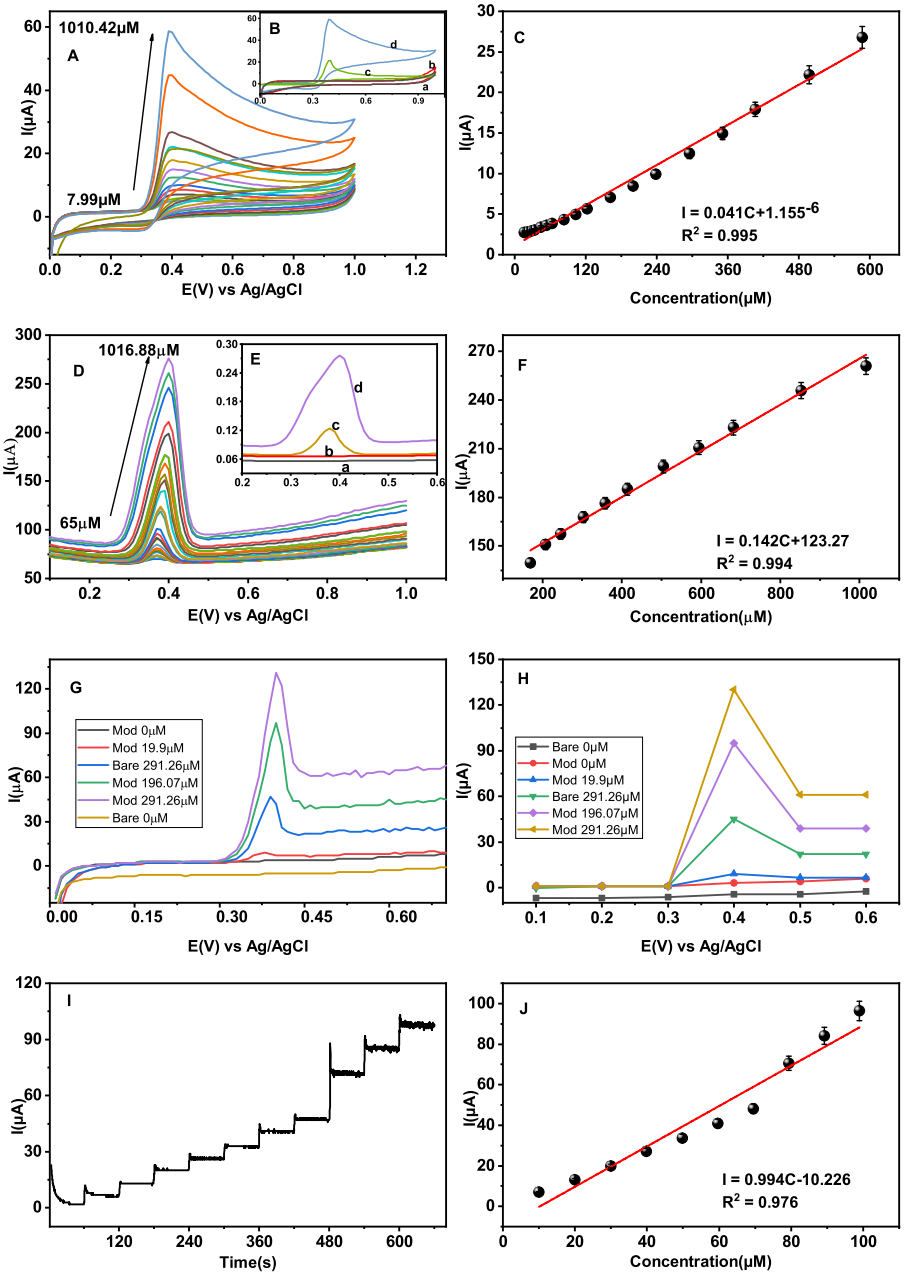


Figure 35 – Uric acid detection: (A) CV; (B) CV referring to curve (a) Bare 0μM, curve (b) Mod 0μM, curve (c) Bare 1010.42μM and curve (d) Mod 1010.42μM; (C) CV test calibration curve; (D) DPV; (E) DPV: curve (a) referring to Bare 0μM, curve (b) Mod 0μM, curve (c) Bare 1016.88μM and curve (d) Mod 1016.88μM; (F) DPV test calibration curve; (G) LSV; (H) LSV summary; Chronoamperometry; (J) Chronoamperometry test calibration curve.

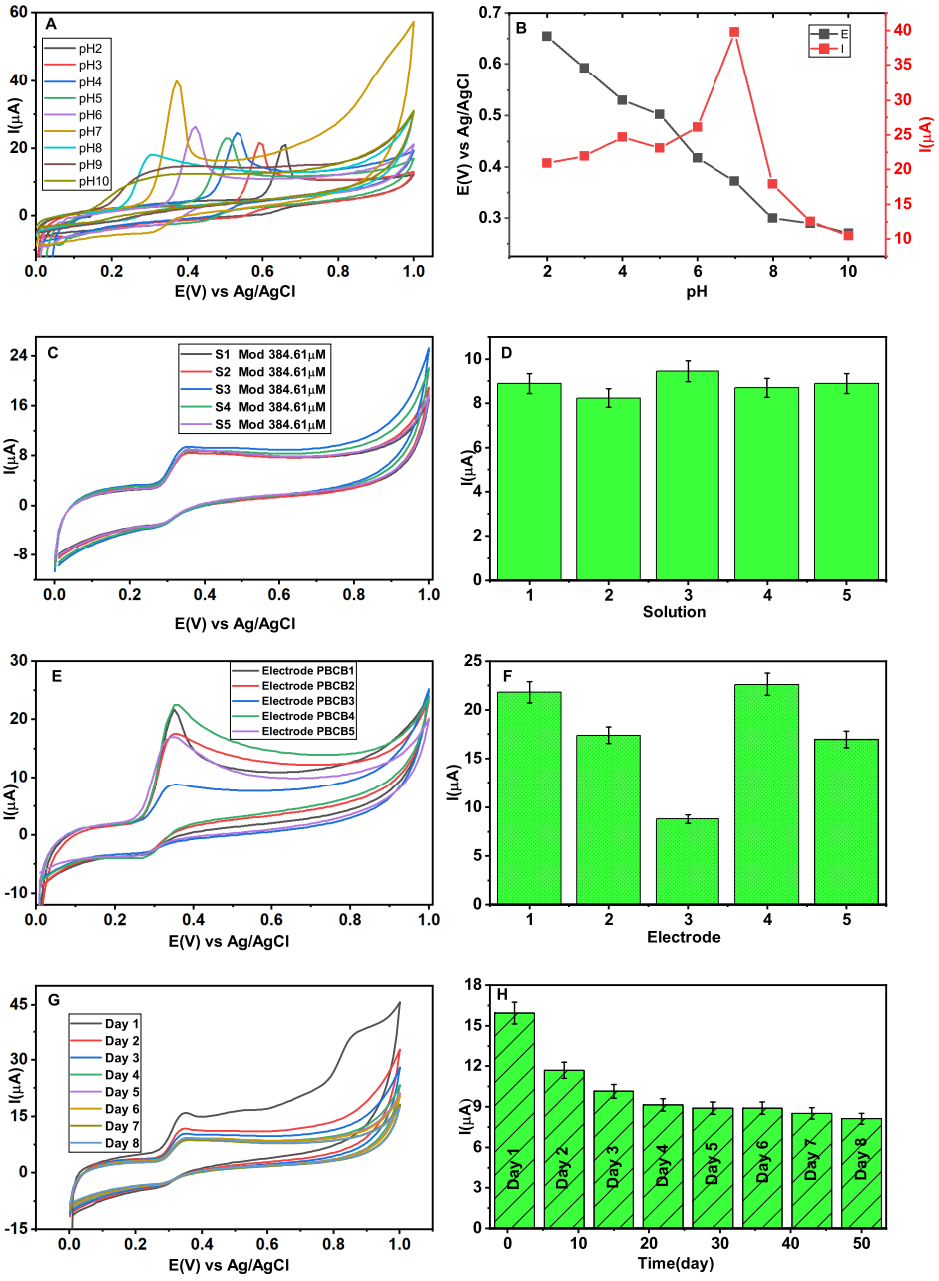


Figure 36 – Uric Acid Validation: (A) pH; (B) pH Summary; (C) Repeatability; (D) Repeatability Summary; (E) Reproducibility; (F) Reproducibility Summary; (G) Stability; (H) Stability Summary.

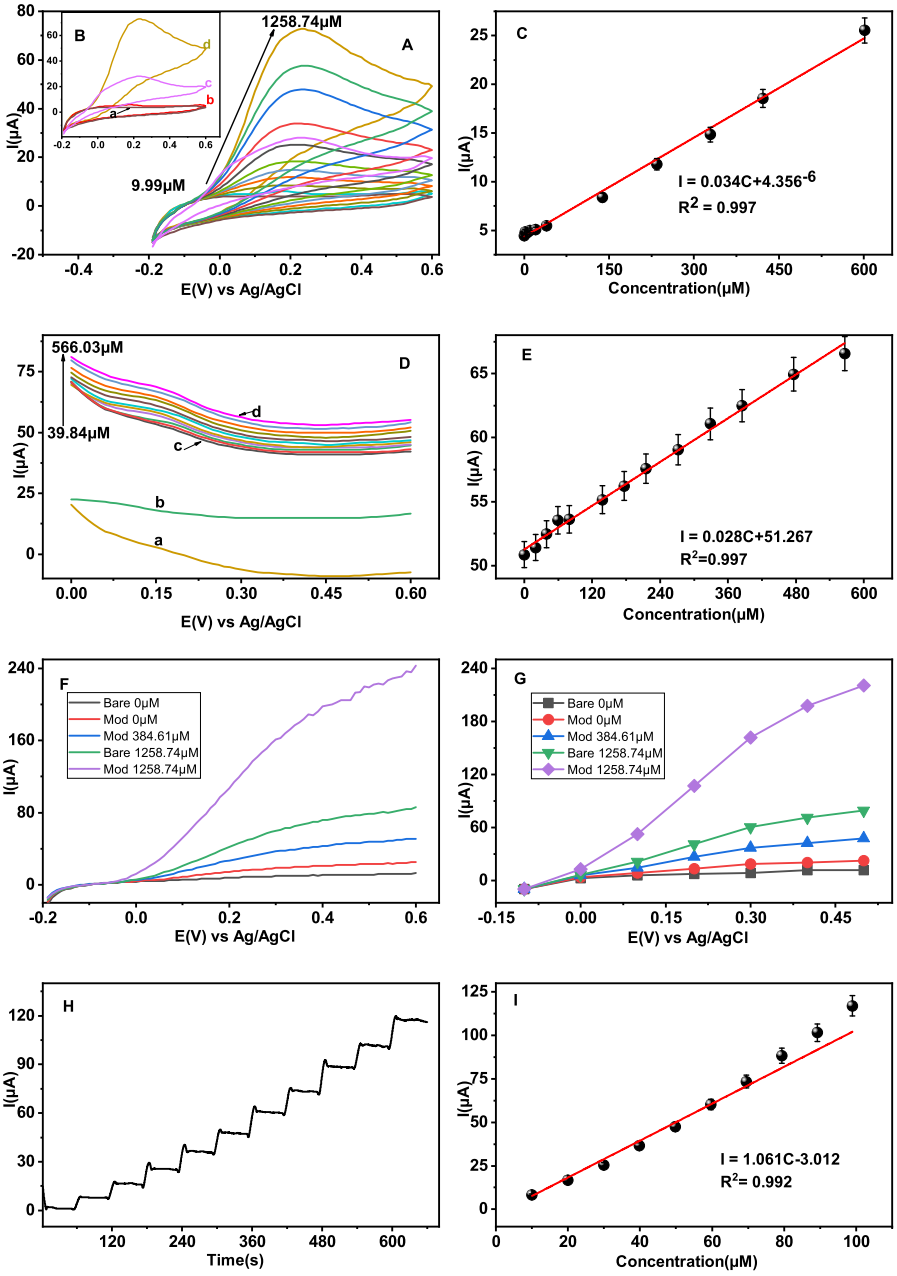


Figure 37 – Ascorbic Acid Detection: (A) CV; (B) CV for curve (a) referring to Mod 0μM, curve (b) Mod 9.99 μM, curve (c) Bare 1258.74 μM and curve (d) Mod 1258.74μM; (C) CV test calibration curve; (D) DPV: curve (a) referring to Bare 0μM, curve (b) Bare 566.03 μM, curve (c) Mod 0μM and curve (d) Mod 566.03μM; (E) DPV test calibration curve; (F) LSV; (G) LSV summary; (H) Chronoamperometry; (I) Chronoamperometry test calibration curve.

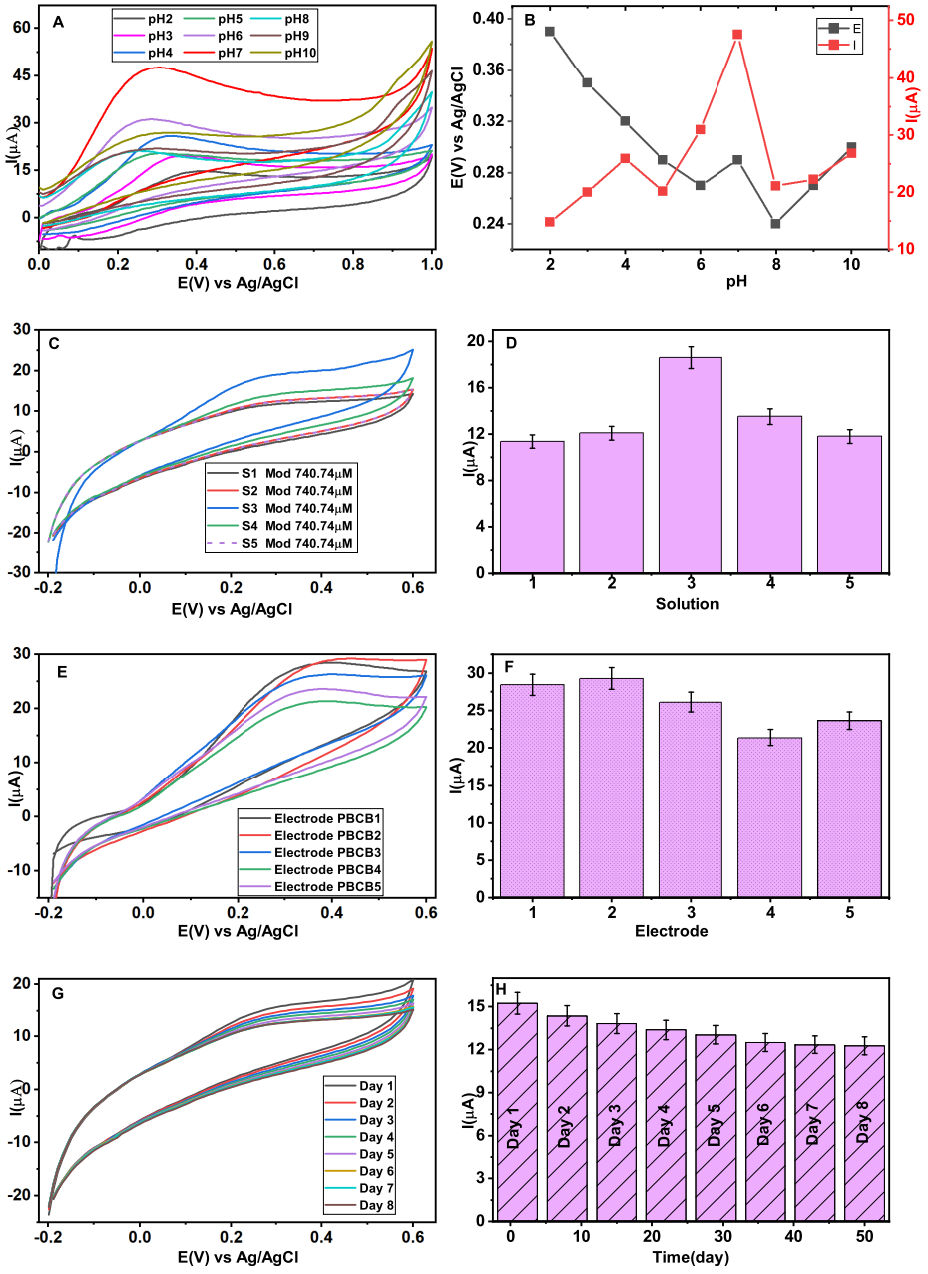


Figure 38 – Ascorbic Acid Validation: (A) pH; (B) pH Summary; (C) Repeatability; (D) Repeatability Summary; (E) Reproducibility; (F) Reproducibility Summary; (G) Stability; (H) Stability Summary.

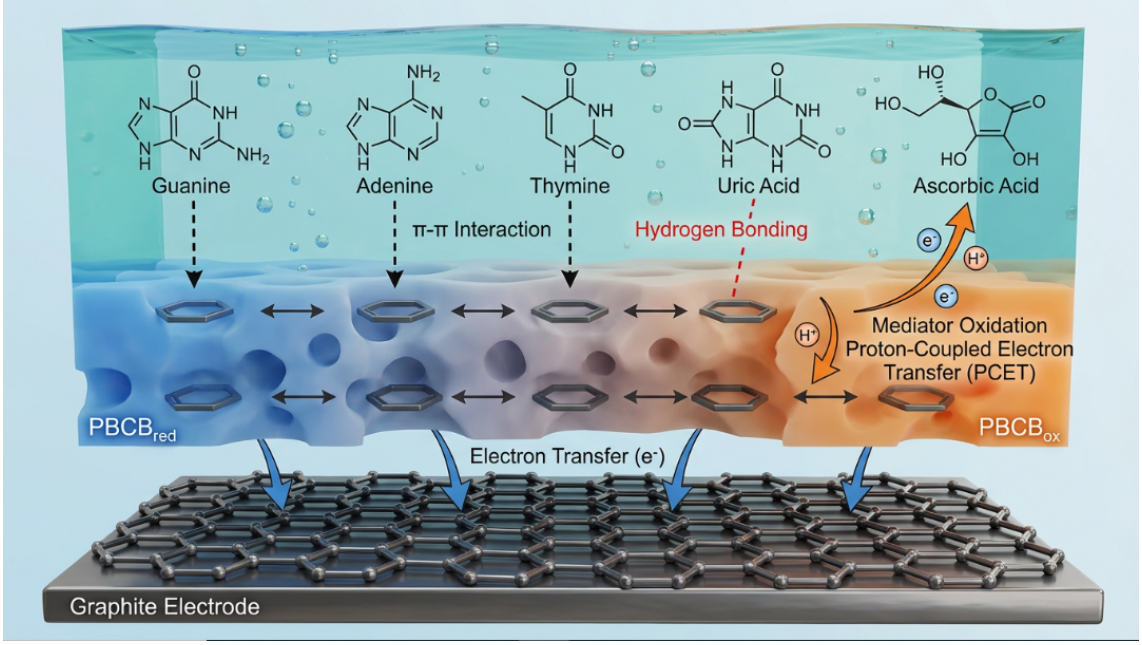


Figure 39 – Analyte detection scheme using the PBCB electrode. Figure produced by the author using artificial intelligence tools.

The nitrogenous bases Guanine, Adenine, and Thymine, which possess aromatic or pseudo-aromatic rings rich in electrons, are attracted to the surface of the PBCB film through – interactions. These interactions promote the adsorption and preconcentration of these analytes at the polymer–solution interface. The stacking of the aromatic rings of the analyte with the conjugated rings of PBCB not only brings the analyte closer to the active site of the polymer, but can also orient it in a favorable way for electron transfer, accelerating the reaction kinetics. Uric Acid and Ascorbic Acid, in turn, interact with the PBCB film predominantly through hydrogen bonding. For Ascorbic Acid, the presence of hydroxyl and carbonyl groups in both analytes allows the formation of hydrogen bridges with the functional groups of the polymer. These interactions contribute to the adsorption and stabilization of the analytes on the electrode surface, facilitating the charge transfer process. Figure 39 presents a diagram illustrating this process.

In the PBCB electrode, the detection of purines such as guanine and adenine, as well as the pyrimidine thymine, occurs through irreversible oxidation mechanisms that are strongly influenced by the acidity of the solution. For guanine and adenine, the process generally involves the transfer of two electrons and two protons ($2e^-/2H^+$) at pH values close to neutrality, resulting in the formation of oxidized derivatives such as 8-oxoguanine and 8-oxoadenine. Thymine, in turn, exhibits a more complex mechanism that may involve

the formation of radical intermediates, but it maintains a linear dependence of the peak potential (E_p) on pH, indicating the participation of protons in the rate-determining step. Uric acid and ascorbic acid, classical analytes for PBCB, follow $2e^-/2H^+$ stoichiometries. In the case of uric acid, oxidation leads to the formation of allantoin via an unstable diimine intermediate, whereas ascorbic acid is oxidized to dehydroascorbic acid.

4.2.2 Results of analytes identified by the PBP electrode.

The Table 8 presents a compilation of the results shown in Figures 40, 42, 44, 46, and 48, in addition to presenting the values of LD, LQ, and Sensitivity of the tests CV, DPV, and CA. Catechol used a potential window from -0.2 V to 1.0 V for the CV, DPV, and LSV tests; for resorcinol and hydrazine, a window from 0.0 V to 8.0 V was required, and for pyrogallol and hydroquinone, the potential window was from -0.4 V to 0.8 V for the same voltammetric tests.

The experiments carried out by cyclic voltammetry (CV) showed a linear relationship between current and concentration for all analytes studied. For catechol and resorcinol, wide linear ranges were observed between 30 - 1469.03 µM and 8 - 1471.94 µM, with high correlation coefficients (R^2 = 0.994 and 0.988, respectively). For hydroquinone, the linear range was between 20 and 1170.75 µM, with R^2 = 0.991, while for hydrazine the linear response was observed between 50 and 2038.2 µM (R^2 = 0.996). In the case of pyrogallol acid, the detection range varied between 20 and 1323.96 µM, with R^2 = 0.998, indicating excellent linear fitting. The limits of detection obtained by CV were 28.971 µM (catechol), 7.245 µM (resorcinol), 11.929 µM and 198.086 µM (hydroquinone), 42.201 µM (hydrazine), and 16.311 µM (pyrogallol acid). The calculated sensitivities ranged from 0.012 to 0.087 µA μM^{-1}, evidencing different levels of electrocatalytic response depending on the analyte analyzed.

The differential pulse voltammetry (DPV) technique also showed good analytical performance, with high correlation coefficients for all the compounds analyzed (R^2 between 0.938 and 0.996). The linear ranges observed were similar to those obtained by CV for some analytes, namely 65–1469.03 µM for catechol and resorcinol, 30–1471.94 µM for hydroquinone, 19.96–942.02 µM for hydrazine, and 1.99–1323.93 µM for pyrogallol. The detection limits obtained were 63.821 µM for catechol, 15.799 µM for resorcinol, 24.181 µM for hydroquinone, 7.499 µM and 62.928 µM for hydrazine, and 0.830 µM for pyrogal-

Table 8 – Compilation of information from tests performed with analytes detected by the PBP electrode.

Parâmetros	Catechol	Resorcinol	Hydroquinone	Hydrazine	Pyrogallic acid
CV [1]Plot	[5]Fig 40 A - B	[5]Fig 42 A - B	[5]Fig 44 A - B	[5]Fig 46 A - B	[5]Fig 48 A - B
CV - Range (μM)	30 - 1469.03	8 - 1471.94	20 - 1170.75	50 - 2038.22	20 - 1323.96
CV - [2]Ep (V)	0.08	0.45	0.01	0.65	0.14
CV - [3]Line - [1]Plot	[5]Fig 40 C	[5]Fig 42 C	[5]Fig 44 C	[5]Fig 46 C	[5]Fig 48 C
CV - R^2	[7]L 0.994 [8]H 0.988	0.988	[7]L 0.991 [8]H 0.993	0.996	0.998
CV - LD (μM)	28.971	7.245	[7]L 19.299 [8]H 198.086	42.201	16.311
CV - LQ (μM)	87.791	21.957	[7]L 60.372 [8]H 600.261	127.882	49.429
CV - [4]Sens (μA$\mu\,M^{-1}$)	[7]L 0.106 [8]H 0.039	0.042	[7]L 0.052 [8]H 0.121	0.098	0.094
DPV [1]Plot	[5]Fig 40 D - E	[5]Fig 42 D - E	[5]Fig 44 D - E	[5]Fig 46 D - E	[5]Fig 48 D - E
DPV - Range (μM)	65 - 1469.03	20 - 1469.03	30 - 1471.94	19.96 - 942.02	1.99 - 1323.93
DPV - [2]Ep (V)	0.04	0.57	0.02	0.62	0.11
DPV - [3]Line - [1]Plot	[5]Fig 40 F	[5]Fig 42 F	[5]Fig 44 F	[5]Fig 46 F	[5]Fig 48 F
DPV - R^2	0.992	0.988	0.993	[7]L 0.994 [8]H 0.998	0.999
DPV - LD (μM)	63.821	15.799	24.181	[7]L 7.499 [8]H 62.928	0.830
DPV - LQ (μM)	193.397	47.877	73.276	22.724 H 190.693	2.517
DPV - [4]Sens (μA$\mu\,M^{-1}$)	0.037	0.021	0.028	[7]L 0.040 [8]H 0.145	0.661
LSV [1]Plot	[5]Fig 40 G	[5]Fig 42 G	[5]Fig 44 G	[5]Fig 46 G	[5]Fig 48 G
LSV [6]Concent (μM)	118.57 and 196.07	196.07	99 and 291.26	2038.2	3124.43 and 1323.96
LSV - [2]Ep (V)	0.07	0.6	0.02	0.6	0.1
CA - [1]Plot	[5]Fig 40 H	[5]Fig 42 H	[5]Fig 44 H	[5]Fig 46 H	[5]Fig 48 H
CA - Time (ms)	10	22	14	14	16
CA - [3]Line - [1]Plot	[5]Fig 40 I	[5]Fig 42 I	[5]Fig 44 I	[5]Fig 46 I	[5]Fig 48 I
CA - R^2	0.998	0.993	0.992	0.996	0.989
CA - LD (μM)	1.895	5.073	4.223	30.250	47.515
CA - LQ (μM)	5.740	15.373	12.797	91.666	143.985
CA - [4]Sens (μA$\mu\,M^{-1}$)	0.294	0.492	0.136	0.031	0.023

[1]Graphic, [2]Peak detection voltage or peak potential,[3]Linear regression or calibration curve, [4]Sensitivity, [5]Figure and [6]Concentration, [7]Low concentration, [8]High concentration.

lol, demonstrating that, in some cases, the DPV technique allows the detection of lower analyte concentrations. The calculated sensitivities ranged from 0.021 to 0.661 µA µM^{-1}, indicating an electrochemical response dependent on the chemical characteristics of each compound.

The linear sweep voltammetry (LSV) experiments confirmed the ability of the modified electrode to detect these analytes over different concentration ranges. Notable ranges are 118.57–196.07 µM for catechol, 196.07 µM for resorcinol, 99–291.26 µM for hydroquinone, 2038.2 µM for hydrazine, and 3124.43–1323.96 µM for pyrogallol, showing that each analyte exhibits a characteristic electrochemical behavior in relation to the applied potential. In chronoamperometry (CA), the results also indicated good linearity, with R^2 values between 0.989 and 0.998. The calculated detection limits were 1.895 µM for catechol, 5.073 µM for resorcinol, 4.223 µM for hydroquinone, 30.250 µM for hydrazine, and 47.515 µM for pyrogallol, while the sensitivities ranged from 0.023 to 0.492 µA µM^{-1}. These results demonstrate that the amperometric technique is also suitable for the quantification of these analytes, exhibiting a good electroanalytical response. The response

time presented by the PBCB electrode was between 10 and 22 s, as shown in Table 8, line "CA - Time".

Table 9 presents the analytical validation parameters obtained for the detection of catechol, resorcinol, hydroquinone, hydrazine, and pyrogallol, including the studies of repeatability, reproducibility, and stability, evaluated before and after the statistical treatment of the data. Initially, the relative standard deviation (RSD) values were calculated from the sets of experimental measurements (ini). Subsequently, the Dixon Q and Grubbs G statistical tests were applied in order to identify possible discrepant values (outliers). When applicable, these tests allowed the data set to be refined, yielding final values (end) with greater statistical reliability. In cases where the test values did not fall within the limits or could not be applied, NA (not applicable) was indicated.

Table 9 – Compilation of information from validation tests with analytes detected by the PBP electrode.

Validation Parameters	Catechol	Resorcinol	Hydroquinone	Hydrazine	Pyrogallic acid
[2]Repet [1]Plot	[5]Fig 41 C - D	[5]Fig 43 C - D	[5]Fig 45 C - D	[5]Fig 47 C - D	[5]Fig 49 C - D
[3]RSD [2]Repet [4]ini (%)	26.925	14.914	4.231	12.583	16.463
[6]Q [5]2Repet	0.604 (80%)	0.244 ([11]NA)	-	0.782 (95%)	0.137 ([11]NA)
Gs Repet	1.773 (95%)	1.312 ([11]NA)	-	1.756 (95%)	1.207 ([11]NA)
[3]RSD [2]Repet [8]end (%)	16.539	12.004	-	2.924	-
[9]Reprod [1]Plot	[5]Fig 41 E - F	Fig 43 E - F	[5]Fig 45 E - F	Fig 47 E - F	[5]Fig 49 E - F
[3]RSD [9]Reprod [4]ini (%)	42.649	22.160	25.641	44.680	21.853
[6]Q [9]Reprod	0.565 (80%)	0.563 (80%)	0.085 ([11]NA)	0.614 (85%)	0.557 (80%)
[7]Gs [9]Reprod	1.669 (85%)	1.665 (85%)	0.859 ([11]NA)	1.618 (85%)	1.555 (80%)
[3]RSD [9]Reprod [8]end (%)	27.368	11.978	-	26.827	12.097
[10]Stab [1]Plot	[5]Fig 41 E - F	[5]Fig 43 G - H	[5]Fig 45 G - H	[5]Fig 47 G - H	[5]Fig 49 G - H
[10]Stab [12]ret [4]ini (%)	68.935	80.242	84.829	82.579	58.063
[3]RSD [10]Stab [4]ini (%)	12.914	9.391	5.530	6.619	19.107
[6]Q [10]Stab	0.429 (80%)	0.048 ([11]NA)	0.558 (95%)	0.401 (80%)	0.333 ([11]NA)
[7]Gs [10]Stab	1.953 (85%)	1.230 ([11]NA)	2.173 (95%)	2.093 (90%)	1.949 (90%)
[10]Stab [12]ret [8]end (%)	79.534	-	92.510	88.080	67.495
[3]RSD [10]Stab [8]end (%)	8.886	-	2.909	4.689	13.430

[1]Graphic, [2]Repeatability, [3]Relative Standard Deviation, [4]Initial Result, [5]Figure, [6]Q Dixon, [7]G Grubbs, [8]Final Result, [9]Reproducibility, [10]Stability,[11]Not Apply and [12]Retention.

In the repeatability study, which evaluates the precision of successive measure-

ments performed under the same experimental conditions, the initial RSD values ranged from 4.231% to 26.925% for the analytes investigated. After applying the statistical tests and, when necessary, removing outliers, a reduction in data dispersion was observed for some analytes, resulting in final RSD Repet end values of 16.539% for catechol, 12.004% for resorcinol, and 2.924% for hydrazine. For hydroquinone, the Q and Gs tests were not necessary because it showed an RSD lower than 5% (4.231%), whereas for pyrogallol, the statistical tests could not be applied because the Q and Gs tests did not indicate the possible presence of an outlier, and thus the original results were maintained. The reduction observed in some cases shows that the exclusion of atypical measurements contributed to improving the statistical consistency of the electrochemical responses.

Reproducibility, which reflects the ability of the method to provide consistent responses in different independent measurements, initially showed relatively high RSD values for some analytes, such as catechol (42.649%), resorcinol (22.160%), hydroquinone (25.641%), and hydrazine (44.680%), indicating greater dispersion among the experimental results. After applying the Dixon and Grubbs tests, a reduction in RSD values was observed for certain analytes, resulting in 27.368% for catechol, 11.978% for resorcinol, 26.827% for hydrazine, and 12.097% for pyrogallol, while for hydroquinone the tests were not applicable. These results indicate that part of the initial variability was associated with outlying measurements, whose exclusion allowed for a more consistent statistical representation of the sensor's behavior. The stability study was evaluated through the initial signal retention stability (Stab ret ini), which represents the percentage of electrochemical response preserved over the sensor storage period. The values obtained ranged from 58.063% to 84.829%, indicating that a significant fraction of the electrochemical response was maintained over time for all analytes evaluated. The initial RSD values for stability ranged from 5.530% to 19.107%, reflecting experimental variations between the measurements performed.

After applying the statistical tests, final retention stability values (Stab ret end) were obtained, accompanied by lower dispersion values. The results of 92.510% for hydroquinone, 88.080% for hydrazine, 79.534% for catechol, and 67.495% for pyrogallol stand out, with corresponding final RSD values of 2.909%, 4.689%, 8.886%, and 13.430%, indicating improved statistical consistency of the data after treatment. For resorcinol, the tests were not applicable at this stage.

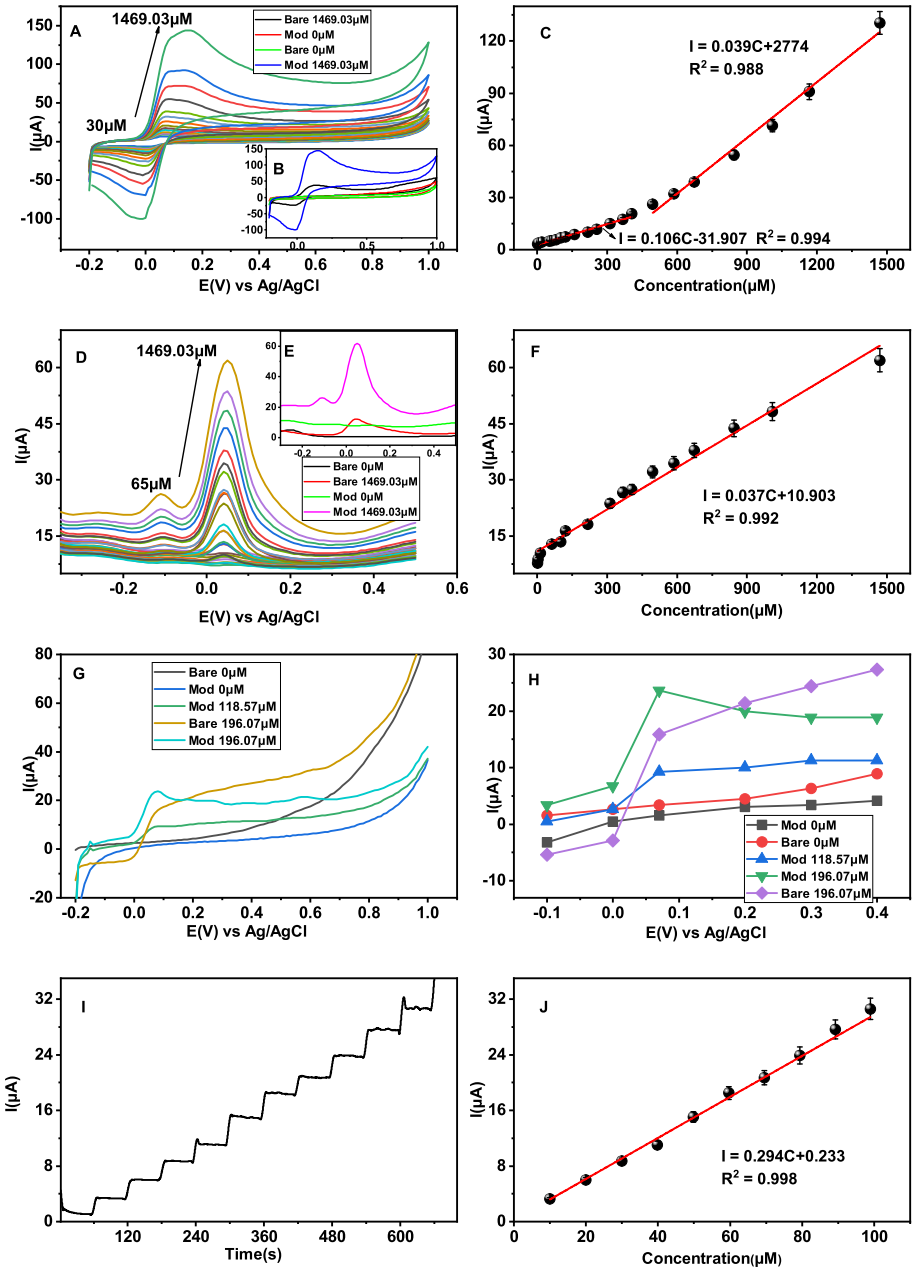


Figure 40 – Catechol Detection: (A) CV; (B) CV with various concentrations; (C) CV test calibration curve; (D) DPV; (E) DPV test calibration curve; (F) LSV; (G) LSV summary; (H) Chronoamperometry; (I) Chronoamperometry test calibration curve.

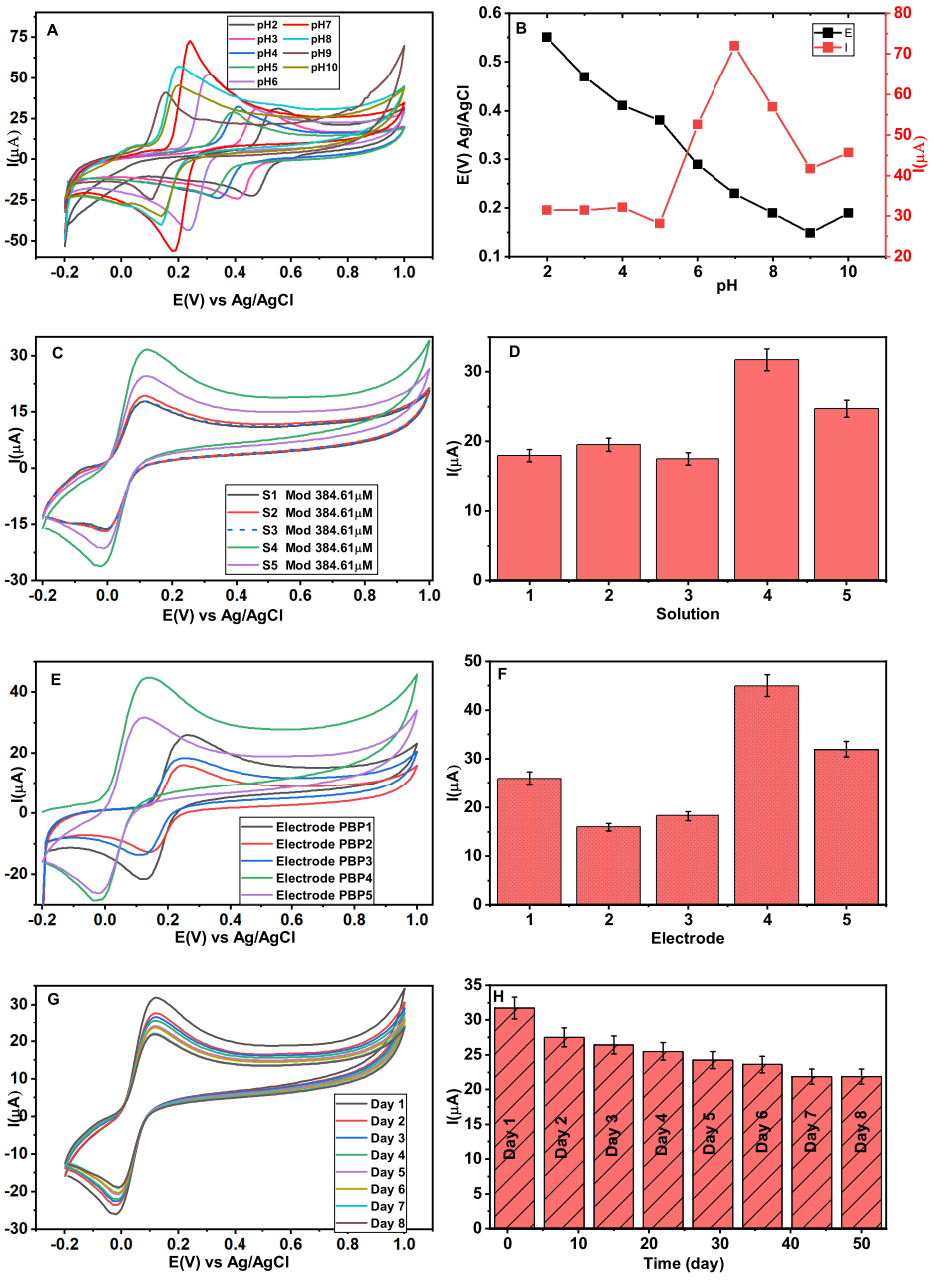


Figure 41 – Catechol Validation: (A) pH; (B) pH Summary; (C) Repeatability; (D) Repeatability Summary; (E) Reproducibility; (F) Reproducibility Summary; (G) Stability; (H) Stability Summary.

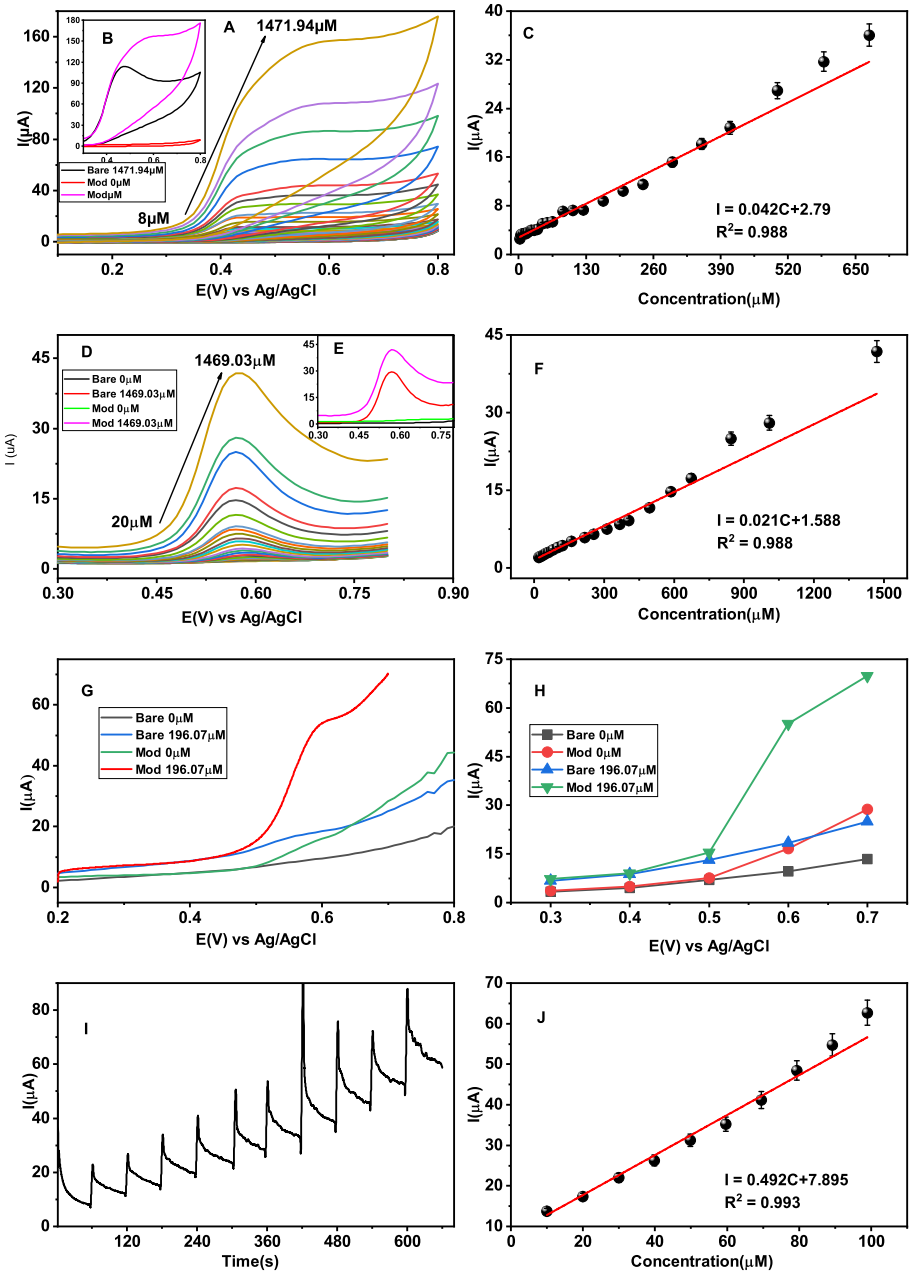


Figure 42 – Resorcinol Detection: (A) CV; (B) CV with various concentrations; (C) CV test calibration curve; (D) DPV; (E) DPV test calibration curve; (F) LSV; (G) LSV summary; (H) Chronoamperometry; (I) Chronoamperometry test calibration curve.

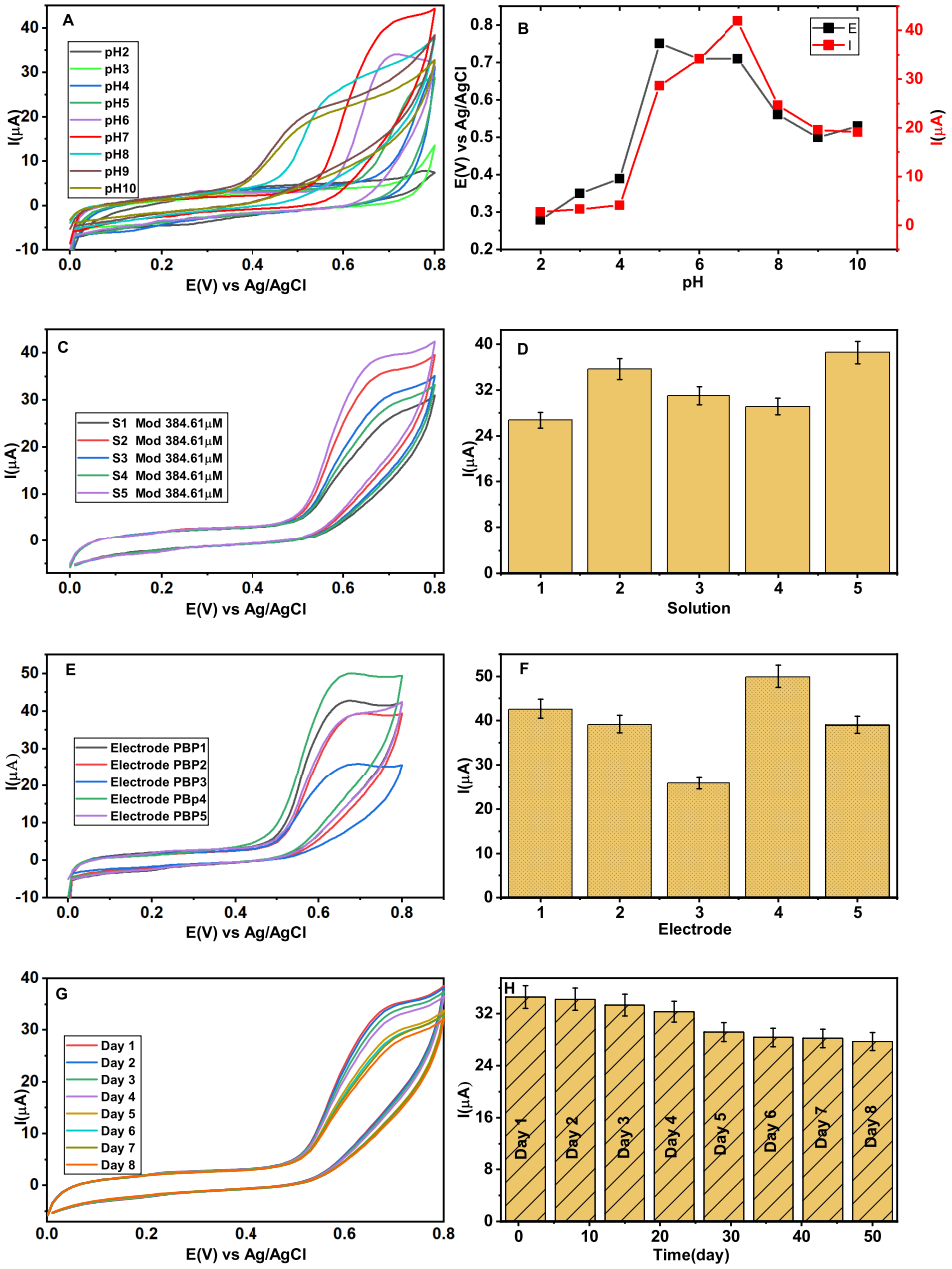


Figure 43 – Resorcinol Validation: (A) pH; (B) pH Summary; (C) Repeatability; (D) Repeatability Summary; (E) Reproducibility; (F) Reproducibility Summary; (G) Stability; (H) Stability Summary.

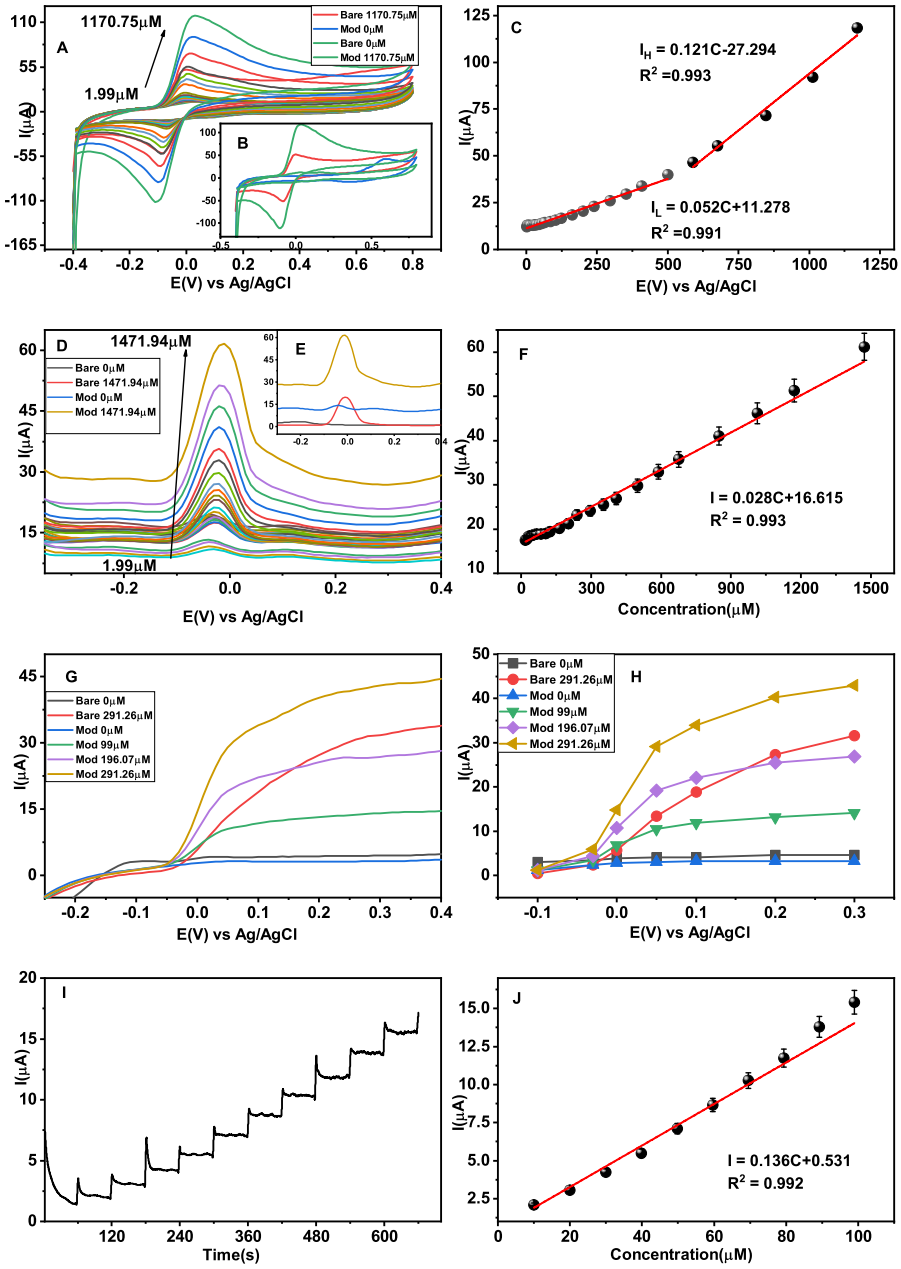


Figure 44 – Hydroquinone Detection: (A) CV with various concentrations; (B) CV ; (C) CV test calibration curve; (D) DPV; (E) DPV test calibration curve; (F) LSV; (G) LSV summary; (H) Chronoamperometry; (I) Chronoamperometry test calibration curve.

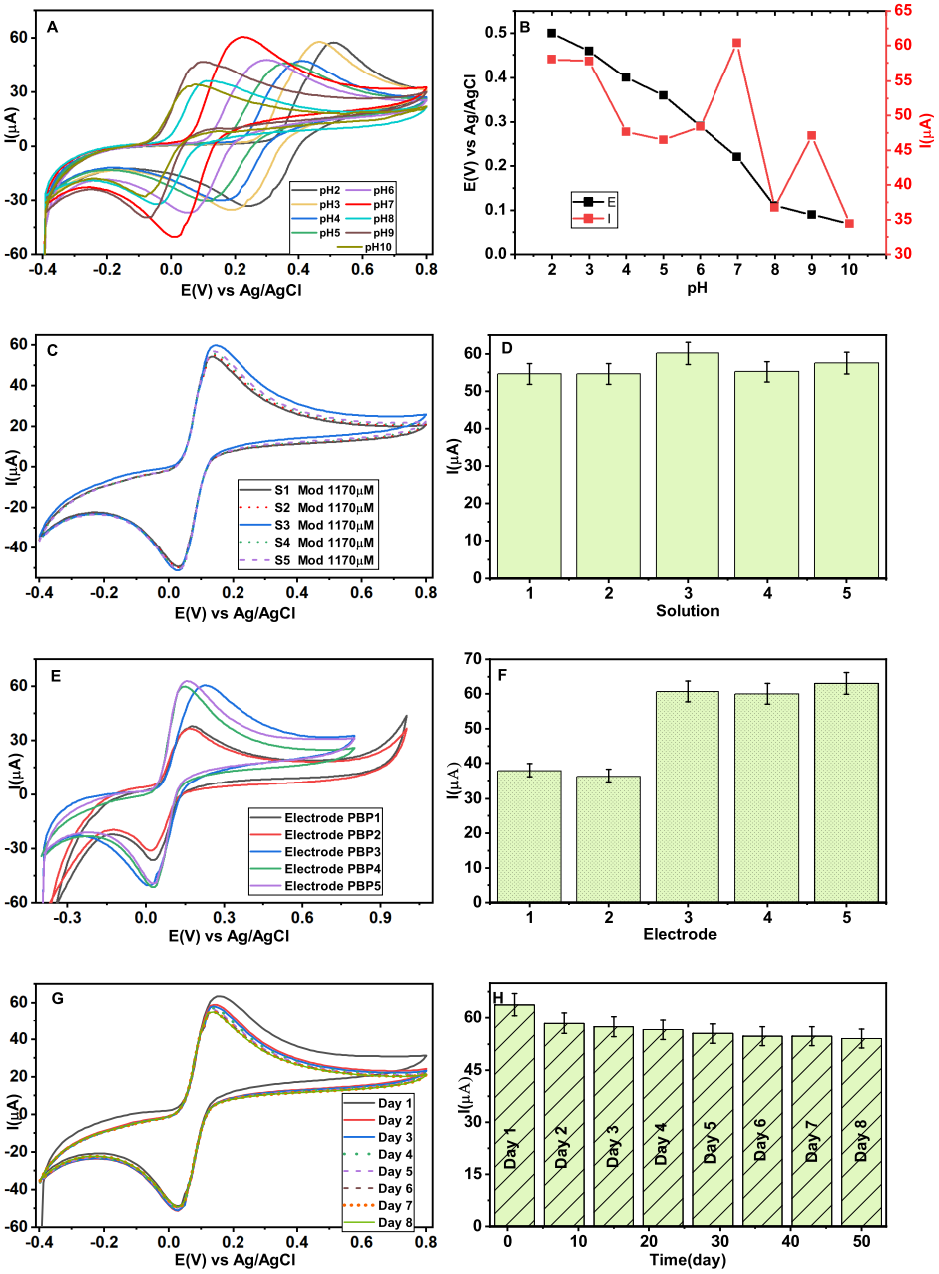


Figure 45 – Hydroquinone Validation: (A) pH; (B) pH Summary; (C) Repeatability; (D) Repeatability Summary; (E) Reproducibility; (F) Reproducibility Summary; (G) Stability; (H) Stability Summary.

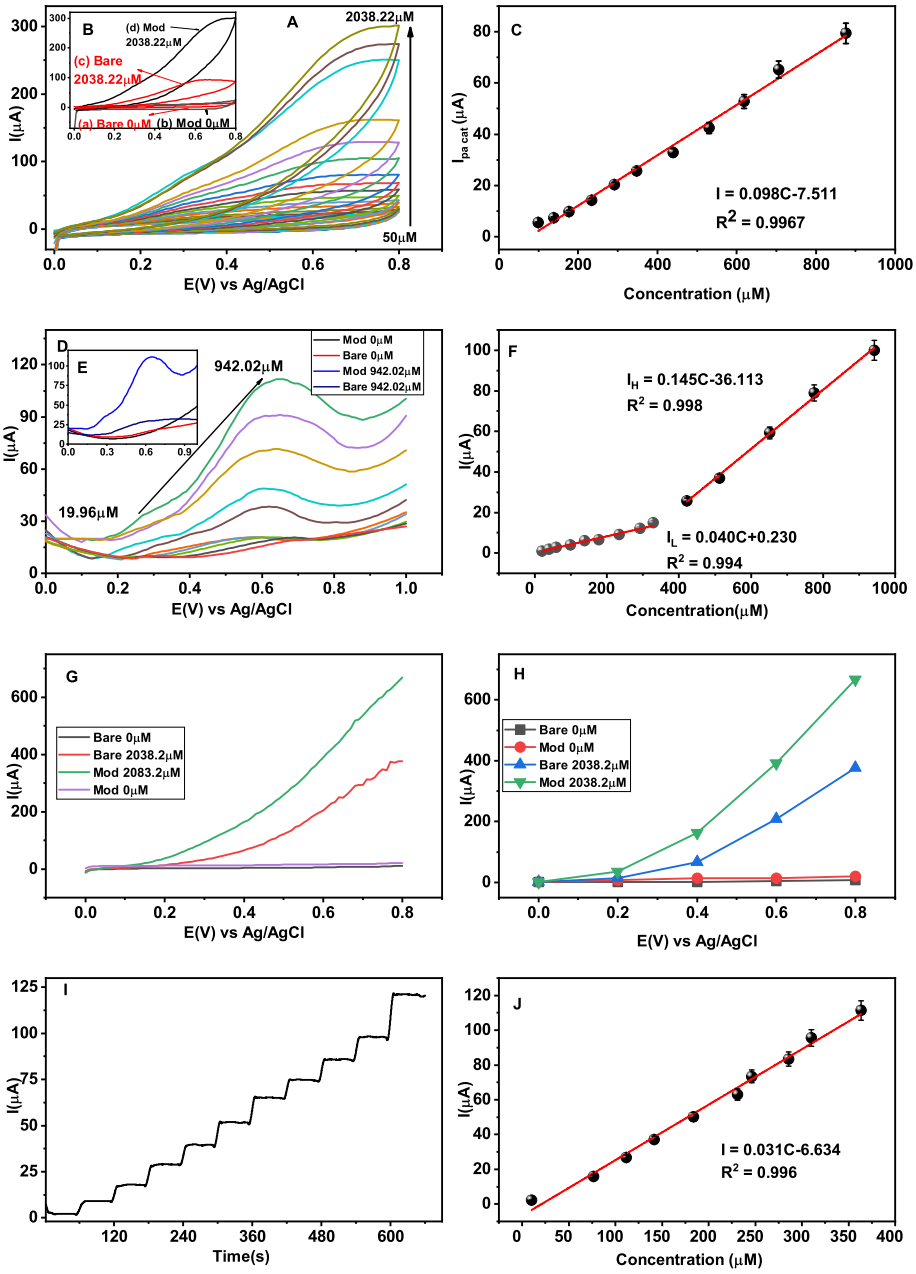


Figure 46 – Hydrazine Detection: (A) CV; (B) CV with various concentrations; (C) CV test calibration curve; (D) DPV; (E) DPV test calibration curve; (F) LSV; (G) LSV summary; (H) Chronoamperometry; (I) Chronoamperometry test calibration curve.

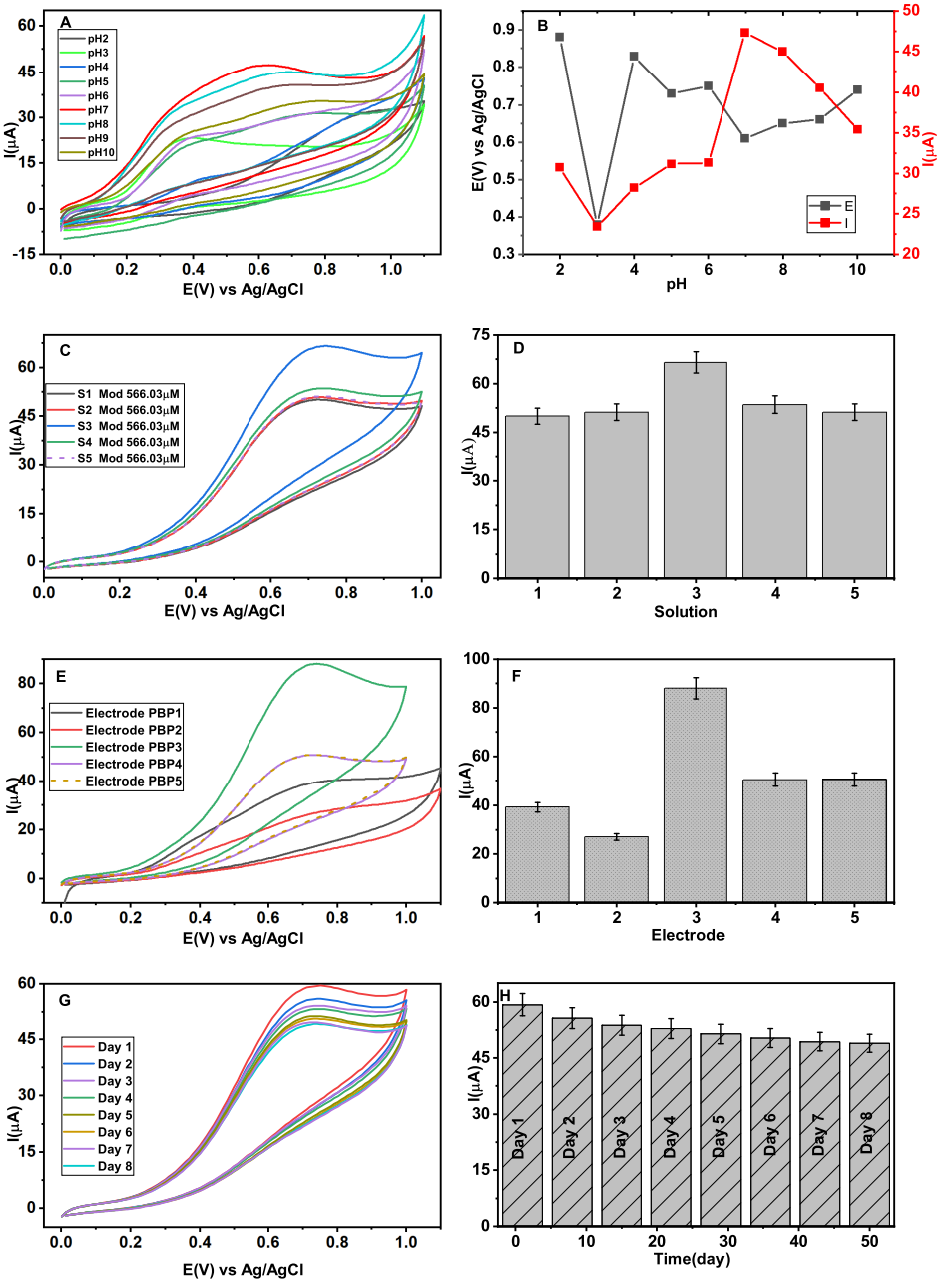


Figure 47 – Hydrazine Validation: (A) pH; (B) pH Summary; (C) Repeatability; (D) Repeatability Summary; (E) Reproducibility; (F) Reproducibility Summary; (G) Stability; (H) Stability Summary.

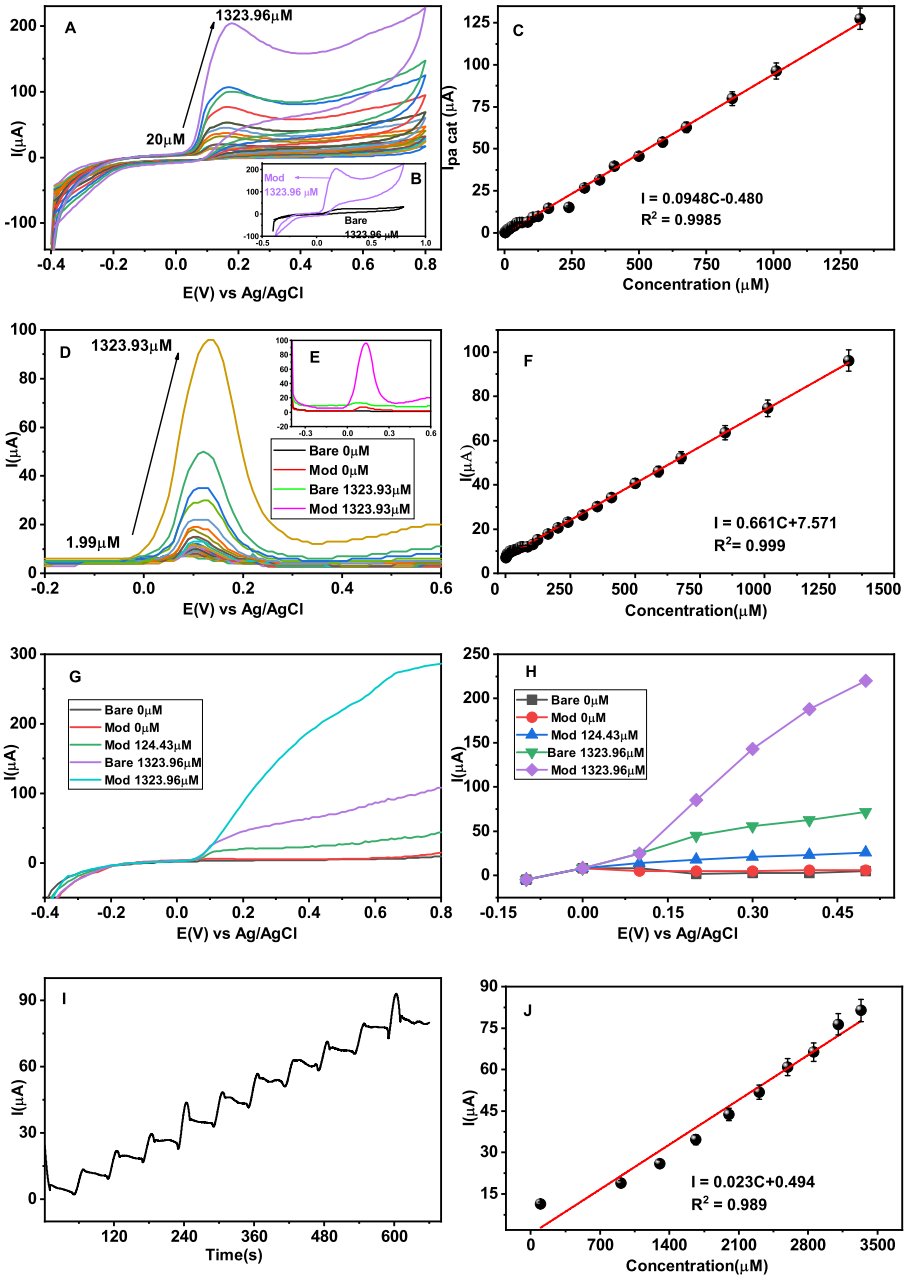


Figure 48 – Pyrogallic Acid Detection: (A) CV; (B) CV with various concentrations; (C) CV test calibration curve; (D) DPV; (E) DPV test calibration curve; (F) LSV; (G) LSV summary; (H) Chronoamperometry; (I) Chronoamperometry test calibration curve.

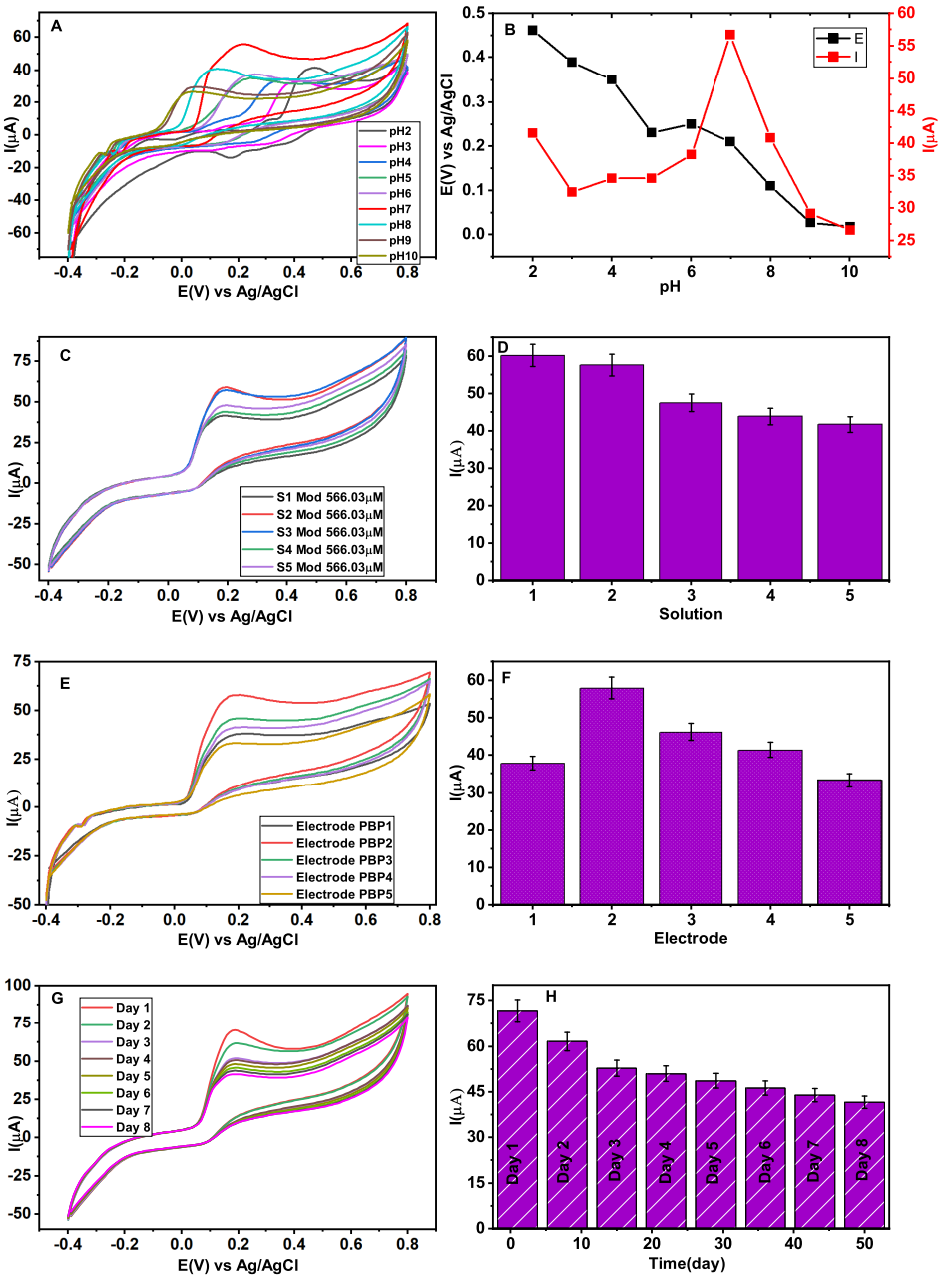


Figure 49 – Pyrogallic Acid Validation: (A) pH; (B) pH Summary; (C) Repeatability; (D) Repeatability Summary; (E) Reproducibility; (F) Reproducibility Summary; (G) Stability; (H) Stability Summary.

PBP in its reduced form (PBP*red*) is electrochemically oxidized at the graphite electrode, losing electrons (e^-) that are transferred to the conductive substrate. This process generates the oxidized form of the mediator (PBP*ox*), which is more electroactively reactive. The oxidized form of PBP (PBP*ox*) reacts chemically with the analytes that are adsorbed on or close to the surface of the polymer. During this reaction, the analyte is oxidized, releasing electrons (e^-) and protons (H^+), which are transferred to PBP*ox*. This process regenerates PBP to its reduced form (PBP*red*), allowing the catalytic cycle to continue; Figure 50 helps to explain this process. This flow of electrons is measured as the analytical current and is proportional to the concentration of the analyte in solution.

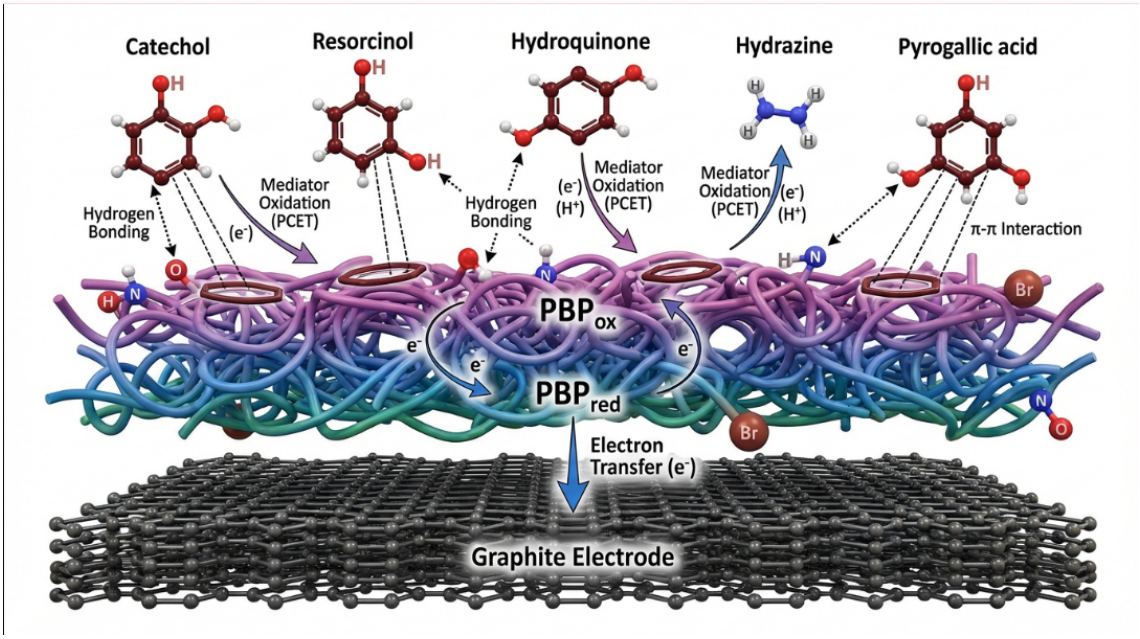


Figure 50 – Analyte detection scheme using the PBP electrode.Figure produced by the author using artificial intelligence tools.

At the PBP electrode, the selectivity in the simultaneous detection of phenolic isomers such as hydroquinone, catechol, and resorcinol is refined by pH control, which modulates the protonation state of both the polymer film and the analytes, and the isomers have hydroxyl groups that interact with the PBP film through hydrogen bonding. Hydroquinone and catechol undergo reversible oxidation to p-benzoquinone and o-benzoquinone, respectively, through a mechanism involving two electrons and two protons ($2e^-/2H^+$). Resorcinol, although a meta isomer, follows a similar stoichiometry, but with slower electron-transfer kinetics and a more positive potential due to the lower stability of its oxidized state. The detection of hydrazine at the PBP electrode is a total oxidation

process that involves the transfer of four electrons and four protons ($4e^-/4H^+$) to form molecular nitrogen (N_2), where the PBP film acts by reducing the overpotential characteristic of this slow reaction. For pyrogallol, oxidation to purpurogallin involves successive $2e^-/2H^+$ steps, and the pH dependence shows that deprotonation of the phenolic hydroxyl groups facilitates electron removal, shifting the oxidation potential to less positive values in more basic media.

4.2.3 Results of analytes identified by the PTB electrode.

The Table 10 presents the compilation of results shown in Figures 51, 53, 55, 57, and 59, as well as the values of LD, LQ, and Sensitivity of the tests CV, DPV, and CA. Vanillin used a potential window from 0.3 V to 0.8 V for the CV, DPV, and LSV tests; for tyrosine, tryptophan, and cysteine a window from 0.0 V to 1.0 V was required, and for pyridoxine the potential window was from 0.4 V to 1.0 V for the same voltammetric tests.

The electrode showed a good linear response for all the analytes investigated. Using the CV technique, the working ranges extended from low concentrations (55 µM for Tryptophan) to levels above 2450 µM (for Cysteine). The linear correlation coefficients (R^2) obtained were consistently higher than 0.990, demonstrating the high fidelity of the linear regression model applied to the calibration curves. The behavior of Tyrosine in CA stands out, with an R^2 of 0.999, indicating an extremely stable and predictable response.

The oxidation potentials Peak detection voltage or peak potential (Ep) varied according to the chemical nature of each species and the technique employed. In CV, the potentials ranged from 0.59 V (Cysteine) to 0.72 V (Tryptophan). A systematic shift toward less positive potentials was observed when using DPV, as in the case of Vanillin, whose Ep decreased from 0.64 V (CV) to 0.53 V (DPV), suggesting a facilitation of the electrode process with this technique.

In terms of analytical sensitivity, the CA technique proved to be the most effective for most analytes. Tyrosine showed the highest recorded sensitivity, 0.605 $\mu A \cdot \mu M^{-1}$ by CA, which is important for detecting minimal concentration variations in real samples.

Analyzing the detection limits, it is observed that cysteine showed the lowest LD global of 2.524 µM via CA. Vanillin achieved a limit of 7.188 µM by CA, significantly lower than the 17.110 µM obtained by CV. Both tyrosine and tryptophan presented LDs in the range of 7.6 µM to 9.8 µM via CA.

Table 10 – Compilation of information from tests performed with analytes detected by the PTB electrode.

Parameters	Vanillin	Tyrosine	Tryptophan	Cysteine	Pyridoxine
CV [1]Plot	[5]Fig 51 A - B	[5]Fig 53 A - B	[5]Fig 55 A - B	[5]Fig 57 A - B	[5]Fig 59 A - B
CV - Range (μM)	20 - 812.20	55 - 1441.29	55 - 1441.2	70 - 2447.13	40 - 1441.29
CV - [2]Ep (V)	0.64	0.65	0.72	0.59	0.68
CV - [3]Line - Plot	[5]Fig 51 C	[5]Fig 53 C	[5]Fig 55 C	[5]Fig 57 C	[5]Fig 59 C
CV - R^2	0.997	0.992	0.991	0.995	0.990
CV - LD (μM)	17.110	54.118	53.391	65.727	33.995
CV - LQ (μM)	51.849	163.996	161.793	199.173	103.015
CV - [4]Sens (μA$\mu\, M^{-1}$)	0.032	0.053	0.070	0.021	0.020
DPV [1]Plot	[5]Fig 51 D - E	[5]Fig 53 D - E	[5]Fig 55 D - E	[5]Fig 57 D - E	[5]Fig 59 D - E - F
DPV - Range (μM)	45 - 1441.29	55 - 1441.29	60 - 1441.29	70 - 2447.12	40 - 1441.29
DPV - [2]Ep (V)	0.53	0.62	0.71	0.56	0.65
DPV - [3]Line - [1]Plot	[5]Fig 51 F	[5]Fig 53 F	[5]Fig 55 F	[5]Fig 57 F	[5]Fig 59 G
DPV - R^2	0.991	0.990	0.990	0.993	0.993
DPV - LD (μM)	43.293	53.704	56.996	65.538	36.360
DPV - LQ (μM)	131.191	131.191	172.716	198.602	110.182
DPV - [4]Sens (μA$\mu\, M^{-1}$))	0.007	0.009	0.013	0.001	0.006
LSV [1]Plot	[5]Fig 51 G - H - I	[5]Fig 53 G - H - I	[5]Fig 55 G - H	[5]Fig 57 G - H	[5]Fig 59 H - I
LSV [6]Concent (μM)	23.94 - 1441.28	23.94 - 1441.28	23.94 - 1441.28	138.6 - 601.5	23.94 - 1441.28
LSV - [2]Ep (V)	0.5	0.61	0.67	0.5	0.6
CA - [1]Plot	[5]Fig 51 J	[5]Fig 53 J	[5]Fig 55 I	[5]Fig 57 I	[5]Fig 59 J
CA - Time (s)	21	24	30	13	20
CA - [3]Line -[1]Plot	[5]Fig 51 K	[5]Fig 53 K	[5]Fig 55 J	[5]Fig 57 J	[5]Fig 59 K
CA - R^2	0.991	0.999	0.990	0.994	0.995
CA - LD (μM)	7.188	7.631	9.861	2.524	9.312
CA - LQ (μM)	21.784	23.125	29.884	7.649	28.220
CA - [4]Sens (μA$\mu\, M^{-1}$)	0.179	0.605	0.106	0.546	0.430

[1]Graphic, [2]Peak detection voltage or peak potential,[3]Linear regression or calibration curve, [4]Sensitivity, [5]Figure and [6]Concentration

These results indicate that, although CV is excellent for initial characterization, CA and DPV offer greater capability for trace analyses, with LQ ranging from 7.649 µM (cysteine) to 29.884 µM (tryptophan) per CA. The response time presented by the PTB electrode was between 13 and 30 s, as shown in Table 10, line "CA - Time".

Table 11 presents the analytical validation parameters obtained for the analytes vanillin, tyrosine, tryptophan, cysteine, and pyridoxine, including the studies of repeatability, reproducibility, and electrode stability. Initially, the relative standard deviation (RSD) values were calculated from the complete set of experimental measurements (ini). Next, Dixon's Q and Grubbs' Gs statistical tests were applied in order to identify possible outliers. When identified, these points were removed, resulting in the final values (end), which represent a statistically more consistent data set. In cases where the tests were not necessary or could not be applied, the abbreviation NA (not applicable) was used.

In the repeatability study, which assesses the precision of the method under the same experimental conditions, the initial RSD Repet ini values ranged from 4.330% to

Table 11 – Compilation of information from validation tests with analytes detected by the PTB electrode.

Validation Parameters	Vanillin	Tyrosine	Tryptophan	Cysteine	Pyridoxine
[2]Repet [1]Plot	[5]Fig 52 C - D	[5]Fig 54 C - D	[5]Fig 56 C - D	[5]Fig 58 C - D	[5]Fig 60 C - D
[3]RSD [2]Repet [4]ini (%)	10.230	11.003	23.275	2.430	16.758
[6]Q [2]Repet	0.147 ([11]NA)	0.470 ([11]NA)	0.460 ([11]NA)	-	0.421 ([11]NA)
[7]Gs [2]Repet	1.498 (80%)	1.548 (80%)	1.504 (80%)	-	1.519 (80%)
[3]RSD [2]Repet [3]end (%)	9.061	6,639	16.146	-	10.907
[9]Reprod [1]Plot	[5]Fig 52 E - F	[5]Fig 54 E - F	[5]Fig 56 E - F	[5]Fig 58 E - F	[5]Fig 60 E - F
[3]RSD [9]Reprod [4]ini (%)	13.274	33.560	24.602	27.851	28.801
[6]Q [9]Reprod	0.361 ([11]NA)	0.525 ([11]NA)	0.543 ([11]NA)	0.563 (80)	0.367 ([11]NA)
[7]Gs [9]Reprod	1.509 (80%)	1.592 (85%)	1.599 (85%)	1.501 (80%)	
[3]RSD [9]Reprod [8]end (%)	8.664	20.384	15.367	16.224	22.493
[10]Stab [1]Plot	[5]Fig 52 G - H	[5]Fig 54 G - H	[5]Fig 56 G - H	[5]Fig 58 G - H	[5]Fig 60 G - H
[10]Stab [12]ret [4] ini (%)	67.540	81.166	41.208	75.467	72.452
[3]RSD [10]Stab [4] ini (%)	13.686	7.297	32.252	9.414	11.186
[6]Q [10]Stab	0.748 (99%)	0.226 (NA)	0.408 (80%)	0.683 (99%)	0.414 (80%)
[7]Gs [10]Stab	2.383 (99%)	1.863 (80%)	2.012 (85%)	2.298 (95%)	2.032 (90%)
[10]Stab [12]ret [8]end (%)	89.226	84.788	54.218	90.666	81.7999
[3]RSD [10]Stab [8]end (%)	4.180	5.633	22.339	3.885	7.125

[1]Graphic, [2]Repeatability, [3]Relative Standard Deviation, [4]Initial Result, [5]Figure, [6]Q Dixon, [7]G Grubbs, [8]Final Result, [9]Reproducibility, [10]Stability,[11]Not Apply and [12]Retention.

23.275%. After applying the statistical tests, a reduction in data dispersion was observed for some analytes. For vanillin, the RSD decreased from 10.230% to 6.901%, while for tryptophan it was reduced from 23.275% to 15.146%, indicating that part of the initial variability was associated with outlying values. For tyrosine, the RSD was reduced to 6.395%, demonstrating an improvement in the precision of the measurements. For pyridoxine, the final RSD value was 10.907%, while for cysteine the statistical tests were not applicable, and the original experimental values were maintained.

Reproducibility, which evaluates the consistency of the method in independent measurements, initially showed RSD Reprod ini values between 13.274% and 33.560%, reflecting a greater dispersion among the electrochemical responses obtained in different measurements. After applying the Dixon and Grubbs tests, a reduction in these values was observed for some analytes, resulting in 8.664% for vanillin, 20.384% for tyrosine, 15.367% for tryptophan, and 12.224% for cysteine. For pyridoxine, the statistical tests were not applicable, and the original data set was maintained. This reduction in RSD values indicates that the exclusion of outlying measurements contributed to improving the statistical consistency of the results obtained.

The stability study was evaluated based on the initial signal retention stability

(Stab ret ini), which represents the percentage of the electrochemical response preserved over the sensor storage period. The initial values ranged from 41.208% to 81.166%, indicating that a significant fraction of the electrochemical response was maintained over time. The RSD Stab ini values ranged from 5.252% to 13.686%, demonstrating moderate variations among the measurements performed.

After the statistical treatment of the data, the final retention stability values (Stab ret end) were obtained, which showed an improvement in statistical consistency for some analytes. The final signal retention values were 89.226% for vanillin, 84.788% for tyrosine, 54.218% for tryptophan, 90.666% for cysteine, and 81.799% for pyridoxine. The corresponding final RSD values were 4.180%, 5.633%, 22.339%, 3.885%, and 7.125%, indicating that, after the removal of outliers, the data showed less dispersion and greater statistical reliability.

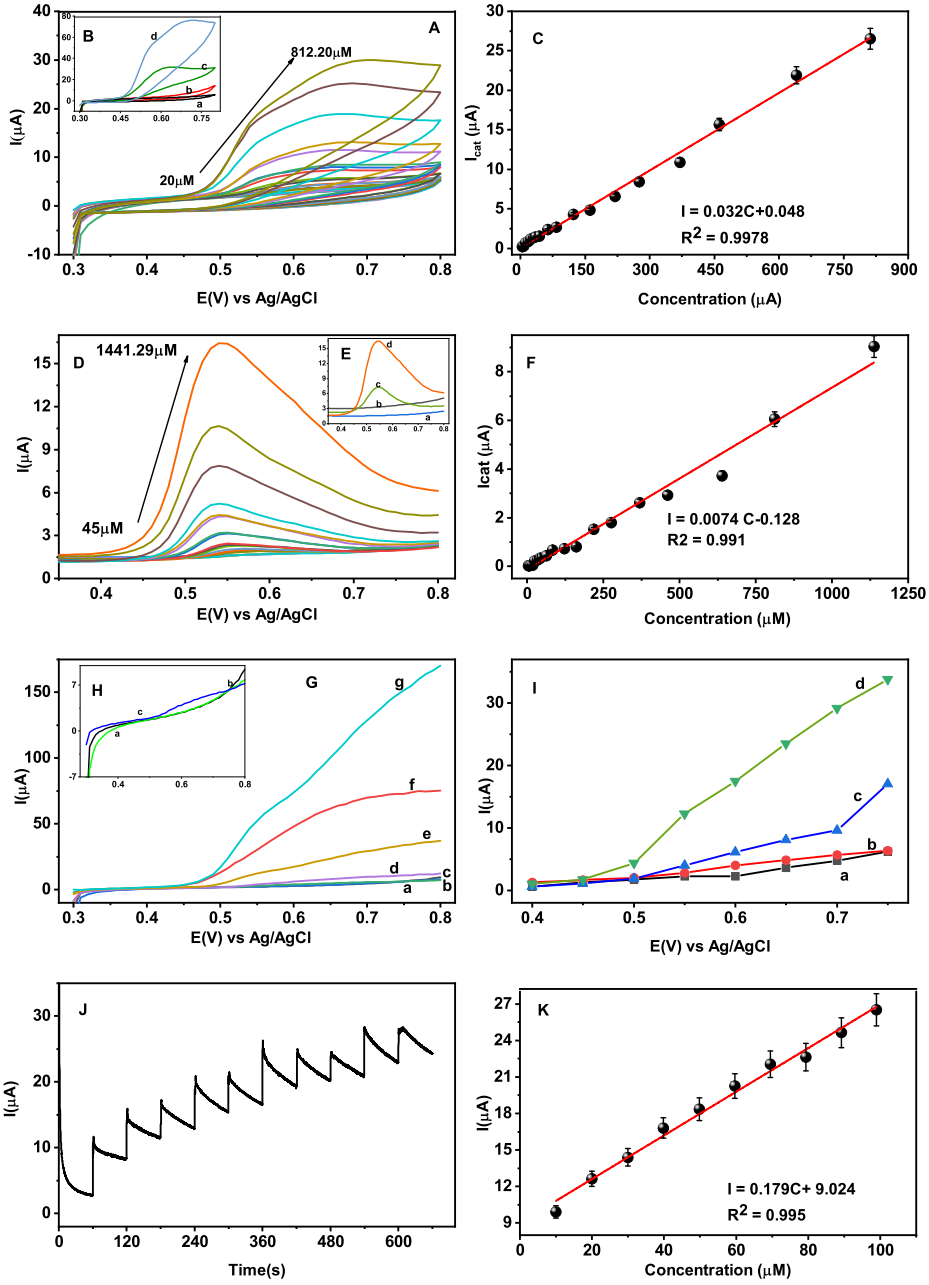


Figure 51 – Vanillin Detection: (A) CV; (B) CV: curve (a) referring to Bare0μM, curve (b) Mod 0μM, curve (c) Bare 812.20μM and curve (d) Mod 812.20μM; (C) CV test calibration curve; (D) DPV; (E) DPV: curve (a) referring to Bare 0μM, curve (b) Mod 0μM, curve (c) Bare 1441.29 μM and curve (d) Mod 1441.29 μM; (F) DPV test calibration curve; (G) LSV: curve (a) referring to Mod 0μM, curve (b) Bare 0 μM, curve (c) Mod 23.94μM, curve (d) 122.48μM, curve (e) Mod 461.65μM, curve (f) Bare 1441.28μM and curve (g) Mod 1441.28μM; (H) LSV reflecting curve (a) Mod 0μM, curve (b) Bare 0μM and curve (c) Mod 23.94μM; (I) LSV Summary: curve (a) referring to Mod 0μM, curve (b) Mod 23.94 μM, curve (c) Mod 122.48μM and curve (d) Mod 461.65μM; (J) Chronoamperometry; (K) Chronoamperometry test calibration curve.

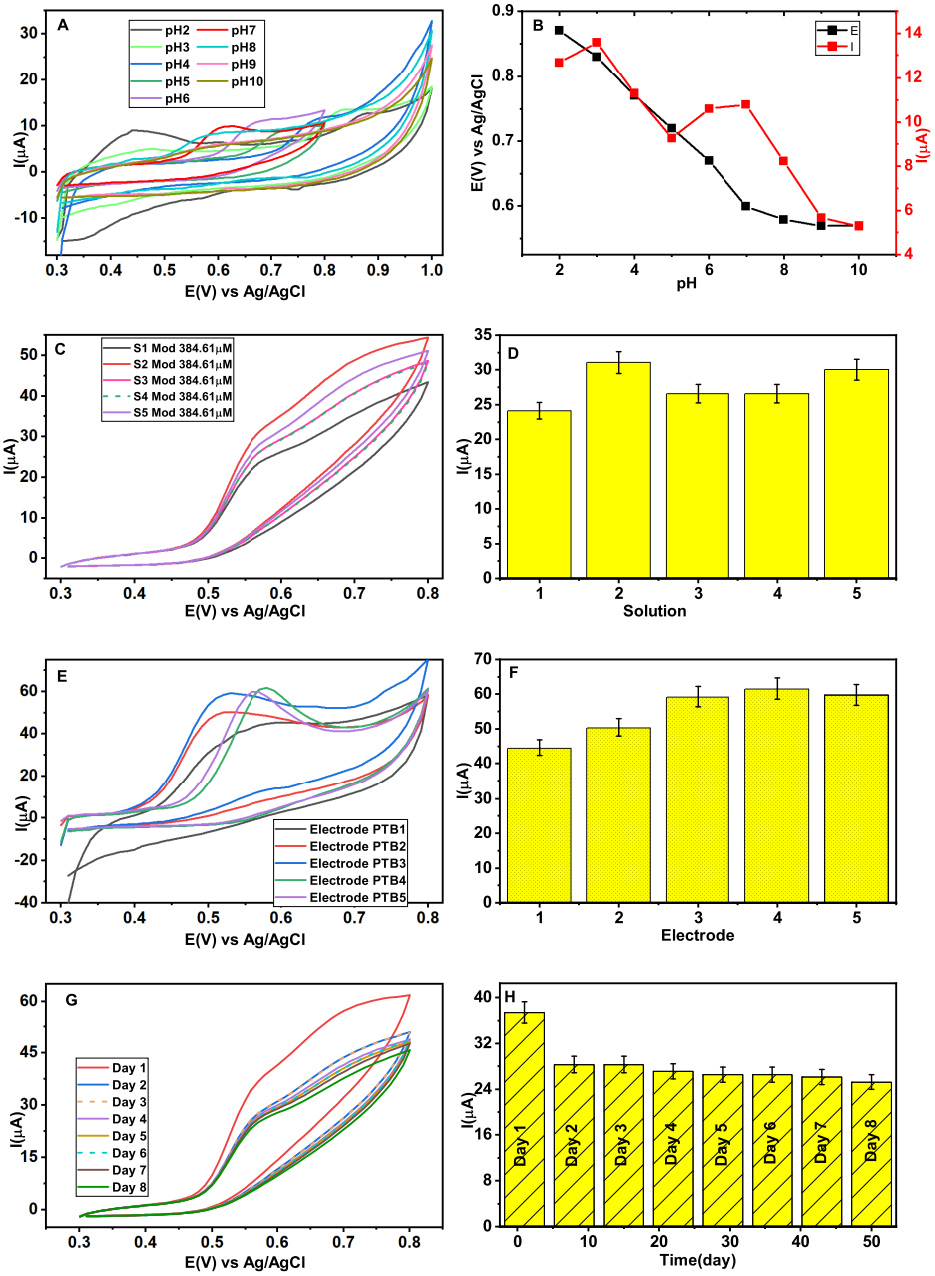


Figure 52 – Vanillin Validation: (A) pH; (B) pH Summary; (C) Repeatability; (D) Repeatability Summary; (E) Reproducibility; (F) Reproducibility Summary; (G) Stability; (H) Stability Summary.

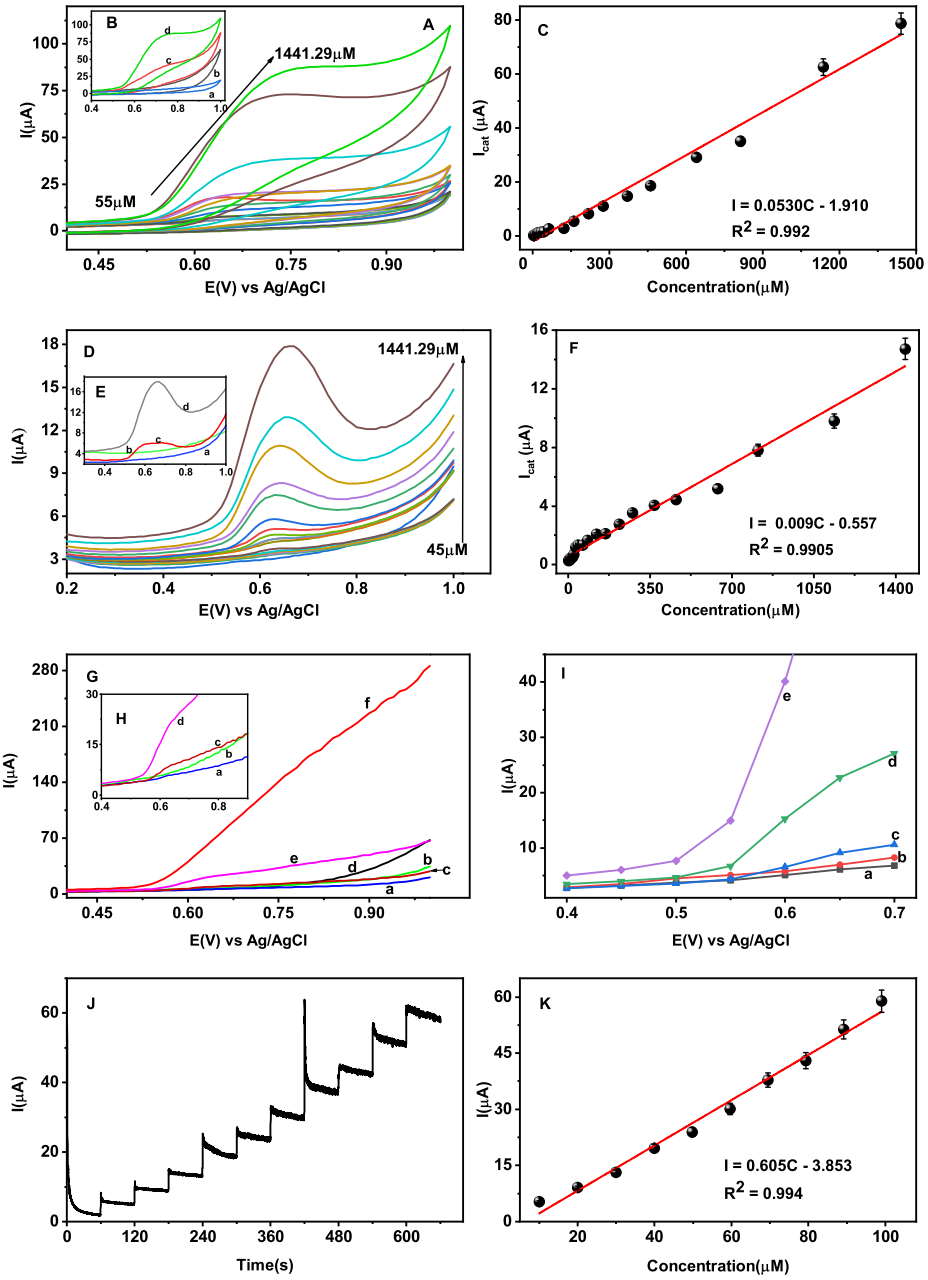


Figure 53 – Tyrosine Detection: (A) CV; (B) CV referring to curve (a) Bare 0μM, curve (b) Mod 0μM, curve (c) Bare 1441.29μM and curve (d) Mod 1441.29μM; (C) CV test calibration curve; (D) DPV; (E) DPV referring to curve (a) Bare 0μM, curve (b) Mod 0μM, curve (c) Bare 1441.29μM and curve (d) Mod 1441.29μM; (F) DPV test calibration curve; (G) LSV: curve (a) referring to Bare 0μM, curve (b) Mod 23.94μM, curve (c) Mod 122.48μM, curve (d) Mod 0μM, curve (e) Bare 1441.28μM and curve (f) Mod 1441.28μM; (H) LSV referring to curve (a) Bare 0μM, curve (b) Mod 0μM, curve (c) Bare 1441.28μM and curve (d) Mod 1441.28μM; (I) LSV Summary: curve (a) referring to Bare 0μM, curve (b) Mod 0μM, curve (c) Mod 122.48μM and curve (d) Mod 1441.28μM; (J) Chronoamperometry; (K) Chronoamperometry test calibration curve.

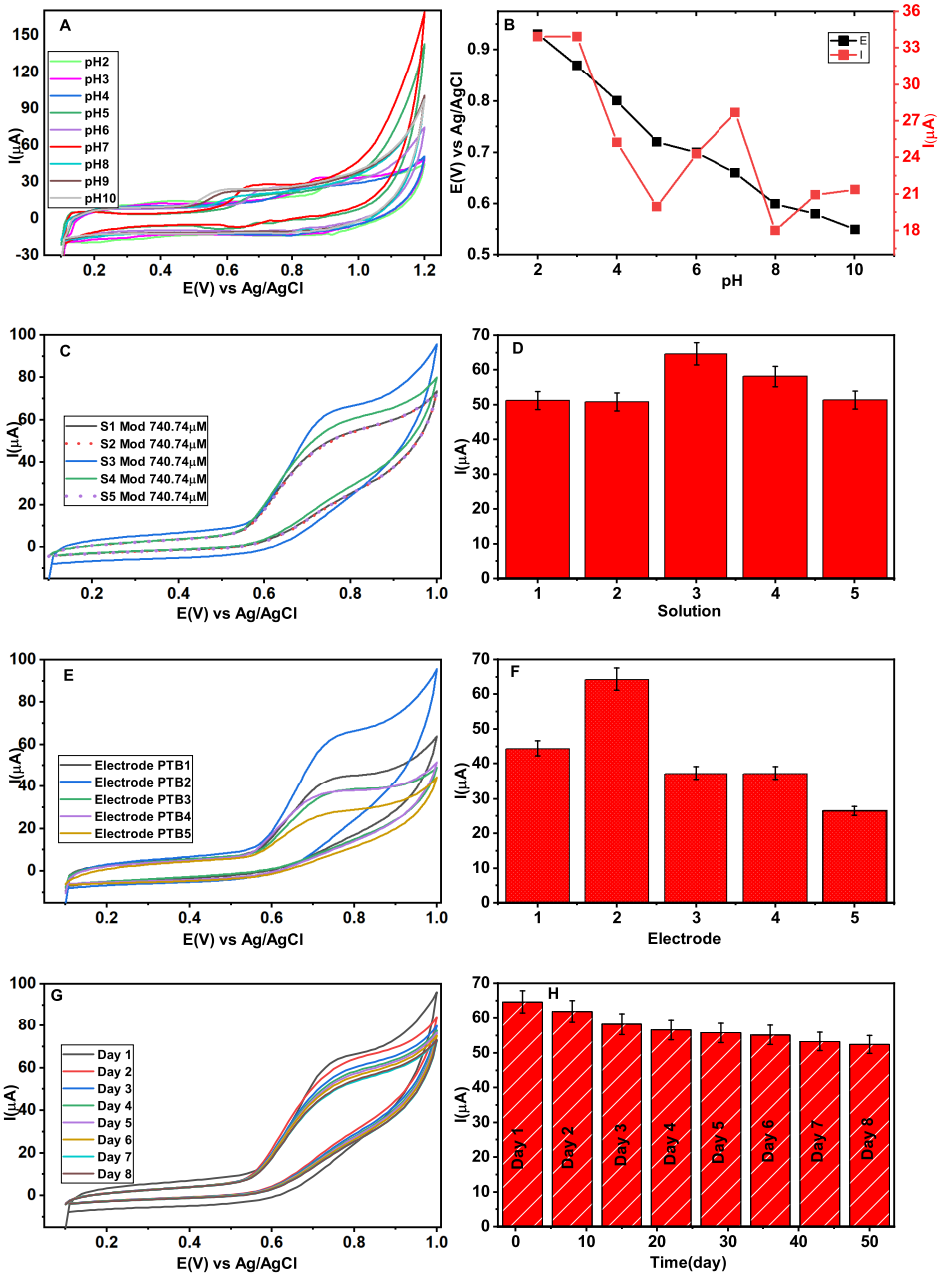


Figure 54 – Tyrosine Validation: (A) pH; (B) pH Summary; (C) Repeatability; (D) Repeatability Summary; (E) Reproducibility; (F) Reproducibility Summary; (G) Stability; (H) Stability Summary.

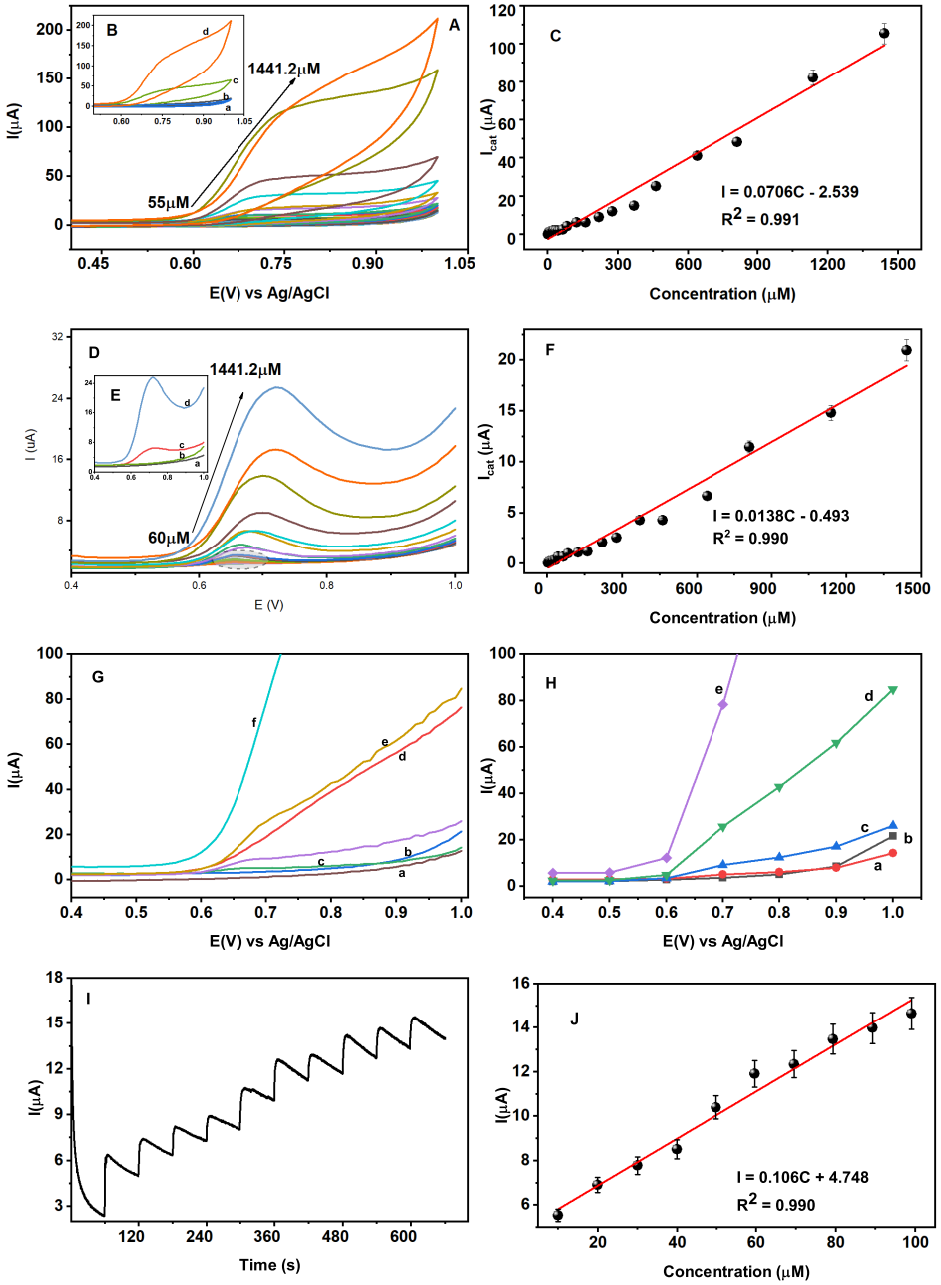


Figure 55 – Tryptophan Detection: (A) CV; (B) CV referring to curve (a) Bare 0μM, curve (b) Mod 0μM, curve (c) Bare 1441.28μM and curve (d) Mod 1441.28μM; (C) CV test calibration curve; (D) DPV; (E) DPV referring to curve (a) Bare 0μM, curve (b) Mod 0μM, curve (c) Bare 1441.28μM and curve (d) Mod 1441.28μM; (F) DPV test calibration curve; (G) LSV: referring to curve (a) Bare 0μM, curve (b) Mod 0μM, curve (c) Mod 23.94 μM, curve (d) Bare 1441.28μM, curve (e) Mod 461.65μM and curve (f) Mod 1441.28μM; (H) LSV Summary: referring to curve (a) Mod 0μM, curve (b) Bare 0μM, curve (c) Mod 23.94μM, curve (d) Bare 1441.28μM and curve (e) Mod 1441.28μM; (I) Chronoamperometry; (J) Chronoamperometry test calibration curve.

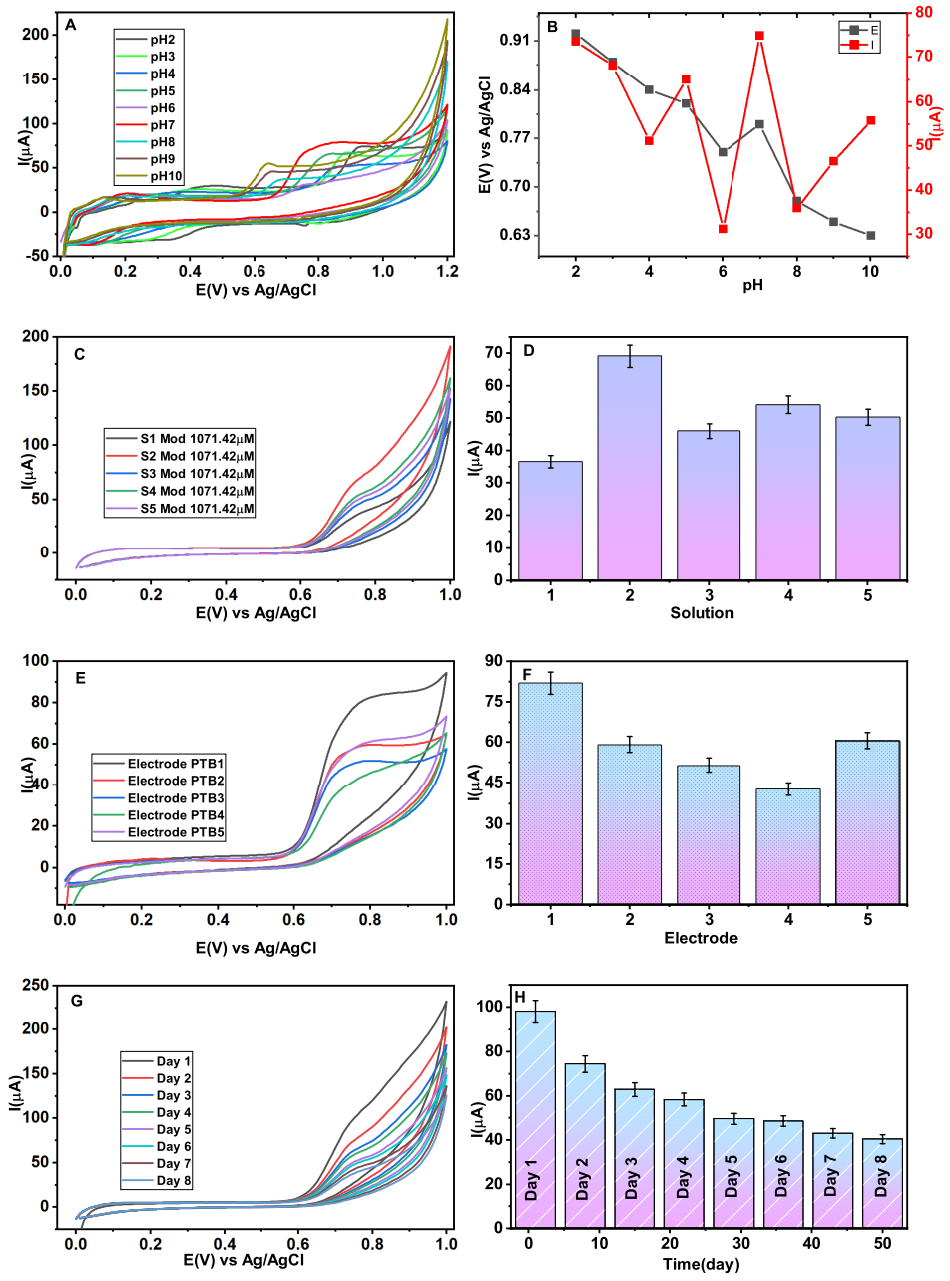


Figure 56 – Tryptophan Validation: (A) pH; (B) pH Summary; (C) Repeatability; (D) Repeatability Summary; (E) Reproducibility; (F) Reproducibility Summary; (G) Stability; (H) Stability Summary.

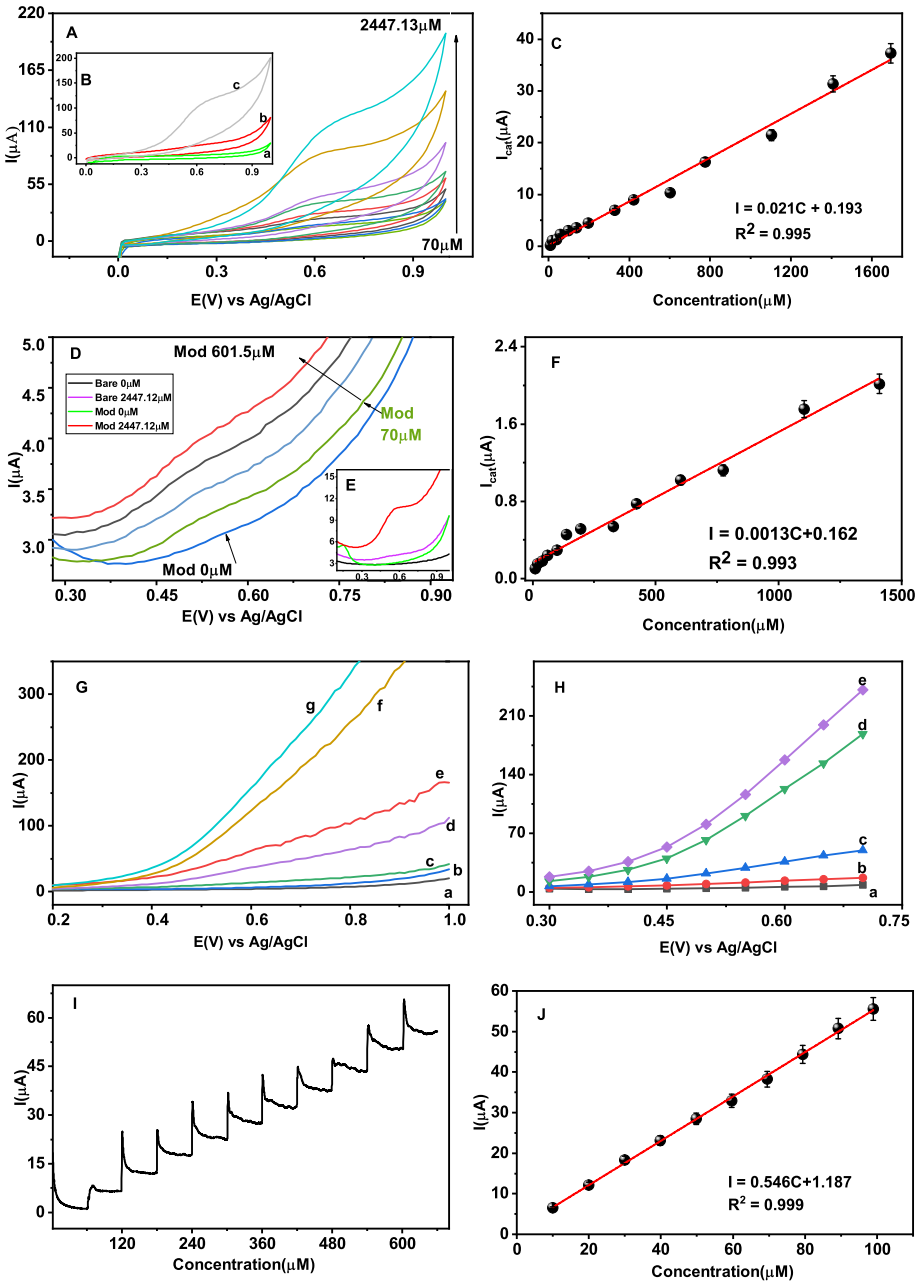


Figure 57 – Cysteine Detection: (A) CV; (B) CV referring to curve (a) Bare 0μM, curve (b) Mod 0μM and curve (c) Mod 2447.13μM; (C) CV test calibration curve; (D) DPV; (E) DPV zoom; (F) DPV test calibration curve; (G) LSV: referring to curve (a) Bare 0μM, curve (b) Mod 0μM, curve (c) Mod 138.06μM, curve (d) Mod 601.5μM, curve (e) Bare 2447.12μM, curve (f) Mod 2088.6μM and curve (g) Mod 2447.12μM; (H) LSV Summary: referring to curve (a) Bare 0μM, curve (b) Mod 0μM, curve (c) Mod 138.06μM, curve (d) 601.5μM and curve (e) Mod 2447.12μM; (I) Chronoamperometry; (J) Chronoamperometry test calibration curve.

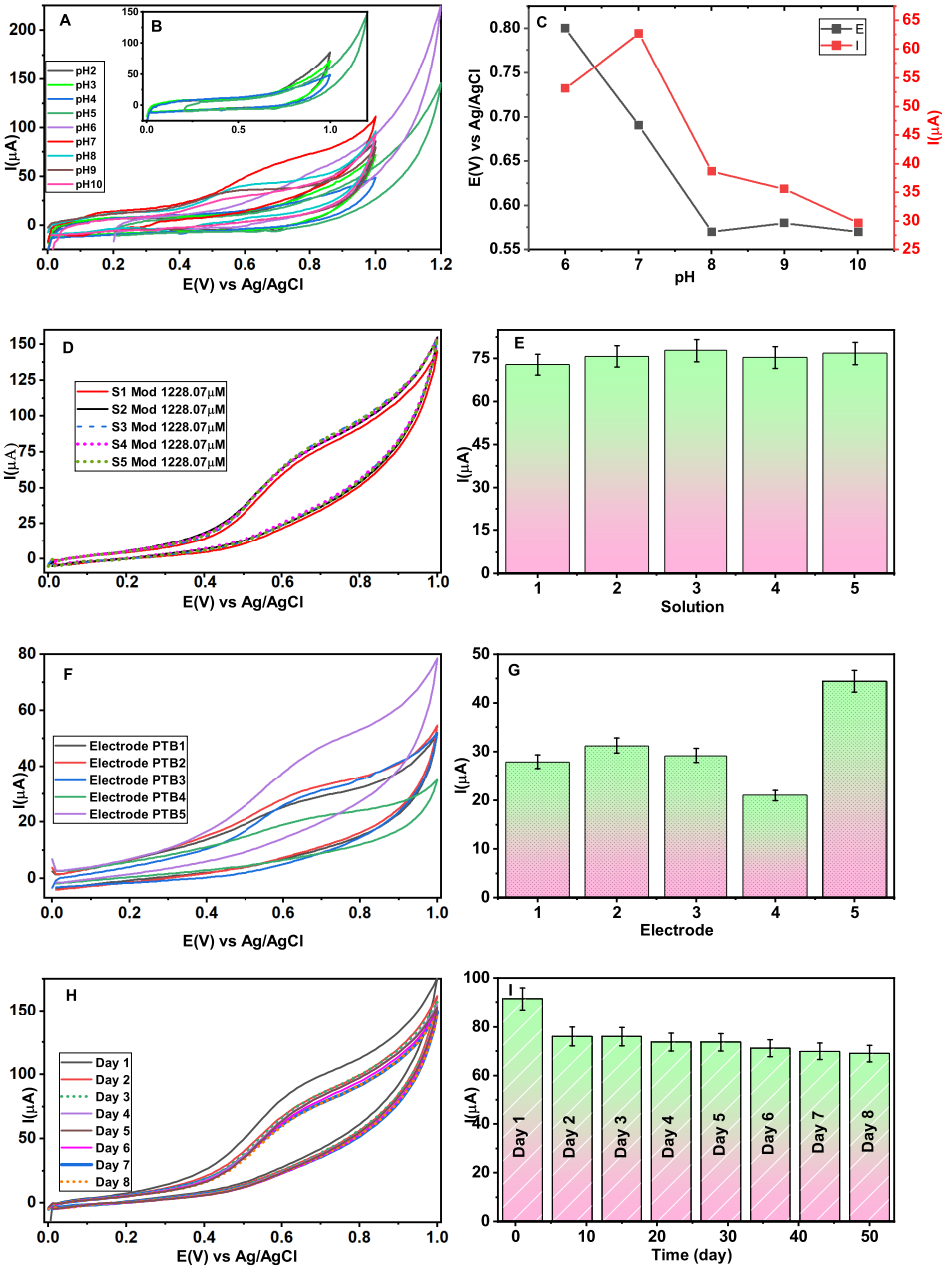


Figure 58 – Cysteine Validation: (A) pH 2 to pH 7; (B) pH 2 to pH 5; (C) pH Summary; (D) Repeatability; (E) Repeatability Summary; (F) Reproducibility; (G) Reproducibility Summary; (H) Stability; (I) Stability Summary.

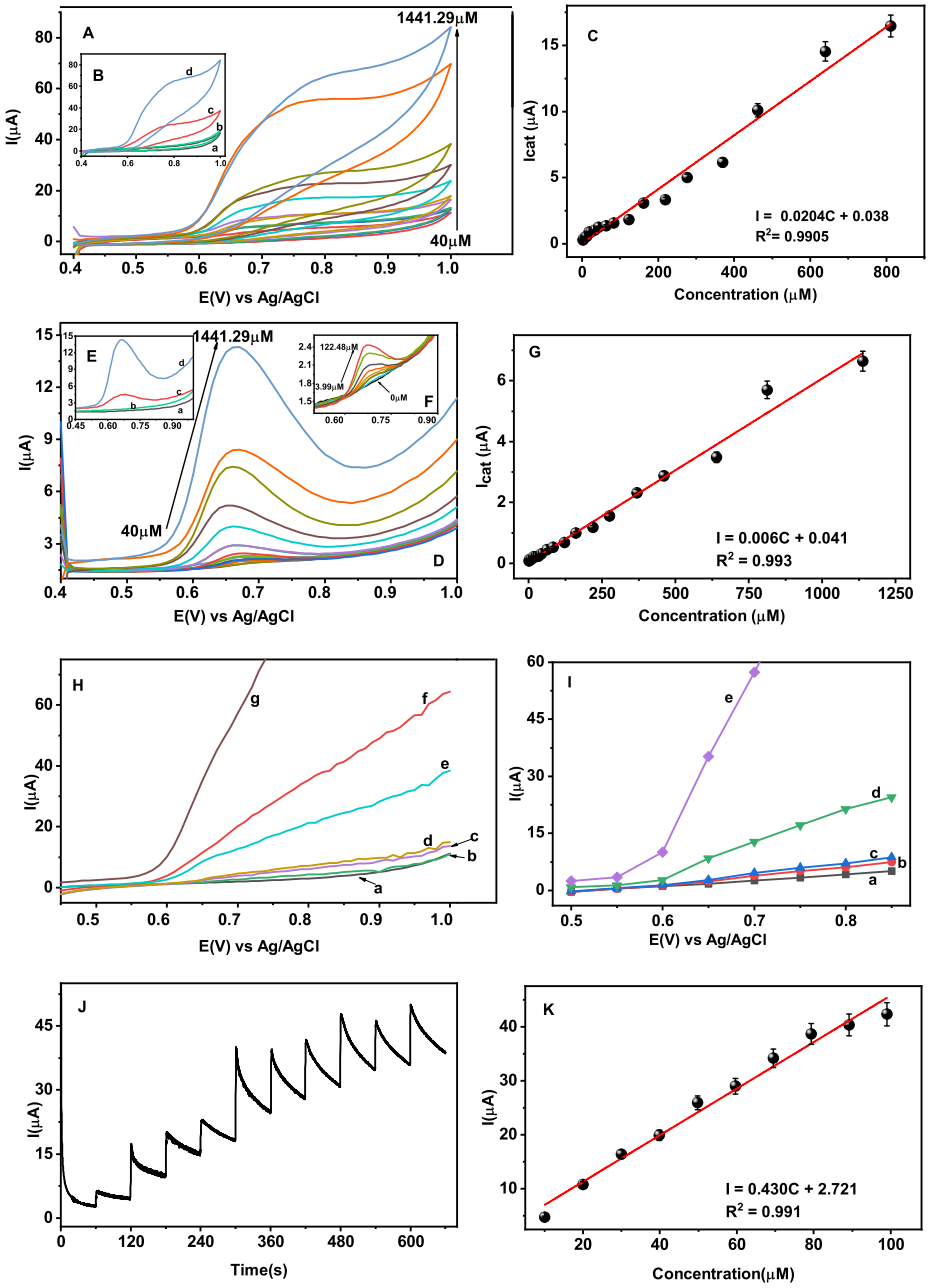


Figure 59 – Pyridoxine Detection: (A) CV; (B) CV referring to curve (a) Bare 0μM, curve (b) Mod 0μM, curve (c) Bare 1441.29μM and curve (d) Mod 1441.29μM; (C) CV test calibration curve; (D) DPV; (E) DPV referring to curve (a) Bare 0μM, curve (b) Mod 0μM, curve (c) Bare 1441.29μM and curve (d) Mod 1441.29μM; (F) DPV low concentrations; (G) DPV test calibration curve; (H) LSV: referring to curve (a) Bare 0μM, curve (b) Mod 0μM, curve (c) Mod 23.94μM, curve (d) Mod 122.48μM, curve (e) Mod 461.65μM, curve (f) Bare 1441.29μM and curve (g) Mod 1441.29μM; (I) LSV summary referring to: curve (a) Bare 0μM, curve (b) Mod 0μM, curve (c) Mod 122.48μM, curve (d) Mod 461.65μM and curve (e) Mod 1441.29μM; (J) Chronoamperometry; (I) Chronoamperometry test calibration curve.

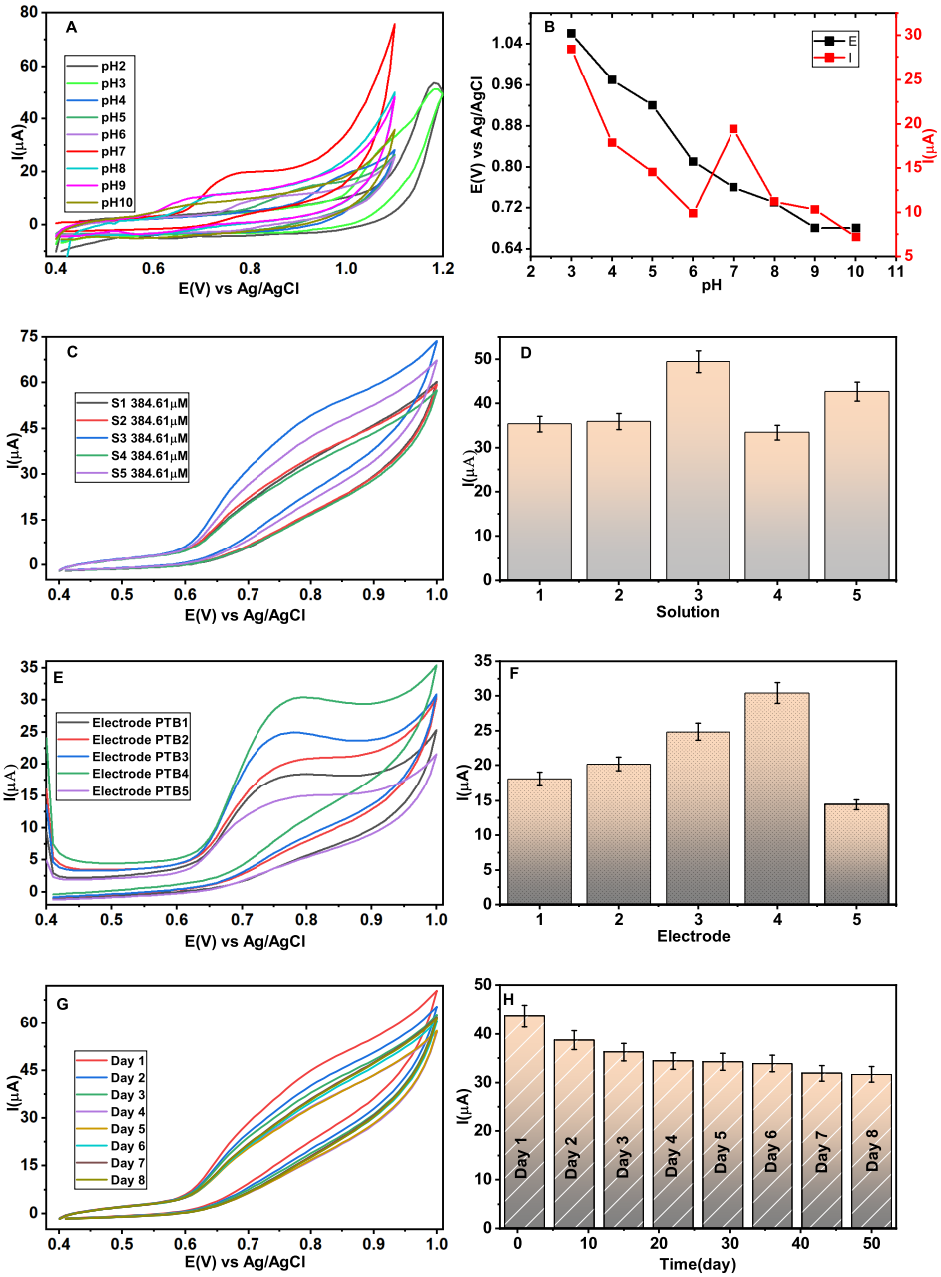


Figure 60 – Pyridoxine Validation: (A) pH; (B) pH Summary; (C) Repeatability; (D) Repeatability Summary; (E) Reproducibility; (F) Reproducibility Summary; (G) Stability; (H) Stability Summary.

PTB in its reduced form (PTB*red*) is electrochemically oxidized at the graphite electrode, losing electrons (e^-) that are transferred to the conducting substrate. This process generates the oxidized form of the mediator (PTB*ox*), which is electroactively more reactive. The oxidized form of PTB (PTB*ox*) reacts chemically with the analytes that are adsorbed on or near the surface of the polymer. During this reaction, the analyte is oxidized, releasing electrons (e^-) and protons (H^+), which are transferred to PTB*ox*. This process regenerates PTB to its reduced form (PTB*red*), allowing the catalytic cycle to continue. Figure 61 shows a diagram for a better visualization of this process.

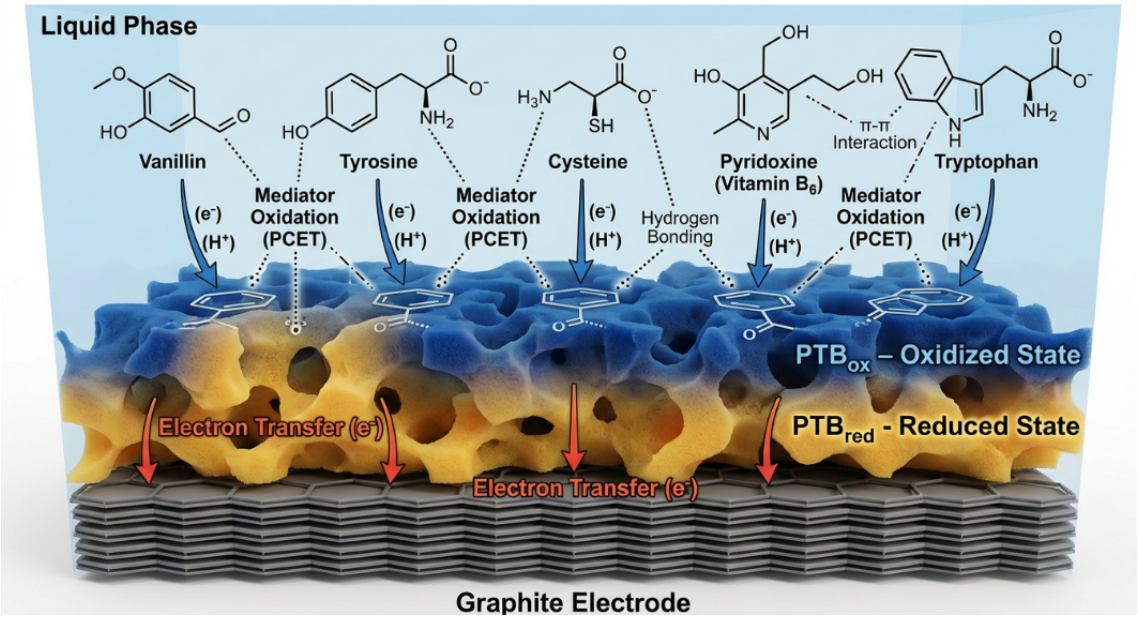


Figure 61 – PTB electrode analyte detection scheme. Figure produced by the author using artificial intelligence tools.

The PTB electrode exhibits a unique electrochemical behavior toward biological analytes such as amino acids and vitamins. The oxidation of tyrosine and tryptophan is a pH-dependent process that involves the transfer of two electrons and two protons ($2e^-/2H^+$). For tyrosine, the formation of the tyrosyl radical is the initial step, followed by the formation of dopaquinone or other condensation products. In tryptophan, oxidation of the indole ring occurs with the participation of protons to stabilize nitrogen-containing intermediates. Vanillin, which contains a phenolic group and an aldehyde, is oxidized preferentially at the hydroxyl group via a $2e^-/2H^+$ process, forming quinone-type derivatives. Cysteine undergoes an oxidation mechanism to cystine (dimer), which involves the transfer of one electron and one proton ($1e^-/1H^+$) per cysteine molecule, totaling $2e^-/2H^+$ in the formation of the disulfide bond. Pyridoxine (vitamin B6) exhibits an irreversible

oxidation in which the pH dependence suggests a mechanism of two electrons and one proton ($2e^-/1H^+$) or two electrons and two protons ($2e^-/2H^+$), depending on the pH range and the protonation state of the pyridine ring.

4.2.4 Simultaneous detection

Figure 62 demonstrates the ability of the modified electrodes to perform simultaneous detection of multiple analytes, highlighting the selectivity and electrochemical resolution provided by the electropolymerized films deposited on the graphite surface.

In Figure 62 A, the simultaneous detection of ascorbic acid (AA), uric acid (UA), guanine (G), adenine (A), and thymine (T) using the PBCB-modified electrode can be observed. The voltammogram reveals the presence of well-defined oxidation peaks at different potentials, corresponding to each of the analytes present in the solution. Ascorbic acid undergoes an oxidation process at lower potentials, followed by the oxidation of uric acid. At higher potentials, the peaks associated with the nitrogenous bases guanine, adenine, and thymine are observed. The clear separation between the electrochemical peaks demonstrates that the PBCB electrode has a high electrocatalytic resolution capacity, allowing the simultaneous identification of these species without significant signal overlap. This behavior is particularly relevant for biomedical applications.

Figure 62 B shows the simultaneous detection of catechol (CC), resorcinol (RS), and hydroquinone (HQ) using the PBP-modified electrode. These three compounds belong to the class of dihydroxybenzenes and share the same molecular formula (C H O), differing only in the relative positions of the hydroxyl groups on the aromatic ring. Catechol corresponds to the ortho isomer (1,2-dihydroxybenzene), resorcinol to the meta isomer (1,3-dihydroxybenzene), and hydroquinone to the para isomer (1,4-dihydroxybenzene). Despite having identical chemical compositions, these structural differences result in distinct electrochemical properties, reflected in the different oxidation potentials observed in the voltammogram. The modified electrode was able to clearly discriminate among these three isomers, showing well-separated peaks for each species.

In Figure 62 C, the simultaneous detection of pyrogallol (PG) and hydrazine (HZ) using the PBP-modified electrode is also presented. It can be observed that both analytes display well-defined oxidation peaks at distinct potentials, allowing their simultaneous identification without significant interference between the signals. Pyrogallol exhibits

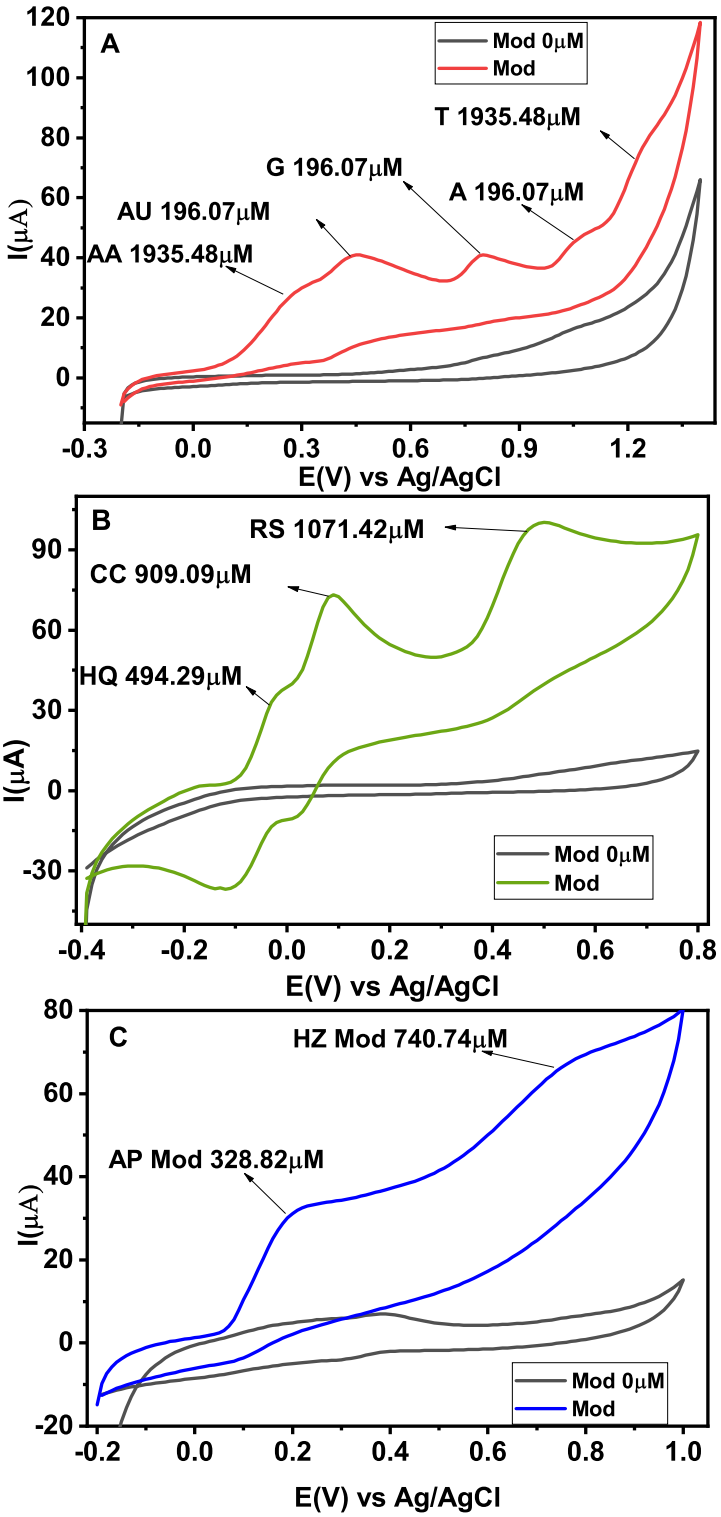


Figure 62 – Simultaneous analyte detection: (A) PBCB electrode for the detection of AA, AU, G, A and T; (B) PBP electrode for the detection of CC, RS and HQ; and (C) PBP electrode for the detection of AP and HZ.

oxidation at lower potentials, whereas hydrazine is oxidized at higher potentials, which enables a clear separation of the electrochemical processes.

4.2.5 Real samples

To evaluate the applicability of the PBP electrode in real environmental matrices, three different types of water samples were analyzed, selected to represent different environmental conditions and levels of contamination. The samples used were: freshwater from a lagoon shown in Figure 63A, theoretically unpolluted; brackish water, potentially contaminated, shown in Figure 63C; and polluted freshwater from a river shown in Figure 63E.

The first sample corresponded to water from a lagoon located in a residential neighborhood in Volta Redonda, in the interior of the state of Rio de Janeiro. This lagoon has predominantly fresh water and is theoretically considered to have a low level of anthropogenic contamination, being used as a relatively clean environmental matrix to assess the sensor's response under near-natural conditions. The second sample consisted of water from the Rodrigo de Freitas Lagoon, located in the city of Rio de Janeiro, characterized as a brackish environment resulting from the mixing of freshwater and seawater. This type of environment exhibits greater chemical complexity due to the simultaneous presence of dissolved salts, organic matter, and possible contaminants from urban activities, and is classified as a potentially polluted system.

The third sample corresponded to polluted fresh water collected from the Paraíba do Sul River, an important watercourse in the southeastern region of Brazil, also in the Volta Redonda area, which is heavily influenced by industrial, agricultural, and urban activities along its watershed. This sample was chosen with the aim of evaluating the sensor's performance in a more complex environmental matrix, containing a variety of potentially interfering chemical species. The pH of these samples was measured and did not show large variations around pH 7 (as shown in Figures 63 B, D, and F).

Finally, Figure G shows the simultaneous detection of pyrogallol and hydrazine in river water, demonstrating the electrode's ability to identify multiple analytes in a single electrochemical analysis. Two distinct voltammetric signals can be observed, corresponding to the characteristic oxidation potentials of each compound: pyrogallol exhibits a detection peak at 0.15 V and hydrazine at 0.75 V, enabling their differentiation in the

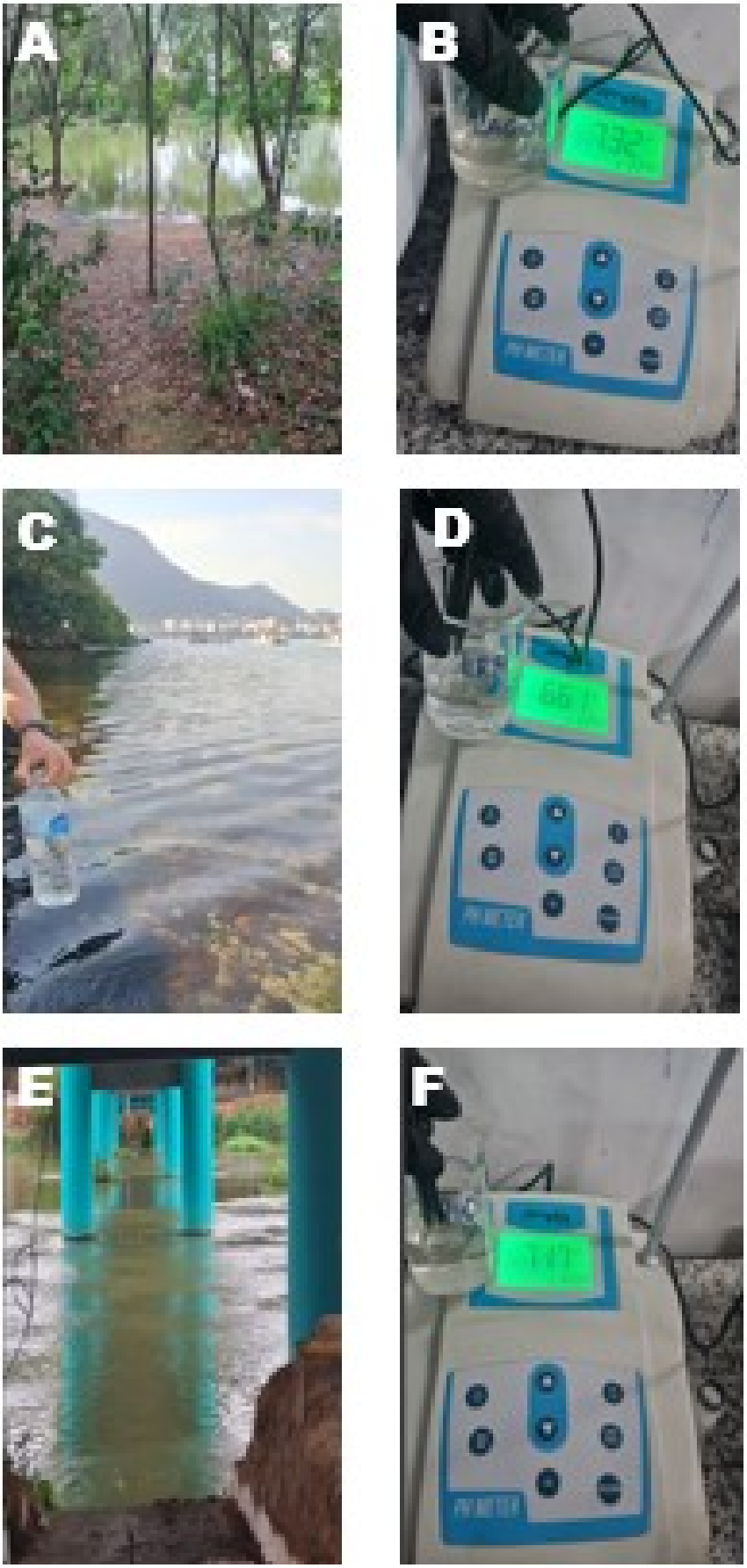


Figure 63 – Detection of real samples: (A) Lagoon in a residential neighborhood in Volta Redonda - RJ; (B) pH 7.32 of the lagoon water; (C) Rodrigo de Freitas Lagoon - Rio de Janeiro; (D) pH 6.61 of the Rodrigo de Freitas Lagoon water; (E) Paraíba do Sul River in Volta Redonda and (F) pH of the Paraíba do Sul River water.

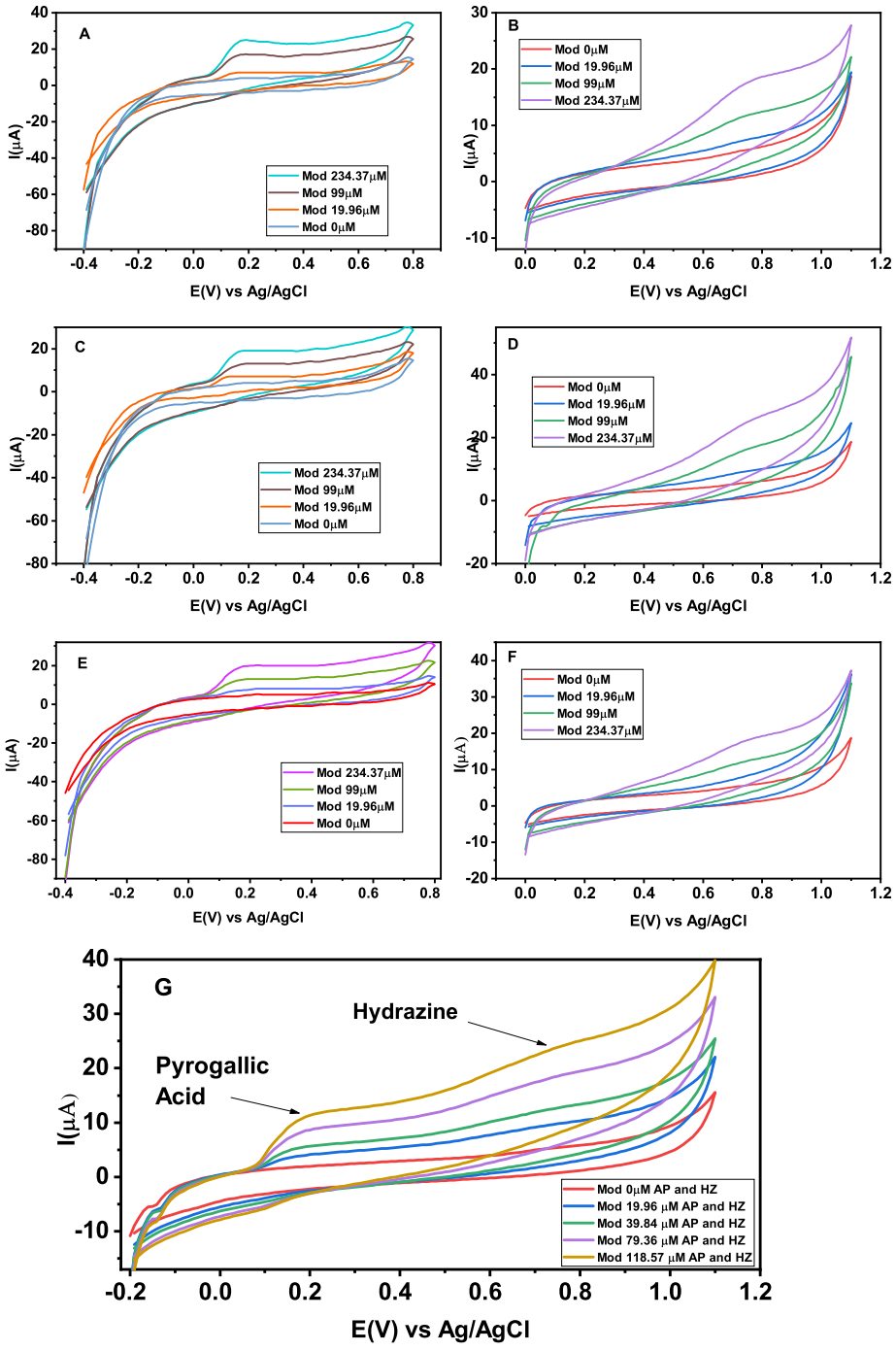


Figure 64 – Detection of real samples: (A) AP in river water; (B) HZ in CV river water; (C) AP in Rodrigo de Freitas lagoon water; (D) HZ in Rodrigo de Freitas lagoon water; (E) AP in lagoon water; (F) HZ in lagoon water; (G) AP and HZ in river water.

same matrix. The peak associated with pyrogallol appears at lower potentials, whereas the hydrazine signal occurs at more positive potentials, which facilitates discrimination between the analyzed species.

Figure 65 shows the tests carried out through cyclic voltammetry studies for each analyte individually, aiming to verify their characteristic oxidation potentials on the modified electrode surface. These tests were performed using a complex matrix of real human urine samples. As observed in Figures 65 (A) to (E), all analytes exhibited distinct anodic oxidation peaks, with current intensities proportional to the increase in their respective concentrations.

Figures 65 (F) and (G) show the voltammograms obtained for the analysis of pure urine, without external addition of uric acid, using the PBCB electrode. A characteristic voltammetric signal can be observed in the potential region associated with the oxidation of uric acid, even in the absence of standard additions of the analyte. This result indicates that the sensor was able to directly detect the uric acid naturally present in the urine sample, demonstrating the occurrence of an oxidation peak corresponding to the analyte.

Figure 65 (G), which presents an enlargement of the potential region where the oxidation process occurs, allows a clearer visualization of the voltammetric peak associated with uric acid. The presence of this signal confirms that the analyzed biological matrix contains detectable concentrations of the analyte, which is consistent with the fact that uric acid is a metabolite naturally present in human urine, resulting from purine metabolism. The simultaneous analytical evaluation is presented in Figure 65 (H), which illustrates the simultaneous detection of five analytes: ascorbic acid (AA), uric acid (UA), guanine (G), adenine (A), and thymine (T) at potentials of 1.00, 0.38, 0.75, 1.05, and 1.30 V. The electrochemical separation achieved by the PBCB electrode is remarkable, with five oxidation peaks clearly resolved in the same voltammogram.

In all the complex matrices analyzed with the analytes, the detection peaks remained at the same values (or very close) as the values assessed through the controlled tests with PBS.

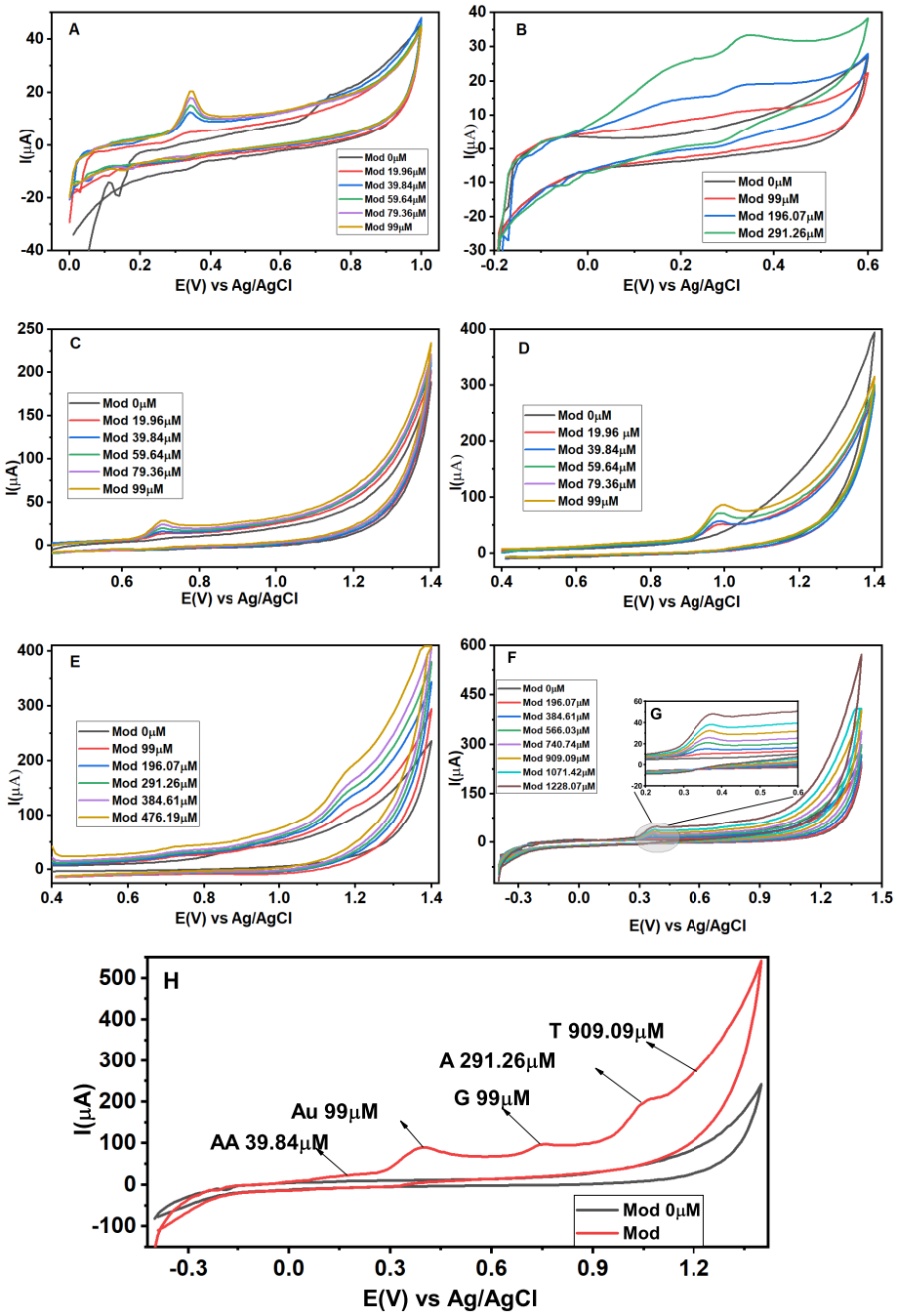


Figure 65 – Detection of real samples (Urine): (A) CV AU; (B) CV AA; (C) CV guanine; (D) CV adenine; (E) CV thymine; (F) Urine without analyte; (G) Amplification of the detection peak of urine without analyte; (H) Simultaneous detection of analytes detected by the PCBC electrode.

4.2.6 Comparison with the literature

The comparison of the limits of detection (LD) of the analytes studied with the values reported in the literature reveals that the evaluated analytes exhibit low LD values, indicating high sensitivity of the applied methods. This finding is in line with the trend observed in several modern analytical techniques, especially in electrochemical methods, which have been continuously improving their ability to detect very low concentrations of target substances. This result can be largely attributed to the efficiency of the electrode surface modification strategy through the electropolymerization of dyes, which contributes to increasing the electroactive area, favors electron transfer, and enhances the electrochemical response of the analytes.

Table 12 – Comparison of analyte detection results with the literature.

Analytes	Technique	RangeμM	LD μM	Electrode/Modified	Ref
Guanine	CV	20 - 3100	18.2	[1]GCE/[2]PNF	[107]
Guanine	CV	4 - 160	3.816	Graphite/PBCB	This work
Adenine	CV	10 - 18600	8.6	[1]GCE/[2]PNF	[107]
Adenine	CA	9.99 - 99	5.757	Graphite/PBCB	This work
Thymine	CV	20 - 11210	19.4	[1]GCE/[2]PNF	[107]
Thymine	CV	10 - 375.35	0.251	Graphite/PBCB	This work
Uric acid	LSV	2 - 200	0.29	[1]GCE/FeO	[108]
Uric acid	CV	7.9 - 1010.42	0.204	Graphite/PBCB	This work
Ascorbic acid	CV	10 - 10550	0.569	[3]CP/CuO	[109]
Ascorbic acid	CV	9.99 - 12258.74	0.168	Graphite/PBCB	This work
Catechol	CA	0.02 - 2500	15.2	[1]GCE/Cu-[4]PPy	[110]
Catechol	CA	9.99 - 99	1.895	Graphite/PBP	This work
Resorcinol	DPV	15.6 - 500	15.6	[1]GCE/ [5]PTA	[111]
Resorcinol	CA	9.99 - 99	5.073	Graphite/PBP	This work
Hydroquinone	DPV	7.81 - 500	7.81	[1]GCE/[5]PTA	[111]
Hydroquinone	CA	9.99 - 99	4.223	Graphite/PBP	This work
Hydrazine	CA	5 - 64	7.38	[1]GCE/[6]FePTZ	[112]
Hydrazine	DPV	19.96 - 942.02	7.499	Graphite/PBP	This work
Pyrogálic acid	CV	8 - 30	6.2	[7]CPE/[8]L-Arg	[113]
Pyrogálic acid	DPV	1.99 - 1323.93	0.83	Graphite/PBP	This work
Vanillin	CV	20 - 120	120	Graphite/Mm/Zn/V	[114]
Vanillin	CA	9.99 - 99	7.188	Graphite/PTB	This work
Tyrosine	CV	10 - 600	7	Graphite/[9]EuHCF	[115]
Tyrosine	CA	9.99 - 99	7.631	Graphite/PTB	This work
Tryptophan	LSV	31.26 - 1000	10.41	[10]CNT/[11]PLA	[116]
Tryptophan	CA	9.99 - 99	9.861	Graphite/PTB	This work
Cysteine	CA	11.6 - 500	3.5	[7]CPE/Cu(II)	[117]
Cysteine	CA	9.99 - 99	2.524	Graphite/PTB	This work
Pyridoxine	DPV	8.88 - 1000	32.12	[3]CPE/[12]CUNs	[118]
Pyridoxine	CA	9.99 - 99	9.312	Graphite/PTB	This work

[1]Glassy Carbon Electrode, [2]Poly(New Fushsin,[3]Carbon Paper , [4]Polypyrrole, [5]Poly Thiophenemalonic Acid, [6]Pirazinelitanotrol, [7]Carbon Paste Electrode, [8]L-Arginine, [9]Europium Hexacyanoferrate, [10]Carbon nanotube, [11]polylactic acid and [12]copper nanoparticle.

Conclusions

This work presented a comprehensive investigation of electropolymerized electrodes and their application in the electroanalytical detection of multiple bioactive and environmentally relevant analytes. The study integrated different electrochemical techniques, including cyclic voltammetry (CV), differential pulse voltammetry (DPV), linear sweep voltammetry (LSV), and chronoamperometry (CA), providing a detailed understanding of the electrochemical behavior, sensitivity, and analytical performance of the developed system.

The comparative analysis of the electroanalytical techniques demonstrated that all methods were effective for the identification and quantification of the studied species. However, cyclic voltammetry stood out as the most sensitive technique, presenting higher current responses and lower limits of detection for most analytes. This superior performance is associated with its ability to probe both kinetic and diffusion-controlled processes, allowing a more complete characterization of the electrode/analyte interface.

The calibration curves obtained for all analytes exhibited excellent linearity, with determination coefficients (R^2) close to 0.99, confirming a strong correlation between peak current and analyte concentration. This linear behavior indicates that the electrochemical response is governed by predictable charge-transfer processes, enabling reliable and reproducible quantitative analysis within the studied concentration ranges.

A key finding of this work is the significant enhancement of electrochemical signals observed for the modified electrodes when compared to the unmodified surface. The electropolymerized film promotes a clear electrocatalytic effect, reflected by increased peak currents and improved signal definition. This behavior can be attributed to a combination of factors, including increased electroactive surface area, improved electron-transfer kinetics, and specific interactions between the polymeric matrix and the analyte molecules. Importantly, the redox potentials remained essentially unchanged after modification, indicating that the electrode surface modification enhances the analytical signal without altering the fundamental electrochemical mechanisms.

Chronoamperometric measurements revealed fast response times on the order of seconds, indicating rapid electron-transfer kinetics and efficient mass transport of analytes

toward the electrode surface. These results demonstrate that the polymeric film does not act as a diffusion barrier, but rather facilitates the electrochemical process, making the system suitable for rapid analyses and real-time monitoring applications.

The electroanalytical performance was found to be dependent on the chemical structure and physicochemical properties of the analytes, highlighting the role of molecular interactions in the sensing mechanism. Despite these variations, the developed system showed high versatility, enabling the detection of multiple analytes with good sensitivity and resolution, even in complex mixtures.

The validation of the electrochemical method confirmed the robustness and reliability of the proposed system. Statistical treatment of the data using Dixon (Q) and Grubbs (G) tests allowed the identification and removal of outliers, resulting in improved data consistency and reduced relative standard deviation (RSD) values. After this treatment, RSD values were predominantly below 10%, indicating satisfactory repeatability and reproducibility, even under conditions involving modified electrodes and complex sample matrices.

Furthermore, stability studies demonstrated that the electropolymerized electrodes maintain a high percentage of signal retention over time, confirming the structural integrity and durability of the polymeric film. The observed stability, combined with low variability after statistical correction, indicates that the system is not only reliable but also suitable for long-term analytical applications.

The practical applicability of the developed electrodes was successfully demonstrated in both environmental and biological samples. In environmental matrices, including river and brackish water, the sensor enabled the simultaneous detection of analytes such as hydrazine and pyrogallol, with well-defined and separated oxidation peaks, even in the presence of interfering species. This demonstrates the selectivity and robustness of the system in real-world conditions.

In biological samples, particularly human urine, the electrode exhibited excellent analytical performance. The system allowed accurate quantification through standard addition methods and was sensitive enough to detect endogenous species such as uric acid without the need for sample fortification. A particularly relevant result was the simultaneous detection of multiple biomolecules, including ascorbic acid, uric acid, guanine, adenine, and thymine, within a single electrochemical scan. This highlights the high resolution, selectivity, and multiplexing capability of the proposed sensor.

Taken together, the results demonstrate that the electropolymerized electrodes developed in this work combine high sensitivity, low detection limits, fast response, good reproducibility, and long-term stability. In addition, the use of low-cost materials and relatively simple fabrication procedures reinforces the practical viability of the system. The effectiveness of the surface modification strategy was clearly demonstrated, providing an efficient approach for enhancing electrochemical performance without increasing system complexity.

Finally, the findings of this work contribute to the advancement of electrochemical sensing technologies, particularly in the development of versatile, low-cost, and high-performance sensors. The results open perspectives for future applications in environmental monitoring, clinical diagnostics, and the detection of bioactive compounds, as well as for further optimization of polymer-based electrochemical interfaces.

4.3- Future Perspectives

Based on the results obtained in this work, several opportunities for further development and optimization of the proposed electrochemical system can be identified.

Firstly, the exploration of alternative electropolymerized materials and composite systems represents a promising pathway to enhance sensitivity, selectivity, and stability. The incorporation of nanostructured materials, such as metallic nanoparticles, graphene derivatives, or carbon nanotubes, into the polymeric matrix may significantly improve electron-transfer kinetics and increase the electroactive surface area, leading to superior analytical performance.

In addition, further investigations into the fundamental mechanisms governing the interaction between the polymeric film and different analytes would provide deeper insights into the sensing process. Studies involving spectroelectrochemical techniques and advanced surface characterization methods could help elucidate adsorption phenomena, charge-transfer pathways, and molecular recognition effects.

Another important perspective involves the miniaturization and integration of the developed electrodes into portable and automated sensing platforms. The development of screen-printed electrodes or microfabricated devices could enable the transition from laboratory-scale experiments to real-world applications, particularly in environmental monitoring and point-of-care diagnostics.

The expansion of the analytical scope to include a broader range of bioactive, pharmaceutical, and environmental compounds is also of great interest. The ability of the system to perform simultaneous multi-analyte detection suggests strong potential for applications in complex matrices, such as biological fluids and industrial effluents.

Moreover, long-term stability studies under different storage and operational conditions, as well as interference studies involving a wider range of coexisting species, would further validate the robustness and applicability of the sensor in practical scenarios.

Finally, the integration of the electrochemical system with data processing tools, including chemometric analysis and machine learning approaches, could enhance signal interpretation, improve selectivity, and enable the development of intelligent sensing platforms.

These perspectives highlight the potential for advancing the developed system toward more efficient, selective, and application-oriented electrochemical sensors, reinforcing its relevance for future research in analytical chemistry and sensor technology.

Bibliography

[1] LM da C SILVA. “Desenvolvimento de biossensores eletroquímicos para fenol e uréia com foco na aplicação ambiental”. In: Universidade Federal do Rio de Janeiro. Rio de Janeiro (2011), p. 154.

[2] Sima Das. “Applications of sensor technology in healthcare”. In: Revolutionizing Healthcare Treatment With Sensor Technology. IGI Global Scientific Publishing, 2024, pp. 79–99.

[3] Md Najmul Mowla et al. “Internet of Things and wireless sensor networks for smart agriculture applications: A survey”. In: IEEe Access 11 (2023), pp. 145813–145852.

[4] Kanaiya Bhatt, Chetan Agrawal, and Anil M Bisen. “A review on emerging applications of IoT and sensor technology for industry 4.0”. In: Wireless Personal Communications 134.4 (2024), pp. 2371–2389.

[5] Manickam Ramesh et al. “Nanotechnology-enabled biosensors: A review of fundamentals, design principles, materials, and applications”. In: Biosensors 13.1 (2022), p. 40.

[6] Leland C Clark and Champ Lyons. “Electrode systems for continuous monitoring in cardiovascular surgery”. In: Annals of the New York Academy of sciences 102.1 (1962), pp. 29–45.

[7] Seán Barry and Alan O’Riordan. “Electrochemical nanosensors: Advances and applications”. In: Reports in Electrochemistry (2016), pp. 1–14.

[8] Dr. Bhagwati Patel, Professor G Sinha, and Naveen Goel. “Introduction to sensors”. In: Nov. 2020. ISBN: 978-0-7503-2707-7. DOI: 10.1088/978-0-7503-2707-7ch1.

[9] Dorothee Grieshaber et al. “Electrochemical biosensors-sensor principles and architectures”. In: Sensors 8.3 (2008), pp. 1400–1458.

[10] Xiaoping Huang, Yufang Zhu, and Ehsan Kianfar. “Nano biosensors: properties, applications and electrochemical techniques”. In: Journal of Materials Research and Technology 12 (2021), pp. 1649–1672.

[11] Koh Sing Ngai et al. “A review of polymer electrolytes: fundamental, approaches and applications”. In: Ionics 22 (2016), pp. 1259–1279.

[12] Arkady A Karyakin, Elena E Karyakina, and Hanns-Ludwig Schmidt. “Electropolymerized azines: a new group of electroactive polymers”. In: Electroanalysis: An International Journal Devoted to Fundamental and Practical Aspects of Electroanalysis 11.3 (1999), pp. 149–155.

[13] Dilek Kul, Rasa Pauliukaite, and Christopher MA Brett. “Electrosynthesis and characterisation of poly (Nile blue) films”. In: Journal of electroanalytical chemistry 662.2 (2011), pp. 328–333.

[14] Jai-Pil Choi and Allen J Bard. “Electrogenerated chemiluminescence 73: acid–base properties, electrochemistry, and electrogenerated chemiluminescence of neutral red in acetonitrile”. In: Journal of Electroanalytical Chemistry 573.2 (2004), pp. 215–225.

[15] Madalina M Barsan, Edilson M Pinto, and Christopher MA Brett. “Methylene blue and neutral red electropolymerisation on AuQCM and on modified AuQCM electrodes: an electrochemical and gravimetric study”. In: Physical Chemistry Chemical Physics 13.12 (2011), pp. 5462–5471.

[16] R Yang, C Ruan, and J Deng. “A H2O2 biosensor based on immobilization of horseradish peroxidase in electropolymerized methylene green film on GCE”. In: Journal of applied electrochemistry 28 (1998), pp. 1269–1275.

[17] Li Xia et al. “Electropolymerization of brilliant cresyl blue on carbon ionic liquid electrode and electrocatalytic application for the voltammetric determination of ascorbic acid”. In: Journal of the Brazilian Chemical Society 22 (2011), pp. 422–427.

[18] Arun Prakash Periasamy, Yogeswaran Umasankar, and Shen-Ming Chen. “Toluidine blue adsorbed on alcohol dehydrogenase modified glassy carbon electrode for voltammetric determination of ethanol”. In: Talanta 83.3 (2011), pp. 930–936.

[19] Mariana Emilia Ghica and Christopher MA Brett. “Poly (brilliant cresyl blue) modified glassy carbon electrodes: Electrosynthesis, characterisation and application in biosensors”. In: Journal of Electroanalytical Chemistry 629.1-2 (2009), pp. 35–42.

[20] Pattan-Siddappa Ganesh et al. “Fabrication of thymol blue film modified electrode and its synergetic effects for simultaneous and interference free detection of toxic dihydroxybenzene isomers: an experimental and theoretical approach”. In: Inorganic Chemistry Communications 172 (2025), p. 113764.

[21] Gong-Jun Yang et al. “Characterization, growth mechanism and application of network poly (bromophenol blue)”. In: Journal of Electroanalytical Chemistry 604.1 (2007), pp. 48–56.

[22] Ana Luiza Lorenzen LIMA. “Estudos de eletroquímica: reações químicas e energia. 1”. In: São Paulo, Brasil: Editora Intersaberes (2020).

[23] Mengwei Yuan and Shelley D Minteer. “Redox polymers in electrochemical systems: From methods of mediation to energy storage”. In: Current Opinion in Electrochemistry 15 (2019), pp. 1–6.

[24] Jizhen Zhang et al. “Mechanical properties of graphene films enhanced by homotelechelic functionalized polymer fillers via π–π stacking interactions”. In: Composites Part A: Applied Science and Manufacturing 71 (2015), pp. 1–8.

[25] Hassan O Shoyiga and Omolola E Fayemi. “Conductive polymers and derivatives as recognition element for electrochemical sensing of food and drug additives: a brief perspective”. In: Heliyon 11.2 (2025).

[26] Sofija Petkovska and Rubin Gulaboski. “Diffusional electrochemical catalytic (EC’) mechanism featuring chemical reversibility of regenerative reaction-theoretical analysis in cyclic voltammetry”. In: Croatica Chemica Acta 92.4 (2019), pp. 495–502.

[27] Antoine Vautier et al. “Bridging Microbial and Electrochemical Redox Systems for Sustainable Wastewater Treatment and Energy Storage”. In: ACS Electrochemistry (2026).

[28] WE Van der Linden and J W_ Dieker. “Glassy carbon as electrode material in electro-analytical chemistry”. In: Analytica Chimica Acta 119.1 (1980), pp. 1–24.

[29] Sharon Hammes-Schiffer. Introduction: Proton-coupled electron transfer. 2010.

[30] Emily C Gentry and Robert R Knowles. “Synthetic applications of proton-coupled electron transfer”. In: Accounts of chemical research 49.8 (2016), pp. 1546–1556.

[31] Cyrille Costentin. “Electrochemical approach to the mechanistic study of proton-coupled electron transfer”. In: Chemical Reviews 108.7 (2008), pp. 2145–2179.

[32] Robert E Warburton, Alexander V Soudackov, and Sharon Hammes-Schiffer. “Theoretical modeling of electrochemical proton-coupled electron transfer”. In: Chemical reviews 122.12 (2022), pp. 10599–10650.

[33] Robin Tyburski et al. “Proton-coupled electron transfer guidelines, fair and square”. In: Journal of the American Chemical Society 143.2 (2021), pp. 560–576.

[34] Douglas A Skoog et al. Princípios de análise instrumental. 2002, p. 654.

[35] Bengi Uslu and Sibel A. Ozkan. “Electroanalytical Application of Carbon Based Electrodes to the Pharmaceuticals”. In: Analytical Letters 40.5 (2007), pp. 817–853. DOI: 10.1080/00032710701242121. eprint: https://www.tandfonline.com/doi/pdf/10.1080/00032710701242121.

[36] E Lojou and P Bianco. “Application of the electrochemical concepts and techniques to amperometric biosensor devices”. In: Journal of Electroceramics 16 (2006), pp. 79–91.

[37] G.R. Agladze et al. “Comparative study of hydrogen peroxide electro-generation on gas-diffusion electrodes in undivided and membrane cells”. In: Journal of Applied Electrochemistry 37 (Mar. 2007), pp. 375–383. DOI: 10.1007/s10800-006-9269-x.

[38] Zhenping Liu et al. “Electrochemical sensor integrated microfluidic device for sensitive and simultaneous quantification of dopamine and 5-hydroxytryptamine”. In: Sensors and Actuators B: Chemical 273 (2018), pp. 873–883.

[39] F Gołek et al. “AFM image artifacts”. In: Applied surface science 304 (2014), pp. 11–19.

[40] Patrick Frederix and Matthew R Linford. “Surface Analysis by Atomic Force Microscopy (AFM)”. In: ().

[41] Paulo SP Herrmann et al. “Microscopia de varredura por força: uma ferramenta poderosa no estudo de polímeros”. In: Polímeros 7 (1997), pp. 51–61.

[42] Nicholas A Geisse. “AFM and combined optical techniques”. In: Materials today 12.7-8 (2009), pp. 40–45.

[43] Chengwei Xing et al. “Application of atomic force microscopy in bitumen materials at the nanoscale: A review”. In: Construction and Building Materials 342 (2022), p. 128059.

[44] Geometrical Product Specifications (GPS) – Filtration – Part 21: Linear Profile Filters: Gaussian Filters. International Standard. Geneva, Switzerland: International Organization for Standardization, 2025.

[45] Geometrical Product Specifications (GPS) – Surface Texture: Profile Method – Rules and Procedures for the Assessment of Surface Texture. International Standard. Geneva, Switzerland: International Organization for Standardization, 1996.

[46] Mehdi Asgharifar et al. "An experimental and numerical study of effect of textured surface by arc discharge on strength of adhesively bonded joints". In: J. Mech. Eng. Automat 2 (2012), pp. 229–242.

[47] Gaëtan Le Goïc et al. "Outlier filtering: a new method for improving the quality of surface measurements". In: Measurement Science and Technology 24.1 (2013), p. 015001.

[48] American Society of Mechanical Engineers. Standards Committee B46. Classification, Designation of Surface Qualities, and American National Standards Institute. Surface Texture: Surface Roughness, Waviness and Lay. American Society of Mechanical Engineers, 2003.

[49] Azad Mohammed and Avin Abdullah. "Scanning electron microscopy (SEM): A review". In: Proceedings of the 2018 International Conference on Hydraulics and Pneumatics—HERVEX, Băile Govora, Romania. Vol. 2018. 2018, pp. 7–9.

[50] A Salman Ali. "Application of nanomaterials in environmental improvement". In: Nanotechnology and the Environment (2020), pp. 17–36.

[51] E Suzuki. "High-resolution scanning electron microscopy of immunogold-labelled cells by the use of thin plasma coating of osmium". In: Journal of microscopy 208.3 (2002).

[52] David B Williams and C Barry Carter. "Transmission electron microscopy: a textbook for materials science". In: Micron 28.1 (1997), pp. 75–75.

[53] Ray F Egerton et al. Physical principles of electron microscopy. Vol. 56. Springer, 2005.

[54] Helmut Kohl. "Transmission Electron Microscopy". In: Encyclopedia of Nanotechnology. Springer, 2016, pp. 4218–4233.

[55] Sandeep Bhattacharya, A Reza Riahi, and Ahmet T Alpas. “A transmission electron microscopy study of crack formation and propagation in electrochemically cycled graphite electrode in lithium-ion cells”. In: Journal of Power Sources 196.20 (2011), pp. 8719–8727.

[56] Jeanne Ayache et al. Sample preparation handbook for transmission electron microscopy: techniques. Vol. 2. Springer Science & Business Media, 2010.

[57] Brian C Smith. Fundamentals of Fourier transform infrared spectroscopy. CRC press, 2011.

[58] George Socrates. Infrared and Raman characteristic group frequencies: tables and charts. John Wiley & Sons, 2004.

[59] Alessio Ausili, Marina Sánchez, and Juan C Gómez-Fernández. “Attenuated total reflectance infrared spectroscopy: A powerful method for the simultaneous study of structure and spatial orientation of lipids and membrane proteins”. In: Biomedical Spectroscopy and Imaging 4.2 (2015), pp. 159–170.

[60] Michael Thompson, Stephen LR Ellison, and Roger Wood. “Harmonized guidelines for single-laboratory validation of methods of analysis (IUPAC Technical Report)”. In: Pure and applied chemistry 74.5 (2002), pp. 835–855.

[61] Kritika Rai et al. “Comparitive study between ICH guideline and anvisa guideline”. In: Int. J. Res. Pharm. Chem 10.31 (2020), pp. 173–90.

[62] D Brynn Hibbert. Compendium of terminology in analytical chemistry. Royal society of chemistry, 2023.

[63] Guzel Ziyatdinova, Ekaterina Guss, and Elvira Yakupova. “Electrochemical sensors based on the electropolymerized natural phenolic antioxidants and their analytical application”. In: Sensors 21.24 (2021), p. 8385.

[64] Lavaraj Devkota et al. “Electrochemical determination of tetracycline using AuNP-coated molecularly imprinted overoxidized polypyrrole sensing interface”. In: Electrochimica Acta 270 (2018), pp. 535–542.

[65] Hai Zhao et al. “Electropolymerized molecularly imprinted electrochemical sensor for sensitive and selective detection of an antipsychotic compound chlorpromazine”. In: International Journal of Electrochemical Science 20.8 (2025), p. 101076.

[66] Sanni Kumar et al. “Recent advances in biosensors for diagnosis and detection of sepsis: A comprehensive review”. In: Biosensors and Bioelectronics 124 (2019), pp. 205–215.

[67] Lung-Chieh Chen et al. “Improving the reproducibility, accuracy, and stability of an electrochemical biosensor platform for point-of-care use”. In: Biosensors and Bioelectronics 155 (2020), p. 112111.

[68] Allen J Bard, Larry R Faulkner, and Henry S White. Electrochemical methods: fundamentals and applications. John Wiley & Sons, 2022.

[69] Ross Bogey, Kay Cerny, and Olfat Mohammed. “Repeatability of wire and surface electrodes in gait”. In: American journal of physical medicine & rehabilitation 82.5 (2003), pp. 338–344.

[70] Elton Santos Franco et al. “Validação de método analítico por ELL-CG-EM para detecção de trialometanos decorrentes da cloração de águas contendo Microcystis”. In: Engenharia Sanitária e Ambiental 24.05 (2019), pp. 1003–1012.

[71] Juan M Sanchez. “Estimating detection limits in chromatography from calibration data: ordinary least squares regression vs. weighted least squares”. In: Separations 5.4 (2018), p. 49.

[72] David B Rorabacher. “Statistical treatment for rejection of deviant values: critical values of Dixon’s” Q” parameter and related subrange ratios at the 95% confidence level”. In: Analytical chemistry 63.2 (1991), pp. 139–146.

[73] Frank E Grubbs. “Procedures for detecting outlying observations in samples”. In: Technometrics 11.1 (1969), pp. 1–21.

[74] Walter Augusto Braun et al. “Eletropolimerização de azul de metileno sobre carbono vítreo e estabilidade do filme de poli (azul de metileno)”. In: Scientia Plena 12.9 (2016).

[75] Khan Loon Ng and Sook Mei Khor. “Graphite-based nanocomposite electrochemical sensor for multiplex detection of adenine, guanine, thymine, and cytosine: a biomedical prospect for studying DNA damage”. In: Analytical chemistry 89.18 (2017), pp. 10004–10012.

[76] Abdulkadir Levent. “Voltammetric behavior of acebutolol on pencil graphite electrode: highly sensitive determination in real samples by square-wave anodic stripping voltammetry”. In: Journal of the Iranian Chemical Society 14 (Aug. 2017). DOI: 10.1007/s13738-017-1184-z.

[77] Noémie Elgrishi et al. “A practical beginner’s guide to cyclic voltammetry”. In: Journal of chemical education 95.2 (2018), pp. 197–206.

[78] Frank Nelson Crespilho Ferreira. “Electrochemical nano (bio) sensors: advances, diagnosis and monitoring of diseases Rodrigo Michelin Iost1, Welter Cantanhede da Silva2, Joao Marcos Madurro3, Ana Graci Brito Madurro4, Lucas Franco”. In: Frontiers in Bioscience 3 (2011).

[79] PubChem. Guanine. Accessed: 2024-07-02. 2024.

[80] Sudarshan Mahapatra et al. “Anhydrous adenine: crystallization, structure, and correlation with other nucleobases”. In: Crystal Growth and Design 8.4 (2008), pp. 1223–1225.

[81] Jessica Maiuolo et al. “Regulation of uric acid metabolism and excretion”. In: International journal of cardiology 213 (2016), pp. 8–14.

[82] Oreste Arrigoni and Mario C De Tullio. “Ascorbic acid: much more than just an antioxidant”. In: Biochimica et Biophysica Acta (BBA)-General Subjects 1569.1-3 (2002), pp. 1–9.

[83] Rimsha Larik et al. “Electrochemical sensor for catechol detection: Leveraging ITO@ TiO2/RGO/Pt nanocomposites for enhanced water quality monitoring”. In: Materials Science and Engineering: B 313 (2025), p. 117966.

[84] Bensalah et al. “Electrochemical oxidation of hydroquinone, resorcinol, and catechol on boron-doped diamond anodes”. In: Environmental science & technology 39.18 (2005), pp. 7234–7239.

[85] Volodymyr Valentynovych Tkach et al. “A Descrição Matemática do Desempenho Eletroanalítico de Nanopartículas de Óxido de Cobre(II) na Eletrodetecção de Hidrazina”. In: Orbital: The Electronic Journal of Chemistry 6 (2014), pp. 142–146.

[86] Hui Wang et al. “Cobalt nanoparticles intercalated nitrogen-doped mesoporous carbon nanosheet network as potential catalyst for electro-oxidation of hydrazine”. In: International Journal of Hydrogen Energy 45.38 (2020), pp. 19344–19356.

[87] Güneş Demirtaş, Necmi Dege, and Orhan Büyükgüngör. “A third monoclinic polymorph of 3, 4, 5-trihydroxybenzoic acid monohydrate”. In: Structure Reports 67.6 (2011), o1509–o1510.

[88] AA Alturfan. “Water-soluble vitamins”. In: A Guide to Vitamins and Their Effects on Diseases; Cambridge Scholars Publishing: Newcastle upon Tyne, UK (2023), pp. 71–74.

[89] John D Fernstrom and Madelyn H Fernstrom. “Tyrosine, phenylalanine, and catecholamine synthesis and function in the brain2”. In: The Journal of nutrition 137.6 (2007), 1539S–1547S.

[90] Sagar S Arya et al. “Vanillin: A review on the therapeutic prospects of a popular flavouring molecule”. In: Advances in traditional medicine (2021), pp. 1–17.

[91] Ivana Bošnjak et al. “Occurrence of protein disulfide bonds in different domains of life: a comparison of proteins from the Protein Data Bank”. In: Protein engineering, design & selection 27.3 (2014), pp. 65–72.

[92] Jens ET Andersen. “The standard addition method revisited”. In: TrAC Trends in Analytical Chemistry 89 (2017), pp. 21–33.

[93] R. M. Silverstein, F. X. Webster, and D. J. Kiemle. Spectrometric Identification of Organic Compounds. Wiley, 2014.

[94] Cátia da Cruz Santos et al. “Electropolymerization of phenol and aniline derivatives: Synthesis, characterization and application as electrochemical transducers”. In: Journal of Electroanalytical Chemistry 846 (2019), p. 113163.

[95] George Socrates. Infrared and Raman Characteristic Group Frequencies. Wiley, 2004.

[96] John Coates. Interpretation of Infrared Spectra, A Practical Approach. Wiley, 2000.

[97] Boris Lakard. “Electrochemical biosensors based on conducting polymers: a review”. In: Applied Sciences 10.18 (2020), p. 6614.

[98] Mohammed A Ali Omer and Abdalla Abdelkarem Abdalla. “Preparation & characterization of polyvinyl alcohol/thymol blue composites gel and films for low radiation dosimetry”. In: Journal of Radiation Research and Applied Sciences 17.4 (2024), p. 101103.

[99] Catherine E Dowding et al. “A new method for gaining insight into the chemistry of drying mineral surfaces using ATR-FTIR”. In: Journal of colloid and interface science 292.1 (2005), pp. 148–151.

[100] MP Amaral et al. “Electrosynthesis of PolyFilm Modified Graphite Electrode and its Application Towards Determination of Thymine”. In: Materials Research 28.Suppl 1 (2025), e20250163.

[101] Christopher MA Brett, György Inzelt, and Vilmos Kertesz. “Poly (methylene blue) modified electrode sensor for haemoglobin”. In: Analytica Chimica Acta 385.1-3 (1999), pp. 119–123.

[102] Maria Inês Costa Marinho, Murilo Feitosa Cabral, and Luiz Henrique Mazo. “Is the poly (methylene blue)-modified glassy carbon electrode an adequate electrode for the simple detection of thiols and amino acid-based molecules?” In: Journal of Electroanalytical Chemistry 685 (2012), pp. 8–14.

[103] MP do Amaral et al. “Simultaneous and selective electrochemical determination of adenine and guanine using a poly (brilliant Cresyl blue)-modified electrode”. In: Materials Letters (2025), p. 139731.

[104] Roohollah Torabi Kachoosangi, Gregory G Wildgoose, and Richard G Compton. “Carbon nanotube-based electrochemical sensors for quantifying the ‘heat’of chilli peppers: the adsorptive stripping voltammetric determination of capsaicin”. In: Analyst 133.7 (2008), pp. 888–895.

[105] Diego Pessoa Rocha et al. “Desenvolvimento e caracterização de eletrodos modificados com materiais nano-estruturados de carbono”. In: (2020).

[106] Horacio J Salavagione et al. “Spectroelectrochemical study of the oxidation of aminophenols on platinum electrode in acid medium”. In: Journal of electroanalytical Chemistry 565.2 (2004), pp. 375–383.

[107] Ching Tang, Umasankar Yogeswaran, and Shen-Ming Chen. “Simultaneous determination of adenine guanine and thymine at multi-walled carbon nanotubes incorporated with poly (new fuchsin) composite film”. In: Analytica chimica acta 636.1 (2009), pp. 19–27.

[108] Tingfan Tang et al. “Sensitive and selective electrochemical determination of uric acid in urine based on ultrasmall iron oxide nanoparticles decorated urchin-like nitrogen-doped carbon”. In: Colloids and Surfaces B: Biointerfaces 216 (2022), p. 112538.

[109] Ruijuan Wang et al. “The electrochemical detection of ascorbic acid constructed on CuO nanocubes with excellent sensitivity and wide linearity”. In: Journal of Molecular Structure 1328 (2025), p. 141314.

[110] Qasar Saleem et al. “A highly explicit electrochemical biosensor for catechol detection in real samples based on copper-polypyrrole”. In: RSC advances 13.20 (2023), pp. 13443–13455.

[111] Guangri Xu et al. “Simultaneous determination of hydroquinone, catechol and resorcinol at poly (3-thiophenemalonic acid) modified glassy carbon electrode”. In: International Journal of Electrochemical Science 10.12 (2015), pp. 10659–10667.

[112] Kalil Cristhian Figueiredo Toledo and Juliano Alves Bonacin. “Unveiling Electrochemical Frontiers: Enhanced Hydrazine Sensing with Na3 [Fe (CN) 5 (PZT)] Modified Electrodes”. In: Inorganics 13.3 (2025), p. 85.

[113] P Raghu et al. “A novel electrochemical biosensor based on horseradish peroxidase immobilized on Ag-nanoparticles/poly (l-arginine) modified carbon paste electrode toward the determination of pyrogallol/hydroquinone”. In: Enzyme and microbial technology 52.6-7 (2013), pp. 377–385.

[114] Rajni Kumari et al. “Metal nanocomposites-based electrochemical sensor for the detection of Vanillin (food additives): Experimental and theoretical approach”. In: Food Bioscience 52 (2023), p. 102464.

[115] Yingju Liu et al. “Construction of europium hexacyanoferrate film and its electrocatalytic activity to tyrosine determination”. In: Applied surface science 256.10 (2010), pp. 3148–3154.

[116] Tao Zhan et al. “3D printed electrochemical sensor and microfluidic system for the detection of L-tryptophan using degradable material”. In: Food Chemistry 475 (2025), p. 143331.

[117] Taher Alizadeh, Behnam Zabihi, and Ahmad Amiri. “A novel L-Cysteine voltammetric sensor based on a dual-nucleation copper (II) complex”. In: Microchemical Journal 202 (2024), p. 110803.

[118] Ayah Moustafa et al. “Electrochemical sensing of vitamin B6 (pyridoxine) by adapted carbon paste electrode”. In: Scientific Reports 14.1 (2024), p. 21972.

TERMO DE AUTORIZAÇÃO PARA PUBLICAÇÃO/DIVULGAÇÃO DE DOCUMENTO ELETRÔNICO NO CATÁLOGO DO SISTEMA DE BIBLIOTECAS DO CEFET/RJ E NO REPOSITÓRIO INSTITUCIONAL

Na qualidade de titular dos direitos de autor da publicação abaixo citada, de acordo com a Lei nº 9610/98, autorizo, a partir da presente data, o CEFET/RJ, a disponibilizar gratuitamente, sem ressarcimento de direitos autorais, conforme permissões assinadas abaixo, no Catálogo Online do Sistema de Bibliotecas e no Repositório Institucional do Cefet/RJ, ou qualquer outro formato de disseminação da informação que a instituição implemente, no formato PDF, para fins de leitura, impressão e/ou download pela internet, a título de divulgação da produção científica gerada por esta Instituição.

1- Tipo de trabalho: [ ] Projeto Final (Graduação) [ ] Especialização
[ ] Dissertação [X] Tese

2- Identificação do trabalho/autor(es):

Curso: PPGIO – Programa de Pós Graduação em Instrumentação e Ótica
Título: Electropolymerized Dye-Modified Graphite Electrodes for Selective and Sensitive Multi-Analyte Electrochemical Detection in Biomedical and Environmental Systems
Autor(es): Monique Pacheco do Amaral
Orientador: Ana Lucia Ferreira de Barros
Co-orientador: Ladário da Silva

3- Informações de acesso ao trabalho:

Este trabalho é confidencial? [ ] Sim [x] Não
Pode ser liberado para publicação? [x] Total [ ] Parcial [ ] Não
Justifique:_____
_____
Em caso de publicação parcial, assinale as permissões:
[ ] Sumário
[ ] Capítulos. Especifique: _____
[ ] Bibliografia
[ ] Outras partes do trabalho: _____

Rio de Janeiro, 18/06/2026

gov.br Documento assinado digitalmente
MONIQUE PACHECO DO AMARAL
Data: 18/06/2026 20:28:56-0300
Verifique em https://validar.iti.gov.br

_____
Assinatura do(s) autor(es)

Ana Lucia Ferreira de Barros Assinado de forma digital por Ana Lucia Ferreira de Barros
Dados: 2026.06.19 03:52:26 -03'00'

_____
Assinatura do orientador

gov.br Documento assinado digitalmente
LADARIO DA SILVA
Data: 18/06/2026 22:04:49-0300
Verifique em https://validar.iti.gov.br

_____
Assinatura do co-orientador